Contributions to understanding the mechanisms of action of Electrolytic Electroporation

Nina Klein

TESI DOCTORAL UPF / 2021

Thesis supervisors

Dr. Antoni Ivorra Cano

Dr. Michael Klaus Stehling

DEPARTMENT OF INFORMATION AND COMMUNICATION TECHNOLOGIES

UNIVERSITAT POMPEU FABRA

This work was carried out as an industrial PhD in the Department of Information and Communication Technologies (DTIC) at the Universitat Pompeu Fabra (academic sphere), and at the Institut für Bildgebende Diagnostik (industrial sphere).

The technology E2 is being developed by a spin-off company of the Institut für Bildgebende Diagnostik, called Inter Science GmbH, in which the doctoral student is involved.

Nina Klein was supported with a mobility fund of the Industrial PhD program from the Catalan Government (Programa de Doctorats Industrials, AGAUR, 2017 Di 82).

Dedication and acknowledgements

I would like to express my greatest gratitude to my PhD supervisor Prof. Dr. Antoni Ivorra Cano for giving me the opportunity to pursue research in the field of electroporation. His experience and valuable knowledge of the field and his helpful input during discussions made it possible for me to deepen my understanding of electroporation processes. His endless patience with me, along with his guidance and support throughout the project have helped me conduct the studies, even at times where things were not easy.

Secondly, I would like to thank my second supervisor Prof. Dr. Michael K. Stehling, for giving me the opportunity to pursue my PhD while working in his clinic. I am thankful for being given the chance to continue my studies, not only in the context of this research project but also in everyday clinical practice. The experiences I made are invaluable to me. I would further like to thank Enric Günther and everyone at InterScience GmbH for generously borrowing me equipment to conduct the research.

I am grateful for Dr. Borja Mercadal and Dr. Tomás García-Sánchez for their support in the lab, scientific input and guidance, all of which was of great help to me during my studies. I would like to thank everyone in the Biomedical Electronics Research Group and our lab neighbours at PRBB for the overwhelming kindness I received every time I visited Barcelona.

Thank you also to my family and friends, who always supported me. I especially would like to thank my mother for supporting me with love and sympathy and my father, who is not with us anymore to see me complete my PhD, but who always believed in me.

Lastly, I would like to sincerely thank my husband and soulmate Oliver, for the neverending kindness, love and support throughout the years. You are my rock during tough times, the best company I could ever ask for, and I will forever appriciate you. This PhD is dedicated to you, my love.

Abstract

Electroporation is a biophysical phenomenon in which cell membrane permeability to ions and molecules is increased when the cell is briefly exposed to high electric fields. Electroporation is the basis of multiple novel clinical treatment modalities. Reversible electroporation is the basis of Electrochemotherapy (ECT), a cancer treatment modality in which electric pulses are applied to enhance cellular uptake of chemotherapeutic agents. It is also the basis of Gene Electrotransfer, which is used in multiple therapies under clinical trials, including cancer treatments and vaccination. Irreversible electroporation (IRE) is used as a non-thermal ablation technique for treatment of solid tumors.

Electrolytic Electroporation (E2) is a novel tissue ablation technique which combines reversible electroporation with electrolysis.

This research project aimed at better understanding the interplay of the two components of E2 to achieve tumor eradication. In order to investigate the cell killing mechanism, *in vitro*, *in vivo* and *in silico* studies were performed and the information obtained was combined to demonstrate the E2's underlying mechanisms of action.

Contents

Acronyms and Abbreviations

BAX	BCL2-associated death promotor X
BCL2	B-cell CLL/lymphoma 2
C_e	Extracellular concentration
C_i	Intracellular concentration
CT	Computer Tomography
DC	Direct current
DMEM	Dulbecco's Modified Eagle's Medium
DPBS	Dulbecco's Phosphate-Buffered Saline
E2	Electrolytical Electroporation
EChT	Electrochemical Treatment
ECT	Electrochemotherapy
EDTA	Ethylenediaminetetraacetic acid
FBS	Fetal bovine serum
FEM	Finite element method
GET	Gene Electrotransfer
GSDMD	Gasdermin D
H+E	Hematoxylin and Eosin
HEK-293	Human embryonic kidney 293 cells
HEK-293 tsA201	transformed human kidney cell line stably expressing an SV40 temperature-sensitive T antigen
HFIRE	High Frequency Irreversible Electroporation
IRE	Irreversible Electroporation
MLKL	Mixed Lineage Kinase Domain Like Pseudokinase
MRI	Magnetic Resonance Imaging
MTT	Methylthiazoletetrazolium
NTIRE	Non-thermal Irreversible Electroporation
PAR	poly ADP-ribose
PI	Propidium Iodide
RIP3	Receptor-Interacting Protein 3
RPA	Relative Pore Area
TMV	Transmembrane voltage
TNFα	Tissue Necrosis Factor alpha
TUNEL	Terminal Deoxynucleotidyl Transferase dUTP Nick End Labeling
US	Ultrasound
XTT	Xanilide Tetrazolium

Preface

Chapter 1

1.1 Introduction

Electroporation is a biophysical phenomenon in which cell membrane permeability to ions and molecules is increased when the cell is briefly exposed to high electric fields. Under some conditions, the effect of electroporation can be transient and result in viable cells after the treatment. In this case the term reversible electroporation is applied. When the cells die due to excessive electric fields, either because of permanent permeabilization leading to cell lysis or because of too severe disruption of cell homeostasis during transient permeabilization, the term Irreversible Electroporation (IRE) is applied.

Electroporation is the basis of multiple novel clinical treatment modalities. Reversible electroporation is the basis of Electrochemotherapy (ECT), a cancer treatment modality in which electric pulses are applied to enhance cellular uptake of chemotherapeutic agents. It is also the basis of Gene Electrotransfer (GET), which is used in multiple therapies under clinical trials, including cancer treatments and vaccination. IRE is used as a non-thermal ablation technique for treatment of solid tumors.

There are other ablation modalities which apply current to tissue. Electrochemical treatment (EChT) has been harnessed for tissue ablation in medicine for several centuries. EChT employs low direct electric currents over longer periods of time to produce an electrochemical reaction, called electrolysis. New chemical species are generated at the interface of the electrodes and diffuse away from the electrodes into the tissue. These species are able to create a cytotoxic environment within the targeted tissue, which induces cell death.

Electrolytic Electroporation (E2) is a newly proposed tissue ablation technique which combines reversible electroporation with electrolysis, whilst affording lower voltages, lower energy and shorter procedure times than IRE, without the combined use of a chemotherapeutic drug.

1.2 Research questions

This research aimed at better understanding the mechanisms of tissue ablation by Electrolytic Electroporation. One of the goals of this thesis was to investigate the interplay of the two major components of the treatment, electroporation and electrolysis, and the roles they play to achieve the treatment effect.

Another goal of the thesis was to determine the lower limits of the two components in a clinical setting.

One of the main practical objectives of this thesis was to develop and combine a set of mathematical models on the basis of the obtained knowledge, which can be further developed to predict treatment outcomes of an E2 application, considering effects of electroporation, electrolysis and mass transfer.

1.3 Dissertation outline

Chapter 2 provides an overview on the different biophysical and cellular phenomena which play a role in electroporation-based therapies and electrochemical treatment. It is intended to provide background information on electroporation, electrochemical treatment, cell death and its assessment, and general mathematical modelling techniques.

The studies of this research can be divided according to the three sets of methods that were applied: 1) *in vitro* studies 2) *in vivo* studies and 3) *in silico* studies. The Chapters 3, 4 and 5 summarize the work of each method.

In the first step, data sets were acquired through *in vitro* (Chapter 3) and *in vivo* (Chapter 4) studies to gather information on the mechanisms of action and effects of the application as compared to the other electroporation-based therapies or EChT. This data then served as the basis for the numerical models in Chapter 5.

Finally, Chapter 6 provides an overview on the main conclusion of this research and discusses how the research can be advanced in future projects.

Background

Chapter 2

2.1 Electroporation as the basis for ablation therapies

Electroporation is the increase of permeability of the cell membrane when the cell is briefly exposed to high electric fields delivered across a biological cell [1]. The effect on the cell membrane is a function of the applied electric field strength and pulse parameters such as pulse duration or shape (Figure 1). Lower electric fields produce reversible electroporation, in which case the cell returns to its original state a few seconds or minutes after the electric field has ceased [1]. This phenomenon is used for gene delivery and uptake of drugs [2, 3] and fusing between individual cells [4].

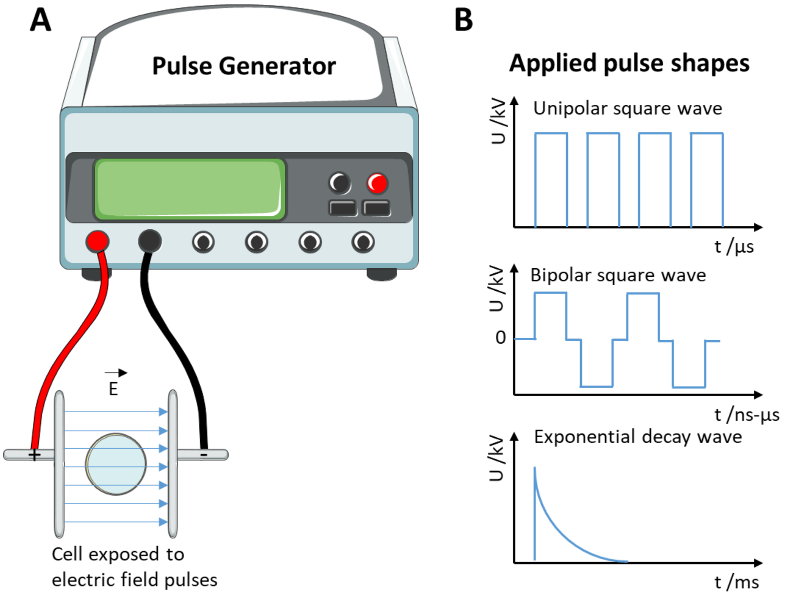

Figure 1: Simplified scheme of an *in vitro* electroporation treatment. **A:** Simplified scheme of an *in vitro* electroporation set-up. Cells are exposed to repetitive (Hz – kHz) very short (from several nanoseconds to several milliseconds) and intense (0.5 – 80 kV/cm) electric field (E) pulses provided by a pulse generator. **B:** Typical pulse shapes used in electroporation: Unipolar square waves, bipolar square waves and exponential decay waves. Here, a variety of pulse parameters such as pulse number, amplitude, duration, frequency and interpulse delay is possible.

Electrochemotherapy (ECT), the combination of reversible electroporation and anticancer drugs such as bleomycin, has successfully been used for decades for cancer treatment in clinical environments [5]. ECT usually employs eight 100 microsecond long pulses, with electric fields between 1000 and 1500 V/cm. While the technology is effective for the treatment of cancer, it requires the application of drugs, putting it into the regulatory domain of drug therapies and increasing the risk of drug-based side effects.

ECT has been included in several national and international guidelines for the treatment of cutaneous metastases and primary skin cancer [6–8] and has been investigated for a broad spectrum of clinical applications in other areas, such as treatment of cutaneous metastases of any histology [9], large breast cancer chest wall recurrences [10] prostate [11], bone metastases [12] and other deep-seated tumors [13–15]. There are multiple clinical trials currently running to study the effects of ECT for internal cancers such as liver, pancreas and lung.

At higher applied electric fields, cell death occurs due to the permanent or temporal membrane electroporation process [16], a mechanism broadly referred to as **Irreversible Electroporation (IRE)**. The technology was brought from first proof of concept [17] to clinical applications through the design of the IRE devices [16]. IRE has gained success in clinical tumor ablation [18], especially due to its property that it can ablate tissues without the need for drug injection or resorting to thermal damage. This is why the procedure is also known as non-thermal irreversible electroporation (NTIRE) [19]. NTIRE ablates only the cells, while preserving the extracellular matrix. This spares important parts of the treated tissue such as large vessels [20], nerves [20] and other lumen structure [16], making it an attractive technique in clinical settings. Irreversible Electroporation has been applied successfully in liver [21], pancreas [22], prostate [23] and kidney [24, 25]. IRE has also been considered for the treatment of cardiac arrhythmias [26]. The combination of IRE and ECT has been tested recently for the ablation of lymph node metastases [27].

A disadvantage of the IRE procedure is that it employs very high electric fields in the order of 1500 to 2000 V/cm and sometimes hundreds of pulses over minutes. Both requirements (high voltages and many pulses) have drawbacks, as the application induces muscle contractions that require the use of a muscle relaxant and deep anesthesia during surgery [24]. The muscle contractions may also move the electrodes during treatment, resulting in possible complications [28]. The large number of pulses are usually delivered at a frequency of 1 Hz, to fit into the refractory period of the heart cycle. The application of **High-Frequency Irreversible Electroporation (HFIRE)** in bipolar bursts is one possibility to eliminate muscle contractions while still applying and benefiting from the IRE technology [29, 30]. HFIRE has already been investigated in a clinical trial [31]. A major drawback of this method remains the high voltage applied and relatively long treatment times.

Other noteworthy emerging combination therapies include Calcium Electroporation [32] and the combination of ECT [33, 34] or IRE in combination with immunotherapy [35].

2.2 Electrochemical Treatment for tissue ablation

Another non-thermal ablation modality is called Electrochemical treatment. Electrochemical treatment (EChT) was harnessed for tissue ablation in medicine since the early 1800s [36], and experienced a revival in the 1970s [37]. In EChT, dc currents are delivered through two electrodes brought to the vicinity of the targeted tissue. The dc current produces an electrochemical reaction, electrolysis, at the surface of electrodes. New chemical species are generated at the interface of the electrodes and diffuse away from the electrodes into the tissue. This diffusion occurs along a concentration gradient and by electrophoresis. These species are able to create a cytotoxic environment which can induce cell death. A leading mechanism of cell death is due to local changes in pH [38].

During the treatment, the electrochemical reaction at the anode mainly consists in water decomposition and chloride oxidation, while oxygen, protons and chlorine are released [39, 40] (Figure 2). At the cathode, the reaction consists in the production of hydrogen and hydroxide ions. Ionic species which are close to the electrode are transported through the tissue or other media by diffusion, migration and convection. This results in a mass transport from anode to cathode and an acidification at the anode, while at the cathode there is alcalinization [41]. Depending on the treatment area, the developed gases partially remain present, reacting further with components of the tissue [42]. These chemical reactions induce both the production of new toxic products as well as local pH changes [43]. Figure 2 illustrates these processes in a simplified way. As tissue typically has a buffer capacity to it, even more processes will take place within the tissue, such as bicarbonate and protein buffer reactions. This will be explained in more detail in Chapter 5.

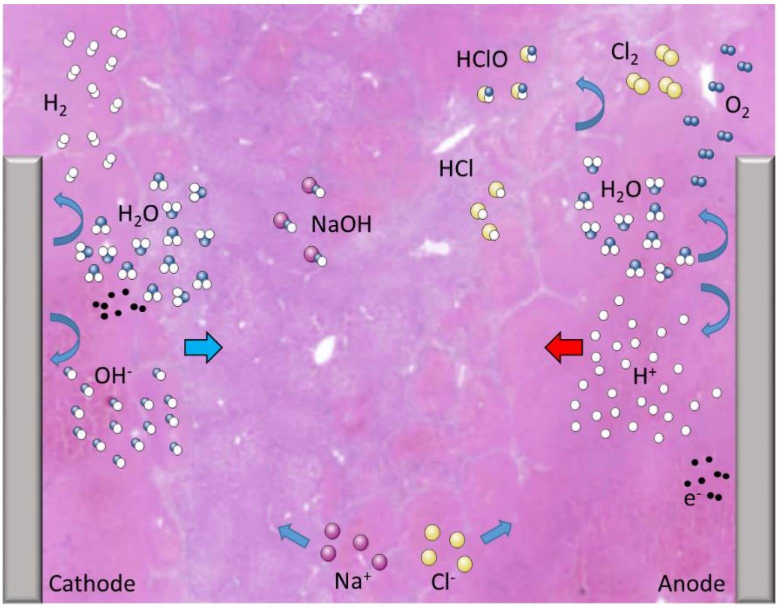

Figure 2: Illustration of the essential chemical reactions occurring during EChT in saline solution. Na^+, sodium; Cl^-, chlorine; NaOH, sodium hydroxide; Cl_2, chlorine (gas); HCl, hydrochloric acid; HClO, hypochlorous acid, H_2O, water; OH^-, hydroxide ion; O_2, oxygen (gas); H_2, hydrogen (gas); e^-, electron.

During the last two decades, substantial research has been done on tissue ablation by electrolysis [44–47]. EChT requires very low voltage and current, providing advantages relative to other ablation techniques, including reduced instrumentation complexity. However, the ablation caused by electrolysis requires high electrolytic species concentration and consequently long exposure time (tens of minutes to hours). The length of the procedure is a drawback. Another drawback is that given the long treatment time, non-Nernst-Planck type diffusion and blood transportation phenomenon *in vivo* lead to an almost unpredictable distribution of electrolytic products and therefore ablation dimensions are difficult to plan [48], though it has been suggested that the extreme pH changes during the treatment can reliably predict the extent of the necrotic area [49].

2.3 Electrolytic Electroporation as a novel treatment option

The combination of electroporation with electrolysis, also called Electrolytic Electroporation or E2, has been proposed as a novel tissue ablation modality. E2 has been developed in a systematic way similar to ECT and IRE, from basic concept through small animal studies to large animal studies. The results have been published in a series of publications [50–55].

The mechanistic explanation of the E2 technology is related to simultaneous permeabilization of the cell membrane and production of electrolytic products. It is suggested that the products of electrolysis can, thereby, gain access to the interior of the cell by the permeabilized cell membrane, which induces a homeostasis impairment and ultimately results in cell death.

Studies have shown that the combination has advantages over tissue ablation by either electroporation or electrolysis alone [53, 54]. One of them is that it requires substantially fewer electric pulses and at a much lower electric field amplitude than conventional NTIRE, which has the goal to kill cells by electroporation and thus has higher electric field thresholds. The latter is the main reason for most of the challenges of IRE in terms of treatment design, maximum ablation sizes per electrode placement and electrical safety design. E2 still has the advantages of NTIRE, as it is also non-thermal and does not require the injection of drugs, unlike Electrochemotherapy.

Earlier studies on E2 employed waveforms that delivered electrolysis and electroporation sequentially and separately [51, 53, 54]. This remains an attractive E2 modality, as it requires only the addition of a low voltage electrolysis device to conventional electroporation pulses. The disadvantage to this approach is that it requires the use of two devices and therefore two control systems. Subsequently, it was shown that the combination of electroporation and electrolysis can be achieved through an exponential decay-type pulse that delivers electroporation and electrolysis simultaneously [52, 56].

In the most recent design of the E2 application, a part of the pulse induces effective cell membrane permeabilization, while another part generates the electrolytic products. Furthermore, the trailing lower voltage provides an electrophoretic force to transport the electrolytic products from the electrodes through the treated zone (Nernst-Planck driven diffusion).

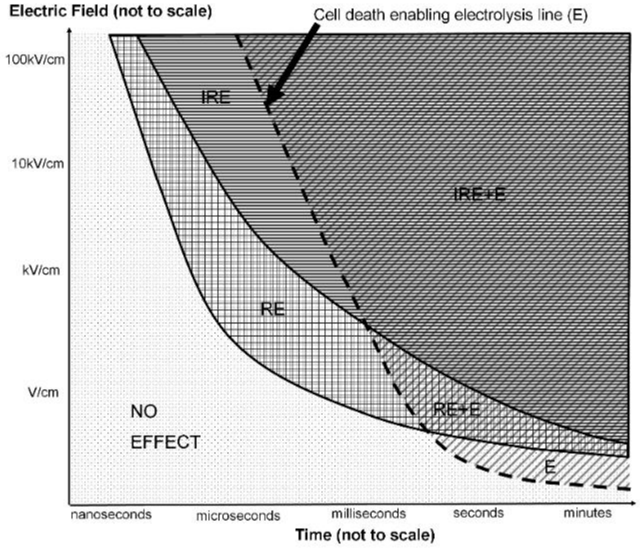

Figure 3: Schematic graph of tissue ablation domains as a function of electric field pulse length. E indicates ablation by electrolysis; RE + E stands for the combination of reversible electroporation and electrolysis; IRE + E stands for the of combination irreversible electroporation and electrolysis [50].

2.4 Mechanisms of cell death

Cell death can generally be classified into two groups, regulated and accidental cell death.

Primary necrosis is an accidental cell death and is related to cell injury, infection or trauma, and comes with an immediate loss of cell membrane integrity, thus undergoing different structural changes compared to the regulated forms of cell death. In the first step, swelling of the cells occur, followed by blebbing, then pyknosis, resulting in nuclear shrinkage, until finally the nucleus is dissolved into the cytoplasm, a process called karyolysis.

In contrast to that stand regulated cell deaths. A sub-group of regulated cell death are based on genetically encoded molecular mechanisms to ensure that unwanted or damaged cells are removed without negatively affecting surrounding tissue. They occur when the cell is exposed to micro-environmental stresses, such as (post)embryonic development, tissue homeostasis and immune responses [57] [58]. Apoptosis is one form of this type of cell death and has been subject to many studies. There are, however, several non-apoptotic mechanisms which can also be classified as regulated. A full list of regulated cell death mechanisms can be viewed in Table 1.

Cell death mechanisms in all types of cells destabilize survival mechanisms to induce their termination. The process of regulated cell death can be initiated through one of two pathways. In the intrinsic pathway the cell terminates itself because it senses cell stress, while in the extrinsic pathway the cell kills itself because of signals from outside. Anti-apoptotic survival signals can be from external sources (i.e. growth factors) and internal sources (i.e. BCL2, which stands for B-cell CLL/lymphoma 2), and pro-apoptotic survival signals can also be external (i.e. Fas, an apoptosis signaling factor or TNFα, tissue necrosis factor alpha) or internal (i.e. BAX, BCL2-associated death promotor X).

Table 1: Functional classification of regulated cell death modes, adapted from [57] and [58]. Highlighted cell death modes are of interest in this work. Abbreviations: ATG, autophagy; BCN1, beclin 1; $\Delta\psi m$, mitochondrial transmembrane potential; CrmA, cytokine response modifier A; DAPK1, death-associated protein kinase 1; EGFR, epidermal growth factor receptor; ERK1, extracellular-regulated kinase 1; IL, interleukin; MAP1LC3, microtubule-associated protein 1 light chain 3; MOMP, mitochondrial outer membrane permeabilization; NET, neutrophil extracellular trap; PAD4, peptidylarginine deiminase 4; PAR, poly(ADP-ribose); PARP1, poly(ADP-ribose) polymerase 1; PP2A, protein phosphatase 2A; ROCK1, RHO-associated, coiled-coil containing protein kinase 1; SQSTM1, sequestosome 1; TG, transglutaminase; Z-VAD-fmk, N-benzyloxycarbonyl-Val-Ala-Asp-fluoromethylketone; Z-YVAD-fmk, N-benzyloxycarbonyl-Tyr-Val-Ala-DL-Asp fluoromethylketone.

Cell death mode	Main biochemical features	Examples of inhibitory interventions
Alkaliptosis	Intracellular alkalinization; activation of NF-κB; caspase-independent	NAC (pH), N-acetyl alanine acid (pH); IMD0354 (IKBKB)
Anoikis	Downregulation of EGFR; Inhibition of ERK1 signaling; Lack of β1-integrin engagement; Overexpression of BIM Caspase-3 (-6,-7) activation	BCL-2 overexpression Z-VAD-fmk administration
Autophagic cell death	MAP1LC3 lipidation; SQSTM1 degradation	VPS34 inhibitors AMBRA1, ATG5, ATG7, ATG12 or BCN1 genetic inhibition
Caspase-dependent intrinsic apoptosis	MOMP; Irreversible $\Delta\psi_m$ dissipation; Release of IMS proteins; Respiratory chain inhibition	BCL-2 overexpression Z-VAD-fmk administration BCL-2 overexpression
Cornification	Activation of transglutaminases Caspase-14 activation	Genetic inhibition of TG1, TG3 or TG5 Genetic inhibition of caspase-14
Entosis	RHO activation; ROCK1 activation	Genetic inhibition of metallothionein 2A Lysosomal inhibitors
Extrinsic apoptosis by death receptors	Death receptor signaling Caspase-8 (-10) activation; BID cleavage and MOMP (in type II cells); Caspase-3 (-6,-7) activation	CrmA expression Genetic inhibition of caspases (8 and 3)

Cell death mode	Main biochemical features	Examples of inhibitory interventions
		Z-VAD-fmk administration
Extrinsic apoptosis by dependence receptors	Dependence receptor signaling; PP2A activation; DAPK1 activation; Caspase-9 activation; Caspase-3 (-6,-7) activation	Genetic inhibition of caspases (9 and 3) Genetic inhibition of PP2A Z-VAD-fmk administration
Ferroptosis	Iron accumulation; lipid peroxidation; ΔΨm dissipation; MAP1LC3B-I to MAP1LC3B-II conversion; glutaminolysis; caspase-independent	Deferoxamine (Fe); ferrostatin-1 (ROS); vitamin E (ROS); β-carotene (ROS); NAC (ROS); XJB-5-131 (ROS); CoQ10 (ROS); baicalein (ROS); vildagliptin (DPP4); thiazolidinedione (ACSL4); selenium (GPX4)
Mitotic catastrophe	Caspase-2 activation (in some instances); TP53 or TP73 activation (in some instances); Mitotic arrest	Genetic inhibition of TP53; Pharmacological or genetic inhibition of caspase-2
Necroptosis	Death receptor signaling; Caspase inhibition; RIP1 and/or RIP3 activation	Administration of necrostatin(s) Genetic inhibition of RIP1/RIP3
Netosis	Caspase inhibition; NADPH oxidase activation; NET release (in some instances)	Autophagy inhibition NADPH oxidase inhibition Genetic inhibition of PAD4
Parthanatos	PARP1-mediated PAR accumulation; Irreversible $\Delta\psi_m$ dissipation; ATP and NADH depletion; PAR binding to AIF and AIF nuclear translocation	Genetic inhibition of AIF Pharmacological or genetic inhibition of PARP1
Pyroptosis	Caspase-1 activation; Caspase-7 activation; Secretion of IL-1β and IL-18	Administration of Z-YVAD-fmk Genetic inhibition of caspase-1

Pyroptosis is a highly inflammatory form of regulated cell death: Immune cells recognize danger signals within themselves, release pro-inflammatory cytokines, swell, burst and eventually die. In contrast to apoptosis, pyroptosis requires the function of the enzyme caspase-1. Another factor that is unlike apoptosis is the fact that cell death by pyroptosis results in plasma-membrane rupture.

Necroptosis, another regulated form of necrosis, is induced by caspase-independent process in the presence of viral caspase inhibitors and has also been characterized as a component of inflammatory diseases. Unlike in apoptosis, it involves leakage of cell contents into the extracellular space, similar to pyroptosis.

Under conditions of acidic intracellular pH, the function of caspase-8 and other proteins can severely be altered. It is known that intracellular acidosis induces apoptosis [59] and necroptosis [60] in various types of cells. However, emerging evidence suggests that a change in intracellular pH regulation also indicates an early event associated with apoptosis induction via the mitochondria-dependent pathway [61]. This means that intracellular acidification can be the trigger and the amplifier of apoptosis. It is therefore necessary to carefully examine the biochemical features of the dell death mode to determine the actual cause of cell death.

Intracellular pH changes in the alkaline direction can also trigger cell death. Alkaliptosis is a relatively newly discovered form of regulated cell death and is driven by intracellular alkalinisation [58]. It mainly occurs when the proteins which participate in pH regulation are downregulated or otherwise altered. But it can also occur in a hypothetical acute situation were the pH of the intracellular space deviates strongly in the direction of basic pH.

Acute and long term intrinsic stress factors trigger different coping mechanisms in the cell. Acidic and alkaline intrinsic stress factors require an acute overload (e.g. intracellular protons) to trigger cell death. This is because the cell generally has a well-functioning buffer system with a buffering power of at least 10 mM [62]. In general, the long-term regulation of pH is robust, while the short-term regulation of acute internal acidic or alkaline loads is more complex [62]. The fast responding mechanisms include a) physicochemical buffering b) cellular consumption of nonvolatile acids and c) the transfer of acid or alkali between the cytosol and organelles [62]. These mechanisms reduce the impact of acute challenges on the intracellular pH, but are insufficient to counteract sustained stress or very big loads.

Ferroptosis is an iron-dependent form of non-apoptotic regulated cell death. While iron is an important trace element in the body, an abnormal distribution or large intracellular concentrations can strongly affect the normal physiological processes within the cell [63]. The mechanism of ferroptosis is via an iron-catalyzed process of lipid peroxidation, which can be initiated through both non-enzymatic and enzymatic mechanisms [58]. The consequences of uncontrolled lipid peroxidation leading to ferroptotic cell death are still not clear. However, multiple recent studies have shown that the increase of iron content in the labile iron pool, which is within the intracellular space, induces cell death [64–66]. Here, too, chronic and acute stress leads to different coping mechanisms of intracellular iron overload, with varying success [67]. But it seems that a very large concentration is required to trigger ferroptosis [67]. In fact, iron often requires additional stresses in order to induce cell death [67].

An example of inducing morphological changes in tissue through elevated intracellular concentrations of ions with regulatory roles is the case of chlorine. A study demonstrated that $[Cl^-]_i$ modulated expression and secretion profiles of an interleukin in airway epithelial cells, which then triggered airway inflammation [68]. While this did not directly trigger cell death, it did alter cell functions in a way that it impaired the regular operation of the cell. When looking at different triggering mechanisms of regulated cell death, it can be said that mild sub-lethal stressors can combine to induce cell death [67], and one of these stressors could be elevated $[Cl^-]_i$ or $[Fe^{2+}]_i$.

2.5 *In vitro* investigation for the assessment of cell death

A simple model for the investigation of electroporation-based therapies can consist of cells in suspension [69, 70]. While *in vitro* cellular models do not provide an accurate representation of *in vivo* morphology, as the models lack the complexity of the 3D architecture of tissue, their implementation, application and analysis is quick and cost-effective. However, there are severe differences between the different types of models, namely cells in suspension, cells in 2D culture and 3D cell cultures. The main reason for the inadequate insight into processes initiated by electroporation through *in vitro* models are the significant differences between animal tissue characteristics and those of cells in solution or 2D culture [71].

The development of 3D cell culture systems is an emerging method for the assessment of cell reactions after external stimuli of any kind [72]. Different models can be used, such as cell gel [73], spheroids [74] or decullularized human tissue [75]. The presence of cell-cell and cell-matrix interactions improves the representativeness of this method and can lead to results that are more adequately translated into *in vivo* systems [76]. While 3D cell cultures give better insight into the resulting processes than conventional 2D *in vitro* models, they are usually more difficult to culture, maintain and handle, and oftentimes associated with higher cost [71]. But because they have significant advantages over 2D models, it is necessary to balance reasons for and against the employment of 3D cell culture models for each study.

In general, there are different methods to detect electroporation effects *in vitro*. Figure 4 summarizes the multiple techniques and categorizes them into different groups: Import of exogenous substances, such as fluorophores [77], color stains (see below), magnetic nanoparticles [78], cytotoxic compounds [79] or nucleic acids [80]; the detection of leakage of the cell’s components [81, 82]; physical and chemical methods, such as conductivity and impedance measurements [83], or voltage clamp techniques [84]; and other methods like acoustic tests [85] or Raman microspectroscopy [86].

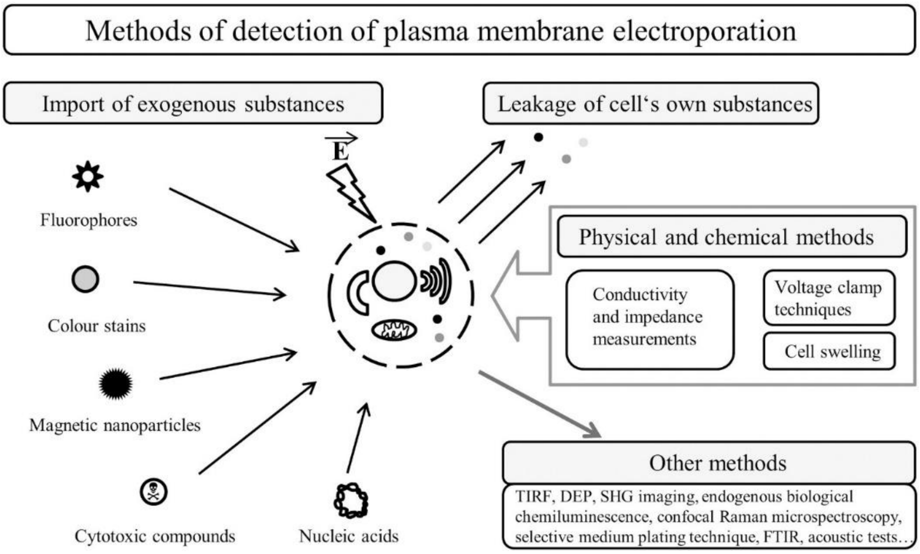

Figure 4: Summary of different methods used for the detection of membrane electroporation. TIRF – total internal reflection fluorescence microscopy, DEP – dielectrophoresis, SHG – second harmonic generation, FTIR – Fourier transform infrared spectroscopy [84].

There are different types of assays which can be used for *in vitro* experiments. Assays that measure metabolic activity are based on the enzymatic activity of the cells, which is indicated by conversion of dyes or other markers during the reaction within in cells that causes changes in colorimetric or fluorimetric features (i.e. shift in color, fluorescence). Amongst these assays are MTT (methylthiazoletetrazolium) assay [87], WST (water soluble tetrazolium), XTT (xanilide tetrazolium), or calcein AM assay. While these assays, in particular MTT, are easy to handle, they only represent the metabolic state of the cells, not quantitative viability. They can also introduce problems in the analysis of the data, since the obtained data might be affected by a specific treatment and cause misleading results on cell number or viability in general [88, 89].

Among membrane permeability assays are the crystal violet assay [90], trypan blue assay [91], and propidium iodide (PI). However, all of the mentioned assays have disadvantages: Crystal violet and trypan blue dyes will enter both alive and dead cells after a specific amount of time, making fast protocols necessary. Additionally, using the crystal violet assay is neither user-friendly nor easily repeatable. A widely used nucleic acid binding fluorophore is propidium iodide

(PI). PI cannot naturally pass the cell membrane and is thus excluded from viable cells. It is therefore regularly used for detecting cells with compromised membranes [92]. Its fluorescence enhances 20 to 30-fold when bound to DNA [93].

Other widely used assays for *in vitro* electroporation experiments are listed in Table 2.

Table 2: Comparison of different cell viability assays employed for *in vitro* analysis of electroporation [94].

Name of the assay	**Basis of the assay**	**Usual time between the experiment and cell viability results**	**Approx. time consumption for performing the assay (for 30 experimental points)**	**Reliability**
MTT	Metabolic activity	24–48 h	2-4 h	Variable
WST-1	Metabolic activity	24–48 h	2-4 h	Variable
MTS	Metabolic activity	24–48 h	2-4 h	Variable
XTT	Metabolic activity	24–48 h	2-4 h	Variable
Resazurin	Metabolic activity	24–48 h	2-4 h	Variable
Calcein AM	Metabolic activity	24–48 h	2-4 h	Variable
ATP (Luciferin-luciferase)	ATP concentration measurement	30 min – 24 h	<1 h	Low
PI	Membrane permeability	30 min – 24 h	~30 min	Low
Clonogenic	Cell proliferation	5–7 days	~30 min	High
Trypan blue	Counting of cells	Within 1h	~1 h	Low
Crystal violet	Counting of cells	24–48 h	~1 h	Low
Acridine orange/ ethidium bromide	Specific markers/ membrane permeability	12–72 h	<3 h	Variable
Annexin V/PI	Specific markers/ membrane permeability	12–72 h	<3 h	Variable

2.6 Mathematical modeling

Electrolytic Electroporation as a novel technique for tissue ablation involves different biophysical and biological mechanisms during and after its application that still need to be understood and described in detail.
One tool that may improve the understanding of fundamentals of the superimposed phenomena which occur during treatment is mathematical modeling. Through theoretical considerations and numerical simulations, it is possible to further understand the mechanisms and their interplay by testing hypothesis contained in the mathematical models. In addition, mathematical models can provide insight into the effects of not yet tested treatment parameters and may ultimately lead to improve treatment protocols.

Aspects of both electroporation [95] and electrolysis [96] have been considered in mathematical models in previous studies. In general, parameters such as electrode geometry, the applied voltage(s) and the electrical properties of the treated tissue(s) are important factors for both treatment types. Besides that, there are treatment-specific key factors that need to be considered in *in silico* investigations, which will be discussed in the following sub-chapters.

2.6.1 Mathematical modeling of Electroporation

Treatment success of electroporation-based therapies is provided through homogenously and effectively permeabilizing the cells throughout the treatment area. For a given pulsing protocol, a cell or tissue is successfully reversibly electropermeabilized when the local electric field exceeds a certain threshold value [97–99]. Shape and position of the electrodes, the applied voltage and tissue properties are of importance for determination of success [100].

A general schematic of the process of electroporation or electropermeabilization is shown in Figure 5: The application of an external electrical field (E_{ext}) leads to an increase of the transmembrane voltage (V_m). This induces an increase of the membrane conductivity σ_m, membrane permittivity ε_m, and membrane permeability p_m. An increase of σ_m and p_m will affect the membrane voltage until the pulse application ends.

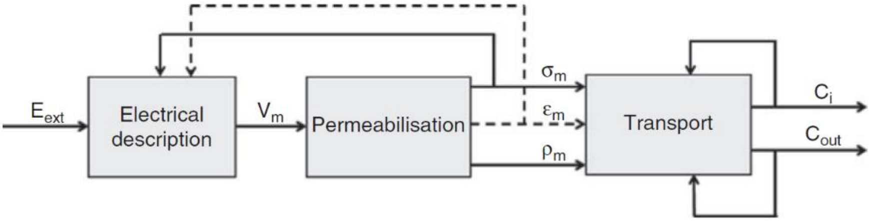

Figure 5: Schematic process of electroporation [101]. E_{ext} = external electrical field; V_m = transmembrane voltage; σ_m membrane conductivity; e_m = membrane permittivity; p_m = membrane permeability; C_i = current flow in; C_{out} = current flow out.

For the simulation of multiple pulses, simulations can become quite complex. The common simplification of electric field pulse protocols to a static electrical conductive media problem can be explained as follows:
Most protocols for electroporation-based therapies apply 100 µs long pulses. As the length of these pulses are long compared to the cell membrane charging constant, it can be assumed that the induced transmembrane voltage will reach its maximum value long before the end of the pulse. Therefore, it can be assumed that all transient effects of electroporation occur in the beginning of the pulse and end before the pulse ends. This approach makes it possible to significantly shorten simulation times for the models [102]. With that, the equation to solve becomes the Laplace equation for electric potential:

$$\nabla \cdot (\sigma \nabla \varphi) = 0 \tag{1}$$

where σ and φ represent tissue conductivity [S/m] and electric potential [V], and ∇ is the gradient operator. This can be applied when the capacitive transient and time course of conductivity increase during the pulse is neglected.

In order to take the increase in conductivity due to electroporation into account, the conductivity σ needs to be a function of the electric field (E):

$$E = \nabla \varphi \tag{2}$$

Including equation (2) is a necessity because in electroporation-based applications, the magnitude and temporal flow of applied electric current is highly nonlinear. This is dependent on the geometrical positioning of electrodes and pulse parameters such as pulse duration, number of pulses, frequency and shape. A recent example of how this effect can be implemented into a model is shown in [103], where the authors used data from *ex vivo* bovine liver experiments to develop a modified tissue conductivity model:

$$\sigma\left(\rho_{por}, \vartheta_{\sigma}, \vartheta_{T}\right) = (\sigma_{min} + (\sigma_{max} - \sigma_{min})\rho_{por}(1 - \alpha_0 + \alpha_T \log(1+, \vartheta_T) \quad (3)$$

with ρ_{por} as the level of poration, which increases as a function of electric field amplitude and decreases exponentially during the pulse; ϑ_{σ} is the poration damage indicator, which models the growth of pores during the application, and ϑ_T, the thermal damage indicator which models the damage effects due to Ohmic tissue heating. σ_{min} is the initial tissue conductivity and σ_{max} is the final tissue conductivity.

While this discrete-in-time model of tissue electroporation is designed to account for the dynamical behavior of tissue conductivity, it highly depends on the choice of the step time [104], which needs to be considered if applied.

Another important factor that needs to be considered is the temperature distribution during treatment. The temperature increase induced in the treated tissue is due to the Joule effect [105]. The Pennes' Bioheat equation is often used to determine temperature increase in tissue, because it considers the dynamic processes that occur in tissues, such as blood perfusion and metabolism. Blood perfusion is an effective way of the body to dissipate heat and is an important factor during electroporation-based treatments. Modifying this equation to include the Joule heating term, as previously done in [106], results in the equation

$$\nabla \cdot (k\nabla T) - \omega_b C_b \rho_b (T - T_a) + q''' + \sigma|\nabla\varphi|^2 = \rho C_p \frac{\partial T}{\partial t} \quad (4)$$

where k is the thermal conductivity of the tissue, T is the temperature above the arterial temperature (T_a = 37°C), w_b is the blood perfusion rate, C_b is the heat capacity of blood, ρ_b the blood density, q''' is the metabolic heat generation, ρ is the tissue density, and C_p is the heat capacity of the tissue.

To assess whether a specific set of pulse parameters and electrode configuration will cause thermal damage, the Arrhenius integral can be applied, which assumes that the damage follows first order reaction kinetics given by:

$$\Omega(t) = \int_0^{\tau(h)} \zeta \cdot e^{-Ea/(RT(t))} dt \qquad (5)$$

where ζ is the frequency factor, Ea the activation energy, R the universal gas constant, T(t) the temperature distribution and finally, τ(h) the heating time.

One of the numerical methods which is often used in electroporation research is the finite element method (FEM) [107, 108], which is based on discretizing the model geometry into a mesh of smaller elements, on which the unknown quantity (in the case of electroporation this is for instance the electric potential) is presumed to change according to a simple function (for instance a polynomial). The solution of the problem in its entirety is then solved by solving a set of algebraic equations for steady state problems. In the case of electroporation, the charge conversation equation can describe the state of the electroporated tissue at the end of a long pulse or a train of pulses when a steady state is assumed.

The mechanism of uptake of toxic components into the cell is a crucial aspect for electroporation-based treatments like ECT or GET. In general, the transport of charged exogenous molecules through the cell membrane is through diffusion along a concentration gradient, as well as movement by electrophoretic force. There are several factors that can severely impact the diffusion process, such as temporal changes of the electric field, the shape and temporal changes of the pores, and interactions between transported molecules and membrane walls [109]. Li *et al.* investigated the delivery of small molecules via electroporation [110]. In their model, they combined an asymptotic Smoluchowski equation for membrane permeabilization, with a Nernst–Planck equation system for ion transport. With that, they simulated calcium ion entry into Chinese Hamster Ovary cells, considering factors that play a role in pore formation. The group also considered molecular delivery via electrophoresis, which has been seen as an important factor in uptake of both small and large molecules for different electroporation-based therapies. In their compact model, they assume that not the degree of permeabilization, but the ambient conditions in the buffer significantly affect transmembrane molecular flux. This assumption allows to significantly simplify the model [110]. Both described models are examples on how to implement mass transfer and molecule uptake into the model.

There are other factors during electroporation-based applications that play a critical role in the determination of tissue ablation effects, such as inhomogeneity of tissue. This can lead to local electric field distortion and possibly inefficient homogenous electric field distribution, for instance due to the heat sink effect [105]. This effect can be included into the model by considering the electrodes as heat sinks which dissipate heat through the electrodes to the environment, as previously done in [106].

Several studies have investigated the effects of pH changes during pulsed electric field treatments [5]. In Gene Electrotransfer, substantial damage can be done on plasmids designated to be delivered or the cells themselves [113–116], which is why valuable investigations in this field were performed. To analyze pH fronts and their role in tissue damage in interaction with natural buffer, the Nernst-Planck equations for ion transport can be used, as described in the next subchapter, or in detail in [112] and [117].

There are only a few models that describe cell death of mammalian cells due to electroporation *in vivo*. A numerical investigation was performed in 2014, where cell death caused by heat and electroporation was considered [111]. The electroporation damage was assessed using the Peleg-Fermi model and the thermal damage by using the Arrhenius integral. However, this approach remains a gross estimation. Cell death models for *in vivo* application are still a challenge, as it is insufficient to use *in vitro* models for optimization purposes of *in vivo* applications, as there are significant differences in cell death thresholds [112].

In summary, the main aspects of *in silico* studies of electroporation are the consideration of electric field distribution, the electric properties of all materials used and the treated tissue, conductivity change, temperature increase and thermal damage. There are additional factors that can play an important role, such as molecule uptake and pH changes, which need to be considered with more or less focus, depending on their amount of significant contribution to the overall outcome of the applied treatment modality.

2.6.2 Mathematical modeling of Electrochemical treatment

In Electrochemical Treatment of biological tissues, a small dc current is applied to tissue, activating the electron transfer and polarizing the electrodes, which results in the formation of ions according to the following equations:

$$\text{Anode: } 2\ H_2O \leftrightarrow O_2 + 4\ H^+ + 4\ e^- \tag{6}$$

$$2\ Cl^- \leftrightarrow Cl_2 + 2\ e^- \tag{7}$$

$$\text{Cathode: } 2\ H_2O + 2\ e^- \leftrightarrow H_2 + 2\ OH^- \tag{8}$$

As a result, negatively charged ions move towards the anode and positively charged ions towards the cathode, forming a significant pH gradient. This produces a change of the intracellular pH in surrounding tissues, which is ultimately the cause of cell death [113].

The ionized Na^+ and Cl^- also move toward anode and cathode, respectively. Once there, these ions react with the water inside the tissue, producing more chemical substances, such as sodium hydroxide at the cathode, and hydrochloric acid, oxygen and chlorine at the anode [46].

It is self-evident that all these processes are not only time-dependent, but significantly increase with increasing treatment time.

Substantial work on *in silico* modeling of electrochemical treatment was performed by Nilsson *et al.* in a series of studies [42, 114–116]. They portrayed ion transport in a defined zone near either cathode or anode by a quasi-1D model using the Nernst–Planck equations for ion transport under the hypothesis of electroneutrality:

$$\frac{\partial c_i}{\partial t} = D_i \nabla^2 c_i + \frac{zi}{|z_i|} u_i \nabla \cdot (c_i \nabla \varphi) + R_i \tag{9}$$

with c_i as concentration, D_i as diffusion coefficient, z_i as the electrical charge of the ion, u_i as the ionic mobility of the ionic species and R_i as the reaction rate.

Their earlier models employed a simplified medium made of physiological saline solution with determined buffer capacity and organic content.

Similar approaches have been proposed by other groups, where they used a model consisting in a 1D Nernst–Planck equation for ion transport in a four component electrolyte (Na^+, OH^-, Cl^-, H^+) and the Poisson equation for the electrostatic potential under galvanostatic conditions [117], without electroneutrality condition and consideration of a full cathode–anode ion transport interaction. With that, the following equations are to solve:

$$\frac{\partial c_i}{\partial t} = -\nabla \cdot J_i \tag{10}$$

$$J_i = -\mu_i C_i \nabla \varphi - D_i \nabla C_i \tag{11}$$

$$\nabla^2 \varphi = -\frac{F}{\epsilon} \sum_i z_i C_i \tag{12}$$

where C_i is the concentration of the ionic species i (i = Na^+, OH^-, Cl^-, H^+); J_i the flux of the ionic species i (moles passing through a unit of area per unity time), φ is the electrostatic potential, z_i and D_i are charge number, and the diffusion coefficient of the species i; $\mu_i = z_i D_i F/RT$ being its respective mobilities and ϵ is the absolute medium permittivity, with F being the Faraday constant, R the gas constant and T the absolute temperature. z_i are signed quantities, being positive for cations and negative for anions.

Their model, while simple, gave insight into current flow, thus ion transport and therefore pH fronts, which correlated with areas of cell death obtained from *in vivo* and *in vitro* data.

Many 2D and 3D models have also considered the spatial distributions of the electric field intensity (E), electric potential (φ)

and temperature (T) [118–120]. As pH changes have been identified as the main reason for cell death in EChT [113], a shift of focus on electrochemical processes [121], protein denaturation [122] and pH fronts during application [123] has taken place.

In EChT, the content of the electrolyte is of crucial importance. In living tissues, both the extracellular and intracellular space is highly regulated. Homeostasis is defined as the regulation of the dynamic stability of the intracellular space and is influenced by physiological processes such as respiration, blood circulation, and renal excretion. The body's buffering system is a key factor to maintain homeostasis. Including the buffering system into a model that deals with mass transfer is therefore an important factor to produce realistic simulations. An example of how the model outputs can look like is shown in Figure 6. This topic is discussed in more detail in the introduction of Chapter 5.

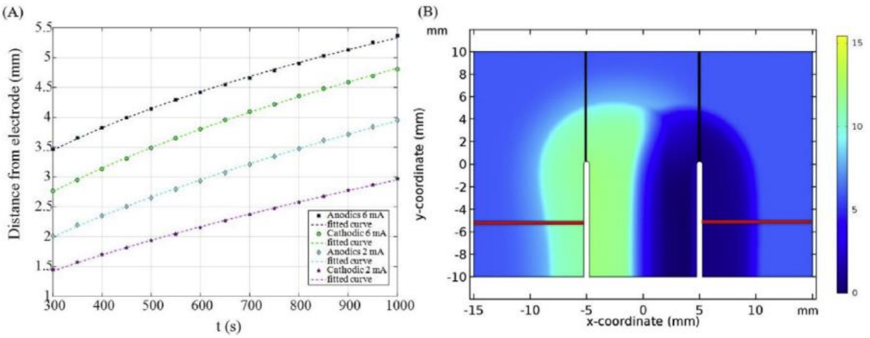

Figure 6: A: Time-dependent acidic and basic pH front distances from the electrodes of a two-electrode EChT for the applied currents 2 and 6 mA, obtained with a buffered model. **B:** Two dimensional pH distribution for a 6 mA buffered model after 1000s of simulation. Figure from [124].

In general, there are more biochemical aspects that can potentially play a role in EChT treatment outcome, such as metal release during the process and its addition to the toxicity [125] or the effects of an ionic layer on the electrodes during treatment, which may cause local electric field distortion, arcing, and possibly contamination of the system [126].

In summary, it can be said that the simulation of EChT typically involves solving for the potential and current density at the electrodes and in the electrolyte, respectively. The contributing species concentrations and the involved electrolysis reactions are considered to gain an understanding on the resulting mass transport and pH fronts. To do that, the Nernst-Planck equation, which accounts for the flux of solute species by diffusion, migration, and convection, is solved for the involving species in the electrolyte.

In vitro study on the mechanisms of action of E2

Chapter 3

3.1 Abstract

To investigate the underlying mechanisms of action of E2, an *in vitro* study in cells in suspension was performed. The goal of the experiments was to isolate the effects of the electrolysis and the electroporation components of the treatment. *In silico* experiments were additionally performed to determine the contribution of temperature increase during treatment application to the E2 effect. The results indicate that E2's cell killing mechanism is based on a combinational effect of electrolysis and reversible electroporation that takes place within the first two minutes after treatment. It was further shown that the E2 effect unfolds after a significant time delay. These observations suggest that cell death is induced in permeabilized cells due to the uptake of electrolysis species, which kill the cells via intrinsic pathways. Thermal simulations indicate a significant but harmless temperature increase.

This chapter was adapted from:

Klein N, Mercadal B, Stehling M, Ivorra A. In vitro study on the mechanisms of action of electrolytic electroporation (E2). Bioelectrochemistry. 2020 Jun 1;133:107482.

3.2 Introduction

The application of cell membrane electropermeabilzation has clinical relevance when it is paired with molecules that would otherwise not be capable of crossing the cell membrane by themselves. Pairing a chemotherapeutic drug with electroporation can effecticaly ablate cancerous tissue, a treatment which is known as Electrochemotherapy (ECT) [5]. A similar effect can be achieved by combining calcium with electoporation [32]. Pairing genetic material with electroporation is a novel application called Gene Electrotransfer (GET) [127].
All these clinical applications employ electroporation to facilitate the transport of molecules into the cells, instead of directly killing the cells. In order to achieve this effect, electric field magnitudes in the range of 1000 to 1500 V/cm are sufficient. A typical clinical ECT protocol uses 8 monophasic square pulses of 100 µs length. This is sufficient to effectively permeabilize the cell membranes within the target area while at the same time enabling enough bleomycin to enter the cell [128]. However, this protocol is not efficient enough for the successful uptake of larger molecules such as plasmids. Here, a typical protocol consists of a short (microseconds) high voltage pulse to electroporate the cells, and a longer (milliseconds) low voltage pulse to electrophoretically drag the material into the cell [129].

The working hypothesis of the mechanism of action of Electrolytic Electroporation is proposed to be similar to that of ECT, GET or Calcium Electroporation, where the pulse application is used to electroporate and transport molecules across the cell membrane, which would otherwise not be able to enter the cells in such high concentrations, or at all.
In contrast to the square pulses which are typically used in ECT or GET, E2 applies an exponential decay-like pulse (Figure 7A), which consists of an initial high voltage stage and a posterior low voltage stage. The initial stage is short in duration and intended to sufficiently reversibly electroporate all cells within the ablation area, while the posterior stage has two purposes: deliver enough current to induce electrolysis at the interface of the electrodes [52], and efficiently transport the electrolysis species across the cell membrane into the cell. The combination of the two components can kill all cells within the treatment area by employing only a few exponential pulses at low

initial electric fields, without the necessity to administer a molecule such as calcium or a drug.

As previously mentioned, the effects of E2 have been investigated in a number of pre-clinical studies [53–56, 130–132]. However, a deeper understanding of the mechanisms behind the method is still lacking. Lv *et al.* have published work on the primary cell death mechanisms of E2. Their conclusion was that the main modes of cell death are pyroptosis and necroptosis [16], both of which are types of programmed inflammatory cell death. While this gives insight into some mechanisms of the E2 effect, there is still not enough information on the entire process of the E2 mechanism.

The aim of this study was to quantify the contribution of electroporation and electrolysis in E2 treatments to help understand the modality better. A series of *in vitro* experiments were performed, where the contribution of each treatment component was isolated and quantified.

3.3 Materials and Methods

3.3.1 Cell culture and preparation

HEK-293 tsA201 cells were cultivated in DMEM (Life Technologies) with 10% fetal bovine serum (FBS, Life Technologies) and supplemented antibiotics (100 µg/mL streptomycin, 100 U/mL penicillin (both Life Technologies)). The cells were maintained in a humidified atmosphere at 5% CO_2 and 37°C, and routinely passed every two days. For the preparation of cell suspension, the cells were washed once with Dulbecco's Phosphate-Buffered Solution (DPBS, Gibco) and removed from cell culture plates employing a 0.25% trypsin-EDTA solution (Life Technologies). They were then centrifuged at 1,500 rpm for 5 minutes at room temperature. The cell pellet was resuspended in DPBS (Life Technologies) to a final concentration of 2.5 million cells per mL. Samples of 150 µL were exposed to the treatment protocols described in the following chapters.

3.3.2 Treatment protocols

This study was designed to investigate the roles of the different E2 treatment components. In total, three sets of experiments were performed.

In the first set of experiments, cells in suspension were exposed to treatment protocols and the time-dependent cell viability was monitored for up to 40 hours.

In the second set of experiments, the cell suspension was pipetted between gelified DPBS, where the gel was positioned between the electrode plates and the cell solution. The objective was to isolate the electroporation component by preventing the produced electrolysis species which were generated at the electrode plates from reaching the cells.

In the third set of experiments, in order to exclude the electroporation component in the E2 treatment, first the media alone (without cells) was treated with an E2 protocol and then the cells were exposed to the media to evaluate the impact of electrochemically generated molecules without pulse application.

In all experiments, E2 pulses were the product of free discharge of a capacitor across a pair of stainless steel electrodes. An additional 150 V/cm pre-pulse was applied to increase electrolysis production and to mimic the envisioned clinical procedure. Clinically, this pre-pulse will be applied to measure tissue conductivity prior to treatment. The IRE treatment protocol consisted of 120 pulses with a duration of 100 µs which were delivered at 1 Hz in trains of 10 pulses. Protocols for IRE, RE and E2 were delivered with a custom-built generator as previously described [56]. The applied currents were measured with a hall probe (Pintek PA-622, Pintek Electronics Co., Ltd.), while the voltages were measured with a high voltage probe (Pico TA044 High voltage probe, Pico Technology). The total applied charge was calculated retrospectively.

Table 3. Summary of experimental conditions and parameters. Exp ID = type of experiment (Exp ID 1 = conventional set-up, 2 = set-up with agar to exclude electrolysis impact, 3 = third set of experiments where only the media was treated). Applied treatment parameters were: E2: exponential decay pulse (Figure 7A) with additional 150 V/cm pre-pulse (*), mean time constant 3.49 ± 0.62 ms. Indicated E-fields are peak values. Surface charge density varies between Exp ID 1/3 and 2 due to dimensional differences. IRE: 100 µs pulse length, 1 Hz, delivered in trains of 10 pulses. RE: 100 µs pulse length, 500 V/cm, 1 Hz, delivered in trains of 8 pulses. Control: cells were handled and processed like the treated cells, but no treatment was performed on them.

Exp ID	**Treatment modality**	**E field magnitude (V/cm)**	**# Pulses**	**Surface charge density (C/cm^2)**	**Time in treatment chamber before incubation (minutes)**	**Time points of cell viability measurements (hours)**
1	E2	800	3 (+1*)	0.148	2,5,10,20,30,40	0.5, 8, 24, 40
1	IRE	1500	120	0.150	30	40
1	Control	-	-	-	2,5,10,20,30,40	0.5, 8, 24, 40
2	E2	800	3 (+1*)	0.201	1	40
2	E2	1000	3 (+1*)	0.222	1	40
2	Control	-	-	-	1	40
3	RE	500	8	0.004	30	40
3	E2	800	3 (+1*)	0.150	30	40
3	Control	-	-	-	30	40

3.3.2.1 Determination of tissue-dependent treatment effect of E2

For the first set of experiments, 150 µL of cell suspension was pipetted into a custom-made CNC-milled polycarbonate cuvette of the dimensions 10 x 6 x 4 mm (width, length, depth) with custom-made stainless steel (grade 316) electrodes of 1 mm thickness (width = 10 mm). Therefore, the distance between the electrodes was 4 mm. Cells in suspension were then treated with E2 or IRE pulse protocols. Treatment parameters are summarized in Table 3 (experimental ID (Exp ID) 1). Treatment parameters of E2 were chosen similar to those which were successful in previous *in vivo* experiments [56], while IRE and RE protocols were similar to protocols typically used in a clinical setting.

3.3.2.2 Isolation of electroporation component in E2

A second set of experiments (Exp ID 2 in Table 3) was conducted in which the impact of electrochemically generated species was excluded. An E2 pulse protocol was applied in a set-up designed to prevent the electrolysis products from reaching the cells. This was accomplished by separating the treated cells from the electrodes with a thin wall of gelified DPBS. DPBS was used to ensure uniform conductivity of the gel and the cell suspension.

15 g/L of agar was dissolved into DPBS, brought to boiling and then immediately filled into the petri dishes. The electrodes were then inserted into the gel. Finally, a small section between the electrodes was cut out where the cell suspension was pipetted in. Custom-made electrodes made of polished stainless steel (0.5 mm thickness) at a distance of 8 mm and a surface area of 30 x 5 mm² (width x length) were used for these experiments. Nylon spacers separated the two electrodes to stabilize the set-up.

The necessary minimum thickness of the gelified DPBS layer between the electrodes and the cell solution was calculated in advance to ensure no contamination of the sample by electrophoretically dragged species. This was performed by taking into account the electrical mobilities of the relevant ions. The electrical mobility is the ability of charged particles, such as ions, to move through a medium in response to an electric field that is pulling them. In such cases, the ion will be accelerated until it reaches a constant drift velocity according to the following equation:

$$\nu d = \mu E \tag{13}$$

where ν_d is the drift velocity [m/s], μ is the mobility [m²/V·s] and E the electric field strength [V/m].

The mobility of the sodium ion (Na^+) in water at 25°C is $5.19 \cdot 10^{-8}$ m²/Vs. That means that Na^+ in an electric field of 1000 V/m has an average drift velocity of $5.19 \cdot 10^{-5}$ m/s, which is 51.9 µm per second. Table 4 illustrates the distances the relevant ions will move at 1000 V/cm for 10 ms, which is the typical total length of an E2 pulse when applied to cells in suspension. Since the suspension was pipetted out of the cuvette immediately after pulsing, additional diffusion effects can be neglected. Protons (H^+) are the fastest ions. Even if H^+ ions immediately moved with constant maximum drift velocity, and when several pulses are applied, it is safe to say that a gel thickness of 2 - 2.5 mm is more than sufficient to prevent electrolysis species from reaching the cells.

Table 4: Mobility and drift velocity of ions which are present in a phosphate buffered saline solution (media of cell suspension during treatment application), as well as in the gel, and those expected to be generated through electrolysis at the electrodes (marked with ǂ [126]) [133].

Ion	**Mobility in water at 25°C /m²/Vs**	**distance at 1000V/cm in 10ms /µm**
H^+	$3.63 \cdot 10^{-7}$	363
Na^+	$5.19 \cdot 10^{-8}$	51.9
K^+	$7.62 \cdot 10^{-8}$	76.2
Cl^-	$7.92 \cdot 10^{-8}$	79.2
OH-	$2.06 \cdot 10^{-7}$	206
$H_2PO_4^-$	$5.91 \cdot 10^{-8}$	59.1
HPO_4^{2-}	$3.42 \cdot 10^{-8}$	34.2
Fe^{2+} ǂ	$5.6 \cdot 10^{-8}$	56
Fe^{3+} ǂ	$7.05 \cdot 10^{-8}$	70.5
Ni^{2+} ǂ	$5.6 \cdot 10^{-8}$	56
Cr^{3+} ǂ	$6.94 \cdot 10^{-8}$	69.4
Mn^{2+} ǂ	$5.54 \cdot 10^{-8}$	55.4

In order to physically and visually confirm that the thickness of the gelified DPBS is sufficient to prevent electrolysis species from reaching the cell suspension, a pre-experiment was carried out with the same set-up as described above (Figure 7B), but with liquid universal pH indicator (pH 3-10, JBL). Figure 7C visualizes the pH distribution one minute after treatment, which is longer than the time after which the cells in suspension are pipetted out in the experiment (treatment parameters: 1 pre-pulse at 150 V/cm, then 3 pulses at 1000 V/cm; total surface charge density applied 0.222 C/cm²). pH distribution is clearly visible, but the colored area is confined into an area around the electrode (approx. 1 mm).

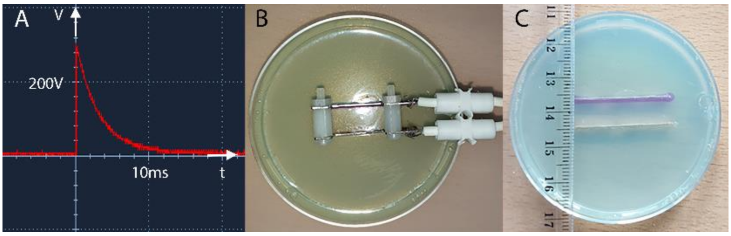

Figure 7: Experimental set-up of a set of experiments with gelified DPBS. A: Typical exponential decay pulse, as applied in E2 treatment. **B and C:** Set-up of experiment series 2 with gelified medium: **B:** Pre-test with a universal pH indicator to test the diffusion of ions in gel during treatment, with the treatment protocol (1x pre-pulse at 150 V/cm, 3x at 1000 V/cm, total surface charge density applied 0.222 C/cm²). **C:** picture was taken immediately after treatment, right picture (with the scale) was taken after 60 seconds, which is when the cell suspension is pipetted out of the petri dish after treatment.

3.3.3 Assessment of cell viability

After treatment, 100 µL of the cells in suspension was seeded on 24-well plates with 700 µL of media and incubated at 37°C until further assessment. At different time points (see Table 3) the cells were detached from cell culture plates (0.25% trypsin-EDTA solution) and centrifuged for 5 minutes (1,500 rpm at room temperature). The cell pellet was resuspended in 100 µL DPBS, and 10 µL of cell suspension was mixed with 90 µL trypan blue solution (T8154, Sigma-Aldrich). Cell concentration was quantified with a light microscope (CKX41, Olympus) and a Neubauer chamber (Laboroptik Ltd).

Since trypan blue only enters cells with an impaired membrane, this method can also be employed to assess membrane permeabilization. Thus, in one sub-set of experiments, cells were stained with trypan blue directly after the treatment and observed under a light microscope. All cell concentrations of treated cells are expressed relative to the results of sham-treated cells (= control) which underwent the same procedure but were not exposed to a treatment protocol.

In order to experimentally show that the dilution of 100 µL cell suspension with 700 µL media after the treatment is sufficient and that the electrolysis products within the media, including metal ions, do not have a strong negative effect on the cells during incubation, a pre-test was performed with cells which were exposed to a typical E2 treatment (1 pre-pulse at 150 V/cm, then 3 pulses at 1000 V/cm; total charge applied 0.15 C) with varying dilution factors during incubation: 100 µL of treated cells were pipetted into 700 µL, 2 mL, 5 mL, 8 mL and 10 mL of media. Statistical analysis revealed that increasing the dilution did not decrease cell viability (Pearson p=0.3). Based on these results, the dilution factor was kept minimal at 1:7.

3.3.4 Calculation of applied charge

E2 treatment consists of the free and total discharge of a capacitor through the sample (Figure 7A). To retrospectively calculate the total charge delivered to each sample, the current was measured and recorded with an oscilloscope (Owon SmartDS Sds7102V Oscilloscope, Fujian Lilliput Optoelectronics Technology Co. Ltd) with a hall sensor current probe (PA-622, Pintek Electronics Co. Ltd.). The total charge delivered is determined by the capacitors of the generator. For E2 treatments the total charge of a pulse, Q, was calculated by multiplying the initial voltage, $V_{initial}$, by the capacitance, C, of the capacitor:

$$Q_{E2} = CV_{initial} \tag{14}$$

For RE and IRE treatments with 100 µs long pulses, the charge was calculated as

$$Q_{IRE} = INL_p \tag{15}$$

where I is the measured current in amperes at the end of first pulse, N is the number of delivered pulses, and L_p is the pulse length.

3.3.5 Thermal simulations

Pulsed electric fields can produce heat, the amount of which is dependent on the applied pulse parameters such as pulse duration and electric field magnitude. A finite element solver (COMSOL Multiphysics 5.3) was employed to perform thermal simulations for a 3D model to rule out potential thermal damage during the application of E2.

With the goal to calculate a worst-case scenario in terms of temperature increase, the simulation was set-up with the following conditions: two parallel plate electrodes with properties identical to that of the designed experimental set-up of Exp ID 1, in a cuvette of the same dimensions as in the experiments, and further properties as described in Table 5. The finest standard mesh type in COMSOL was selected. First, the Laplace equation was solved to obtain the electric potential (V) distribution for the given geometry:

$$\nabla \cdot (\sigma \nabla V) = 0 \tag{16}$$

with σ as the conductivity. The model then employed a heat conduction equation with inclusion of the Joule heating source term (**J**·**E**=σ|**E**|^2), as previously described [19]:

$$\rho c \frac{\partial T}{\partial t} = \nabla \cdot (k \nabla T) + \sigma |\mathbf{E}|^2 \tag{17}$$

with ρ as the density, c as the specific heat at constant pressure and k as the thermal conductivity. The boundaries facing the polycarbonate cuvette were treated as thermal insulators, while the outer boundaries facing air were treated as external convective cooling at room temperature:

$$q_0 = h(T_{ext} - T) \tag{18}$$

Where q_0 is the convective heat flux, Text the external temperature and the heat transfer coefficient h is dependent on

$$h = h_{air}(L, p_a, T_{ext}) \tag{19}$$

with h_{air} as the heat transfer coefficient of air, L as the plate diameter (area/perimeter) and p_a as absolute pressure (here: 1 atm). Details on the calculation of h for an upside horizontal plate movement can be found in [20, 21]. Since the cell suspension has a water content of over 98%, the thermal properties were chosen to that of water (Table 3). The simulation was performed for the application of three consecutive 800 V/cm (320 V) pulses that were applied every 3 seconds (capacitance = 100 µF). These parameters represent the real worst-case scenario with regards to heat development that was applied in these *in vitro* experiments.

Table 5: Physical properties which were used in the numerical simulations.

Description	**Parameter**	**Value**	**Reference**
Initial voltage	V_0	320 V	-
Power supply capacitance	C	100 µF	-
Initial temperature	T_0	293 K	-
Decay constant	τ	0.0035 s	-
Stainless steel: Electric conductivity	σ	$7.4 \cdot 10^6$ S/m	[134]
Stainless steel: Thermal conductivity	*k*	15 W/(m·K)	[134]
Stainless steel: Density	ρ	8000 kg/m³	[134]
Stainless steel: Heat capacity	C_p	477 J/(kg·K)	[135]
Cell solution: Electric conductivity	σ	1.7 S/m	Obtained experimentally
Cell solution: Thermal conductivity	*k*	2 W/(m·K)	[136]
Cell solution: Density	ρ	997.8 kg/m³	[135]
Cell solution: Heat capacity	C_p	4181.8 J/(kg·K)	[135]
Cell solution: relative permittivity	ε_r	80	[135]

3.3.6 Statistical Analysis

All experiments listed as ID 1 and ID 3 in Table 3 were repeated five times, experiments of ID 2 were repeated three times. All cell viability measurements were repeated three times. Statistical analysis was performed using Prism GraphPad (GraphPad Software). The Mann-Whitney-Test was used to assess statistically significant differences in paired and unpaired continuous variables. This test was used to compare different treatment modalities to each other. The Kruskal-Wallis independent sample test was used to test whether the central trends of several independent samples differ from each other; this test was used to compare samples that experienced the same treatment but where treatment outcome was measured at different time points. A p value of $p < 0.05$ was considered statistically significant.

3.4 Results

3.4.1 Time-dependent treatment effect of E2

Cell viability after E2 treatment was measured 30 min, 8h, 24h and 40h after treatment (800 V/cm peak electric field at a delivered charge surface density of 0.15 C/cm²). In all cases, cell suspension was kept in the cuvette for 30min directly after treatment. Figure 8 shows the results. 30min post treatment, the cells were not affected by the E2 application (96.3 ± 3.1% compared to control). At 8 hours post treatment, the viability decreased to 54.3 ± 21.8% compared to control and kept decreasing up to 40 hours after the treatment, where it reached 1.2 ± 2.0%.

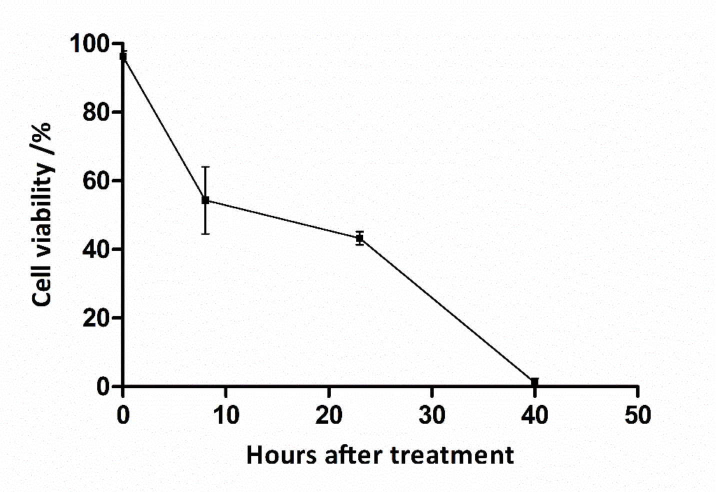

Figure 8: Time evolution of cell viability after E2 application. Applied E2 treatment protocol: 800 V/cm, total median surface charge density applied: 0.15 C/cm² (range: 0.12 - 0.16 C/cm²). Cell viability was measured with trypan blue staining at 30min, 8 hours, 24 hours and 40 hours after treatment. The results are presented as mean compared to control ± standard deviation.

3.4.2 The electroporation effect of E2

Membrane integrity was measured directly after treatment by means of trypan blue staining. Figure 9 shows that half of the cells display significant membrane permeability two minutes after treatment (51.9%), but that almost all cells recover their membrane integrity after 20 minutes (only 3.2% of cell show permeable membranes).

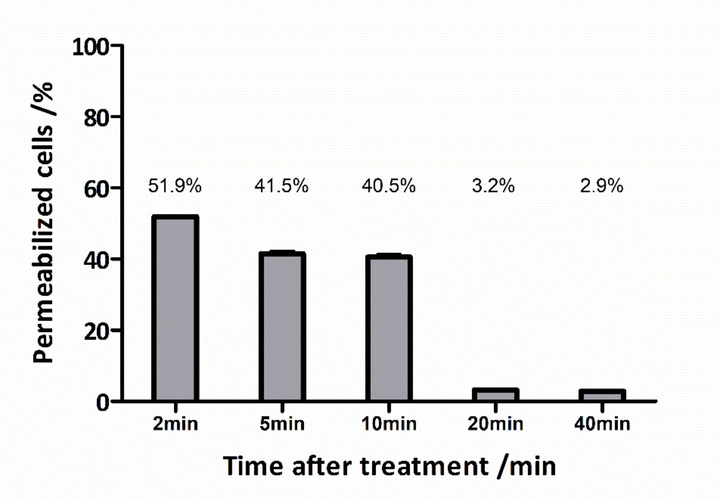

Figure 9: Permeabilization efficacy after E2 treatment. Percentage of cells that display trypan blue uptake over time compared to control.

3.4.3 Direct comparison between E2 and IRE

Cell viability after E2 and IRE treatments with similar charge delivered was measured. The E2 treatment protocol consisted of three exponential decay-like pulses with a peak E-field of 800 V/cm, and a pre-pulse of 150 V/cm, with a total applied surface charge density of 0.15 C/cm². IRE treatment protocol consisted of 120 pulses of 100 µs length and 1500 V/cm, delivered in trains of 10 at 1 Hz. Total surface charge density applied was 0.15 C/cm². This IRE protocol was chosen to mimic typically effective clinical application. Cell viability 40 hours after the treatments was 1.2% in E2 treated cells and 0.5% in IRE treated cells.

3.4.4 The effect of electrolytic species exposure to E2 treatment outcome

In order to investigate how severely the incubation of cells with the produced electrolytic products impacts the result, a set of experiments was conducted where the cells were left in the cuvette, together with the generated electrolytic products, for different amounts of time. The cells were left in the cuvette for 2, 5, 10, 20 and 40 minutes, during which they were fully exposed to the generated electrolysis products. After the respective time, they were handled as described in the materials and methods section. Figure 10 displays the results. At 40 hours post treatment, all cell suspensions showed comparable and not significantly different cell viabilities, which was 2% or less (Kruskal-Wallis-test p=0.4).

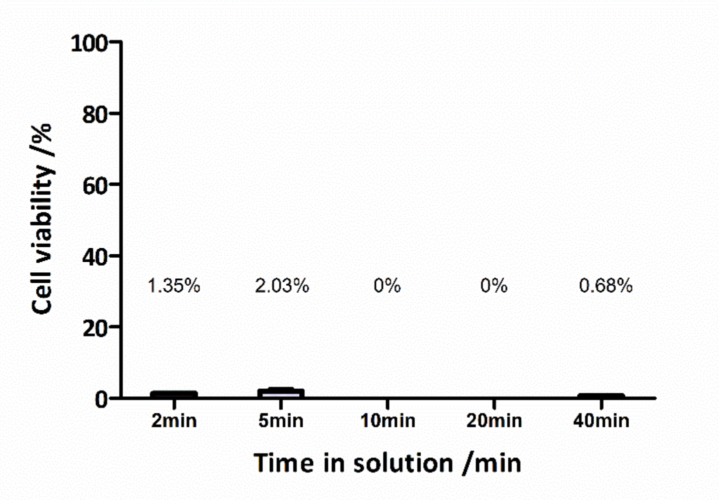

Figure 10: Cell viability after E2 treatment at 800V/cm for different incubation times. Cell viability was measured 40 hours after E2 treatment, where the cell solution was left in the cuvette for 2, 5, 10, 20 and 40 minutes, respectively. Displayed here is cell viability compared to control. There is no significant difference in cell viability (Kruskal-Wallis-test p=0.4).

3.4.5 E2 treatment effect without electrolysis

Figure 11 shows cell viability after E2 treatment and after E2 with gel layer between the cell solution and the electrodes (Exp ID 2). Figure 11A compares results at 800 V/cm, showing a significant (p=0.043) decrease of cell death when electrolysis products are prevented from reaching the cells. Figure 11B compares results of a treatment at 1000 V/cm, where the decrease is much less prominent, but still significant (p=0.034).

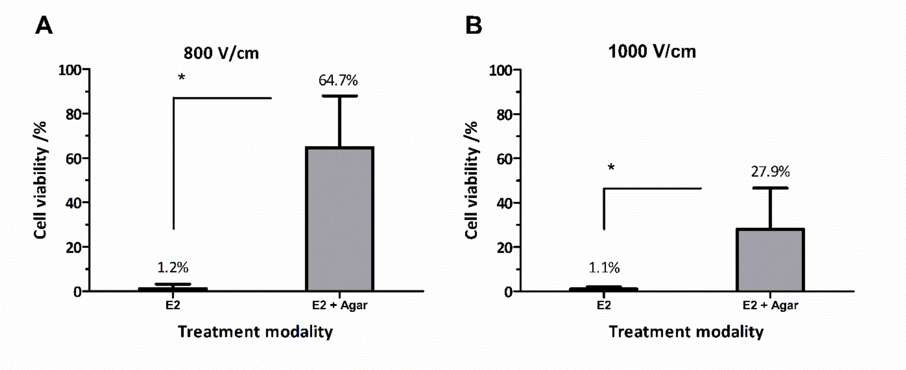

Figure 11: Comparison of E2 application with an E2 application where gelified DPBS layer prevented diffusion of electrolysis products into the solution. Cell viability was measured after 40h. **A:** Graph shows the E2 application at 800 V/cm (0.15 C/cm² for E2 and 0.2 C/cm² for E2 + agar) compared to control. **B:** Graph shows the application at 1000 V/cm (0.16 C/cm² for E2 and 0.22 C/cm² for E2 + gelified medium) compared to control. (*) indicates statistically significant differences ($p < 0.05$).

3.4.6 The role of electroporation in E2

In order to determine the role of membrane electroporation in E2, an experiment was conducted in which the culture media alone was treated, and then the cells were seeded in this media (Exp ID 3). The aim of this set of experiment was to quantify the effect of the electrolysis products when the cell membranes are not exposed to electroporation. Figure 12 shows the viability of cells seeded in media treated with reversible electroporation (RE) and E2 relative to control samples. Cell viability after 40 hours decreased after both treatments. Cell viability in the media treated with RE (8 square pulses of 100 µs length delivered at 1 Hz; calculated applied total surface charge density 0.004 C/cm²) was reduced on average by 35% compared to control, and by 53% in the media treated with E2 (total applied surface charge density of 0.15 C/cm²). No statistically significant differences were found between the RE and E2 groups.

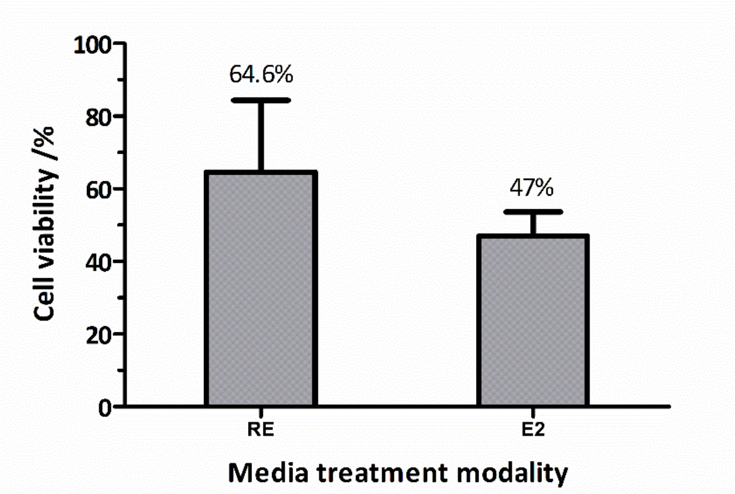

Figure 12: Results of an experiment where first the media was treated, and then the cells pipetted into the treated media. Cell viability measurements were performed after 40h. Treatment protocols were: **RE:** 8x 100 µs pulse at 500 V/cm, 1 Hz; total surface charge density of 0.004 C/cm². **E2:** 3 exponential decay-like pulses with a peak E-field of 800 V/cm and surface charge density of 0.15 C/cm². Cell viability is shown compared to control in percent. Comparison of the two treatments showed no statistically significant differences, p = 0.12.

3.4.7 Thermal aspects of E2 application

Numerical simulations were performed to investigate the temperature increase during E2 treatment in the *in vitro* setting described for experimental set-up Exp ID 1. The temperature evolution during the application of three consecutive E2 pulses at 800 V/cm (applied every 3 seconds) and 100 µF were computed. The results are presented in Figure 13. As expected, the temperature increases after each pulse. With 293K as the initial temperature, the temperature in the cell suspension increases to 298K (24.85°C, Figure 13A). The suspension then cools down to 296.4K (24.4°C) before the second pulse at t = 3s. Ten milliseconds after the second pulse at t = 3.01s, the maximum temperature in the suspension reaches 301K (27.85°C, Figure 13B). The system cools down to 300K before the third pulse. After the final pulse, maximum temperatures of 304K (30.85°C) are reached within the treated area (Figure 13C), which is a total increase by 11°C compared to the initial value. By t = 9s, the temperature of the system was homogeneously distributed at 302K (Figure 13D).

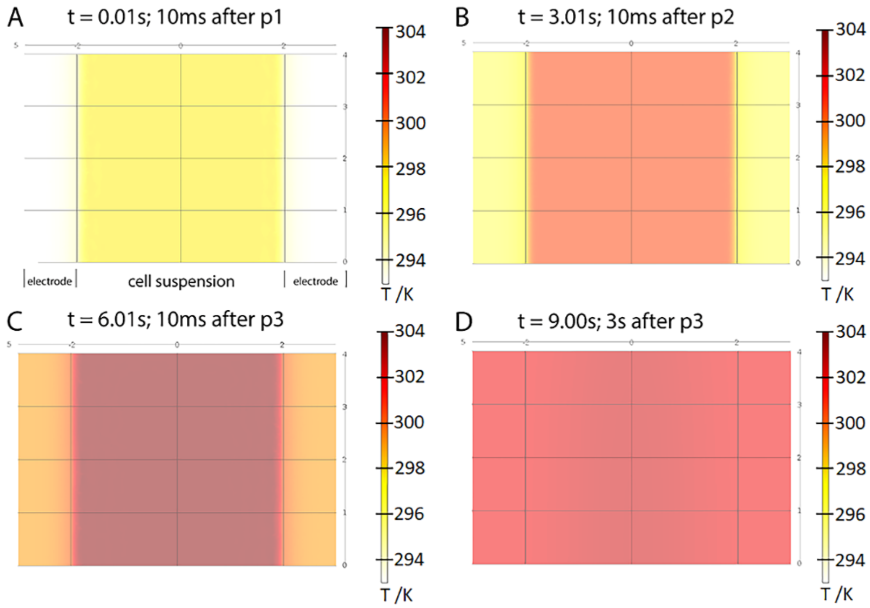

Figure 13: Calculated heat distribution of E2 application. Figure shows the axial cut of the electrode and cell suspension system. **A**: Results after the first pulse at 10ms. Overall temperature of the cell suspension increased from 293K to 298K. **B:** Results at 10ms after the second pulse (t=3.01s). The maximum temperature reached was 301K. **C:** Results 10ms after the third pulse (t=6.01s). The cell suspension reached maximum temperatures of 304K (30.85°C). **D:** 3s after the final pulse, (at t=9s), the cell suspension has cooled down to 302K.

3.5 Discussion

This study was conducted to better understand the underlying mechanism of E2. The goal was to assess the interplay between the two components of E2: electroporation and electrolysis.

Experimental results shown in Figure 8 illustrate the time-dependent, gradual lethal effect of an E2 application. Congruent with pre-clinical results in rat liver, the process of cell death starts with a delay [137].

It was shown that a short exposure to electrolysis products is sufficient for E2 treatment success (Figure 10). This aspect of E2 is important from a clinical perspective, as there are perfusion processes during *in vivo* application, which would generally hinder high amounts of electrolysis products to remain within the target tissue. With regards to electrolysis exposure and its treatment effect, the *in vitro* results illustrated here are comparable to previous pre-clinical studies in porcine liver, where electrolytic products also did not remain in the cellular environment for long, but the E2 effect was still clinically impactful [56].

To further explore the effects of the electrolysis component in E2, experiments were performed in which first the medium was treated and then the cells were pipetted into the treated medium for exposure of electrolysis species without involvement of the electroporation component (Figure 12). The results illustrate how electrolysis had an impact of approximately 50% in terms of cell viability reduction. On the other hand, experiments with gel were performed in which it was effectively prevented that the electrolysis products produced at the electrode surfaces reached the cells in suspension. The results in this case show that electroporation at 800 V/cm without the electrolysis component had a treatment efficiency of only 35% (meaning that the majority of cells survived), while at 1000 V/cm, the treatment efficiency was approximately 70% (Figure 11). From an E2 application perspective, 1000 V/cm is significantly above the *in vivo* threshold for electric fields, since it was shown in pre-clinical studies that the application of 667 V/cm is sufficient to produce continuous lesions is tissue [55, 56]. It is known that *in vitro* E-field thresholds tend to be higher than *in vivo* [138]. Therefore, it comes to no surprise that the effective E-field applied here is 800 V/cm as compared to the *in vivo* threshold of 667 V/cm.

For recapitulation, Figure 14 compares the efficacy of a regular E2 treatment with that of an equivalent E2 treatment in which electrochemically generated species are excluded (EP effect) and that of an equivalent E2 treatment in which the electroporation component is excluded (electrolysis effect). The results strongly suggest that the cell killing effect of a typical E2 treatment is due to a synergistic effect between the electrolysis and the electroporation components.

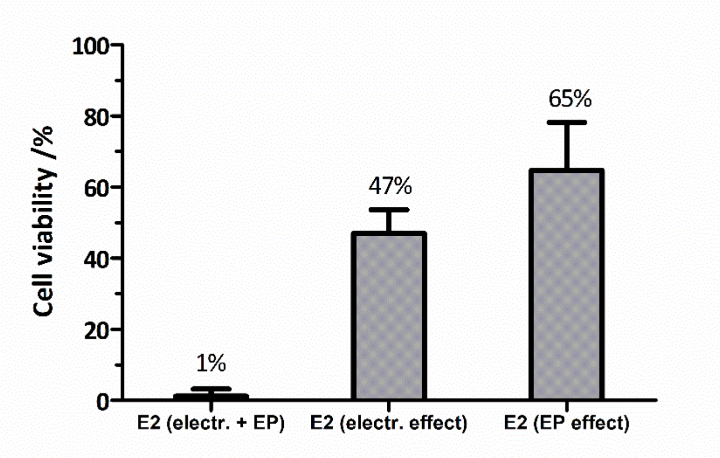

Figure 14: Direct comparison of E2 application and its different components. Treatment parameters: 3 exponential decay-like pulses with a peak E-field of 800 V/cm, and a pre-pulse of 150 V/cm; total surface charge density applied 0.15 C/cm². Measured after an incubation time of 40 hours. **E2 (electrolysis + EP):** treatment application with the above parameters without any modifications. The combination of electrolysis and electroporation (EP) is applied. **E2 (electrolysis effect):** Result of the experiment summarized in Figure 12, where cells are not exposed to electroporation. The media was treated with the protocol described above, and afterwards the cells were pipetted into the media. **E2 (EP effect):** Result of the experiment summarized in Figure 11, where the cells were not exposed to electrolysis. A gel layer prevented the generated electrolysis species to penetrate the treated cell solution.

It could be argued that, to some extent, the observed treatment effect (i.e. relative decrease in cell viability), in particular the results shown in Figure 11 and 12, may not be due to cell death caused by the treatment itself, but due to disturbed cell proliferation during the incubation period by the remaining electrolysis species in the buffer.

This assumption would be in alignment with the fact that cell proliferation rates in HEK-293 cells are known to be up to 32 hours [139]. Effects that reduce cell proliferation rates have been shown in several studies on Electrochemical Treatment (EChT) in cell suspension [140–143]. The anti-tumor effect has mainly been ascribed to the severe pH change, the degree of ionization and cell cycle control. Work of other groups has assigned similar effects to metal release [125]. In general, such effects are possible in E2 application, because E2 is known to have elements of impactful pH changes [50]. Additionally, the use of stainless steel electrodes, as performed in this study, will cause an increase of Fe^{2+} and Fe^{3+} concentrations within the treatment field [125]. Therefore, it may be possible that both pH changes and increased metal concentrations in the cell suspension were potential causes of an arrest in cell proliferation.

What counteracts this argument is the fact that it was shown in pre-tests of this study that the dilution factor was sufficient enough to guarantee that the E2 treatment effect did not occur during incubation with extracellular electrolysis products. This indicates that the cell viability decrease, whether via a direct cell killing mechanism or an effect on cell proliferation, was due to intracellular processes after treatment, rather than due to extracellular factors. In context of the proposed E2 mechanism, which includes electroporation of cell membranes, this hypothesis makes sense, as the electrolysis species were most likely being admitted into intracellular space while the membrane was permeable (Figure 9), where they were possibly able to initiate intracellular cell death mechanisms. This hypothesis will be investigated and discussed in more detail in Chapter 5.

To understand the role of temperature increase during E2 treatment, simulations of a worst-case scenario were performed (Figure 13). The results show that the temperature can increase by 11°C in total. Similar results were already reported for various electroporation-based treatments [144, 145]. It is known that permanent tissue damage can occur instantaneously due to temperatures above 90°C, but also chronically with temperatures above 45°C when the temperature is elevated in a specific period of time. The temperature threshold as well as the necessary minimum time depends on cell or tissue type. In this case, the temperature has not exceeded 304K or 31°C, which is within the acceptable temperature for cells in solution

[146]. Furthermore, since thermal necrosis takes place directly after treatment, and no instantaneous (i.e. 30 minutes) decrease in cell viability could be observed in these experiments, it can be concluded that the temperature increase, while significant, did not lead to cell death.

Direct comparison of the standard E2 protocol to a typical clinical IRE treatment protocol reveals comparable outcomes. While the same amount of charge was applied, E2 application was at a much lower peak electric field strength (800 V/cm compared to 1500 V/cm) and severely faster (a total of 4 pulses was applied, compared to 120 pulses) than the IRE counterpart. Both of these are clinical advantages of E2: the efficiency at lower E-fields allows for large treatment areas without the induction of severe plasma formations, which happen at high voltages and high pulse numbers [85]. Additionally, time is one of the critical factors in clinical settings. E2 has similarities to other techniques that employ reversible electroporation, such as Electrochemotherapy or Calcium Electroporation. The key difference, however, is that the additional application of a substance is not necessary. Instead, the relevant toxic products are produced within the treatment area during the treatment. This can generally reduce risks and adverse events that arise when applying additional substances.

3.6 Conclusion

This *in vitro* study with HEK-293 cells in suspension had the goal to investigate the underlying mechanisms of Electrolytic Electroporation (E2). The results indicate that E2's cell killing efficacy is due to a synergistic effect of electrolysis and reversible electroporation that takes place within the first two minutes after E2 application. Experiments which isolated the two components showed that prevention of contamination by electrolysis products in cell solution significantly decreased treatment efficacy. The hypothesis that E2 treatment efficacy is not purely due to electrolysis, but enhanced by electroporation, was further reinforced by showing that only half of cells died due to the electrolysis products when solely the media was treated with E2, whereas when cells were treated directly, treatment success was almost 100%. The E2 treatment effect was delayed, which is congruent with previous studies on E2. A possible explanation is that cell death induction is due to electrolysis species uptake during the treatment, which leads to a delayed intracellular response via intracellular processes and ultimately to regulated cell death. Thermal simulations revealed a substantial temperature increase which was still below the threshold for necrotic effects. Further investigation is necessary to understand what triggers the intracellular mechanisms that lead to cell death, parts of which will be discussed in Chapter 5.

Different electrode arrays for the ablation of large tissue volumes

Chapter 4

4.1 Abstract

Previous pre-clinical studies on the application of E2 have implied that it is possible to ablate big volumes of tissue in liver in a very short time and with only a few electrodes. The goal of this *in vivo* study was to test a variety of electrode configurations for the E2 treatment of large tissue volumes.

Twenty-seven lesions were performed in healthy porcine liver of five female pigs. Four, two and bipolar electrode-arrays were used to deliver various E2 treatment protocols. Liver was harvested approx. 20h after treatment and examined with H&E and Masson’s trichrome staining, and via TUNEL staining for selective specimen. All animals survived the treatments without complications. With four electrodes, a lesion volume of 35 x 35 x 35 mm can be achieved in less than 30s of treatment time. The prototype bipolar electrode created lesions volume of 50 x 18 x 18 mm in less than 10s. Parameters for two-electrode ablations with long exposures encompassing large veins were found to be good in terms of vessel preservation, but not optimal to reliably ablate all cells in the area between the electrodes.

This study demonstrates the ability to produce large continuous lesions in liver within seconds at lower limits of the E2 parameter space using different electrode configurations. The results indicate a charge-dependency of the application. The applicability of E2 for single electrode ablations was demonstrated with bipolar electrodes. Parameters for large 4-electrode ablation volumes were found suitable, while parameters for two electrodes still need optimization. However, since the parameter space of E2 is large, it is possible that for all electrode geometries optimal application protocols for specific tissues will emerge with continuing research.

Part of this chapter was adapted from:

Klein N, Guenther E, Botea F, Pautov M, Dima S, Tomescu D, Popescu M, Ivorra A, Stehling M, Popescu I. The combination of electroporation and electrolysis (E2) employing different electrode arrays for ablation of large tissue volumes. Plos one. 2019 Aug 22;14(8):e0221393.

4.2 Introduction

In a clinical context, the decisive advantage of electroporation-based therapies is the fact that they affect only the cells in tissue and spare the extracellular matrix. This can be considered advantageous for many clinical applications, in particular for treatment of tumors near sensitive structures such as blood vessels or nerves [20], as it is possible to kill cells within tissue structures while preserving the structural integrity of the tissue, making it possible for them to be repopulated with healthy cells [20].

Irreversible Electroporation has gained clinical success because of this property [147], but also due to its non-thermal mechanism and the fact that it does not require the application of drugs. However, a drawback of the IRE procedure is the requirement of very high electric field strengths, in the order of 1500 to 2000 V/cm, and the application of hundreds of pulses (e.g. 90 to 100 pulses between each electrode pair) over a typical procedural period of 30 min with strict limitations regarding distance and parallelism of electrodes. This results in restrictions with respect to the resulting lesion size.

Another drawback is the requirement of deep muscle relaxation, as it induces muscle contractions [24]. These muscle contractions may cause significant movement of the electrodes during treatment, resulting in possible complications [28]. The likelihood of complications increases with number of contractions, i.e. number of delivered pulses. The problem of muscle contractions has been partially solved by developing High-Frequency IRE (HFIRE), which employs the same technique but at a higher frequency and higher electric field magnitudes. However, a small amount of muscle relaxant is often still required [31], and management of high electric fields and strict electrode placement rules still apply in HFIRE.

Another challenge that arises with electric fields of 1500 V/cm or above is that they will almost inevitably spark the gases that are produced during the treatment [85], causing a pressure wave (referred to as discharges, sparks or arcing) with severe acoustic manifestation and mechanical tissue damage. Even when stopped early on, this phenomenon can cause low-impedance situations, resulting in machine failures and prolonged treatment times.

As discussed in detail in Chapter 2, it has been shown that Electrolytic Electroporation has advantages over tissue ablation by either electroporation or electrolysis alone, such as requiring substantially fewer electric pulses (typically ≤ 5 pulses, depending on lesion size) and lower electric field strengths (typically ≤ 1000 V/cm). At the same time, E2 is non-thermal and tissue selective like IRE, and does not require the application of drugs.

Previous E2 studies have addressed protocols for successful ablation with one electrode pair at relatively short exposure lengths, thus limited ablation volumes. This study was designed to test E2 treatment protocols that can successfully ablate large volumes of tissue employing different electrode geometries. Additionally, large lesions in areas which are usually classified as untreatable with thermal modalities (i.e. near large vessels) were targeted.

4.3 Methods

4.3.1 Ethical approval

The experiments were performed in compliance with all ethical and legal rules as stated by the national legislation and the European Union (program number 327). The experimental protocol was reviewed and approved by the Ethics Committee of Fundeni Clinical Institute as well as by the Bucharest Sanitary-Veterinary Authority (no 316).

4.3.2 Animal model and preparation

The study was carried out *in vivo* on three 40 kg and two 30 kg breed female pigs, as previously described [55]. In short, after the animals were fasted for 24h, they were medicated with a combination of acepromazine (0.5 mg/kg, Vetoquinol S.A., France) and ketamine (15 mg/kg, Gedeon Richter Plc., Hungary), which was injected intramuscularly prior to treatment. Anesthesia was induced intravenously with Propofol at a concentration of 2.5mg/kg and 0.1mg Fentanyl (Chiesi Pharmaceuticals GmbH, Austria). After endotracheal intubation was performed, anesthesia was maintained with sevoflurane in 80% O2 (adjusted to 2-2.5% Endtidal sevoflurane, Abbvie, Italy). In case of postoperative pain, the animals were treated with morphine (Zentiva S.A., Romania) at a concentration of 0.1 mg/kg, applied intramuscularly, and ketoprofen 1 mg/kg (S.C. Terapia S.A., Romania). Cefazolin 25 mg/kg (Biochemie GmbH, Austria) was applied intravenously in 2h intervals. The pigs were placed in a ventral side-up position, and the liver was exposed with an upper midline incision continued with a right transverse incision.

4.3.3 Treatment protocol

The pulses were delivered using 3 types of electrodes: 1) 18-gauge or 16-gauge stainless steel needle-type electrode with a variable exposed length of 1 – 4 cm exposed treatment length (Inter Science GmbH, Switzerland); 2) A 13-gauge stainless steel needle-type electrode (IGEA, Italy); 3) A simple, custom-made bipolar electrode, employing 2 shifted 18-gauge electrodes with an insulated gap between.

All treatments and treatment parameters are listed in Table 6. All sets of parameters were tested a minimum of 2 times in healthy pig liver. Total number of lesions was 27.

Table 6: Relevant parameters for the experiments which were conducted in this study. * in these cases, a total of 10 waveforms were applied, where the first 6 were between all electrode pairs at 1400 V, and the last 4 were between the peripheral electrode pairs at 1000 V. UA = uniformly ablated treatment area.

No. of probes	d /mm	E /mm	C /µF	Di /G	U /V	Pulse protocol	Lesion size / uniformity	Fig.
4	15	30	293	18	1400, 1000	6+4*	39x37x35mm, UA	2
4	15	20	193	18	1200	6	Not bridged	3
4	15	30	293	16	1400, 1000	6+4*	26x26x35mm, UA	S1 Fig
2	20	30	293	18	1500	2	30x30mm, UA	4
2	20	30	293	13	1600, 1500	2	Not bridged	5
2	15	30	193	13	1500	2	35x21mm, UA	S2 Fig
2	angular	30	293	13	1000, 1200		15x20mm, UA	S3 Fig
Bipolar	15	10	293	18	1200, 1100, 1000	3	50x13mm, UA	6
Bipolar	15	15	193	18	1200	3	Not bridged	S4 Fig

In all cases the electrodes were placed in the liver under ultrasound guidance (Hi Vision Preirus Ultrasound device, Hitachi Medical Systems, Germany). In all experiments except one, custom made grids and spacer were used to stabilize the electrode array and ensure distance and parallelism between electrodes (Figure 15B). In the one exception, explicitly non-parallel behavior was tested. The oscilloscope (Owon SmartDS Oscilloscope, Fujian Lilliput Optoelectronics Technology Co., Ltd, China) trace in Figure 15A illustrates a typical E2 waveform, which is made by the first part of the E2 wave that has the primary objective to induce electroporation, followed by a low voltage part to induce electrolysis. the E2 waveforms were the product of free discharge of a capacitor (of specific capacitance and charged to a specific voltage) across a pair of electrodes in tissue.

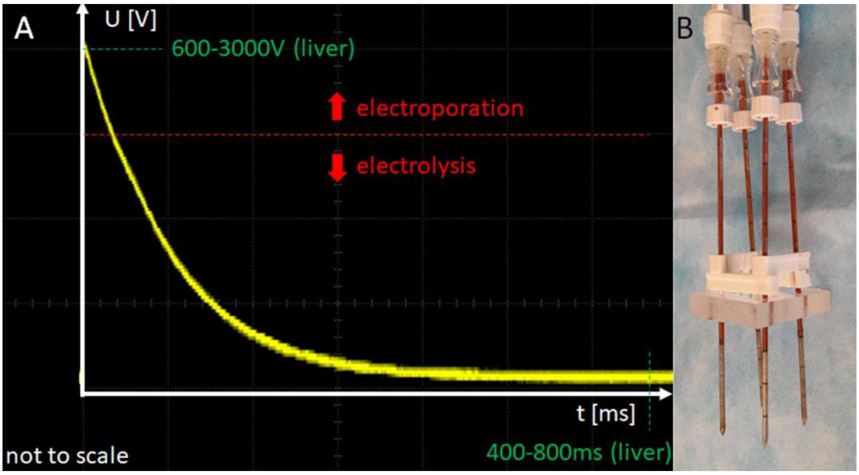

Figure 15: Typical E2 waveform and electrode configuration. A: Outline of a typical E2 waveform in liver tissue. It consists of an initial high-field electroporation phase (600 – 3000 V) and a 400 – 800 ms long, continuous low-voltage tail which transports the produced electrolysis continuously from one electrode to the other (Nernst-Planck type driven diffusion). What parameters are applied depend on the tissue and the electrode geometry. **B:** A typical 4-electrode configuration, employing 18-gauge electrodes at a distance of 15 mm.

4.3.4 Histopathological assessment

After the procedure, the pigs were kept alive for 18 - 23 hours, after which the liver was harvested and the animal was sacrificed using KCl 7.45% 1 ml/kg (B. Braun, Germany). The liver harvesting procedure was carried out under general anesthesia and is described in detail in [55]. After liver harvest, it was immediately perfused with saline solution and a 10% formalin fixative was perfused in the same way for approx. 10min. All lesions were cut out with normal surrounding parenchyma and stored in formalin solution. The tissue was then bread loafed and put in cassettes, which were routinely handled with 10% phosphate buffered formalin for 8 - 10 hours, photographed and embedded in paraffin blocks. For microscopic evaluation, 3µm sections were cut from each paraffin block and stained either with hematoxylin & eosin or Masson's trichrome staining. TUNEL staining was only performed in selected slides. The staining and scanning was performed by a pathology service provider (HistoWiz Inc, USA), as per their tissue preparation protocol for sectioning and staining. Whole slide scanning (up to 40x magnification) was performed completed with an Aperio AT2 (Leica Biosystems). Microscopical analysis was performed separately by two scientists trained in the field of liver tissue ablation. At least three sites per slide in the area of the electrode, in the middle between the electrodes, and the border between treated and untreated areas (if applicable) were reviewed and analyzed. Additionally, at least two vessels enclosed in the treatment area were evaluated per slide.

4.4 Results

4.4.1 E2 ablation with a four-electrode array

Figure 16 shows macroscopic and microscopic clinical results obtained with four electrodes. The electrodes were in a parallel square alignment 15 mm apart (held by a spacer) with 30 mm stainless steel exposure length. The electrodes had a diameter of 18G. Pulse protocol included that each pair had a potential difference of 1400 V and the capacitance was 293 µF. To add more electrolysis, another pulse round (without the diagonal electrode pairs) was delivered with the same capacitance but a decreased applied voltage of 1000 V. Figure 16 shows that this protocol produced a continuous lesion of approximately 35 x 35 x 35 mm. The total delivery/recharge time was less than 30 seconds, with a 30 second delay between the two rounds due to manual export of oscilloscope data. The lesion shown in Figure 17 followed the identical protocol with different electrodes (16G) and displays similar clinical results with slightly smaller outer dimensions.

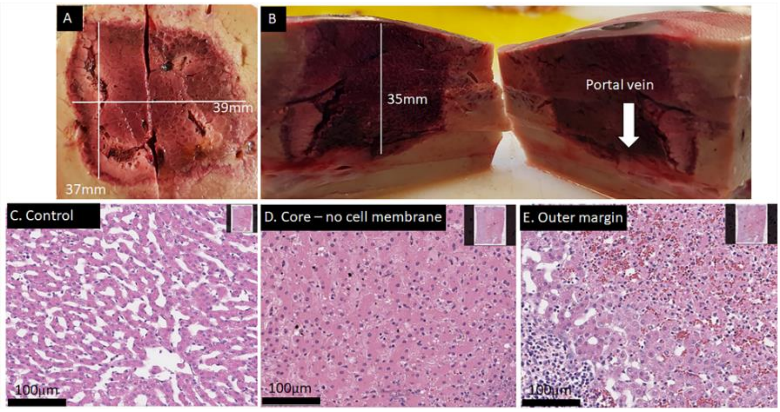

Fig 16: Example of a successful 4-electrode array ablation using a total of 10 waveforms in less than 30s total delivery and recharge time. Liver harvest was 18h post treatment. The lesions size is approx. 39x37x35mm. **A+B:** Gross pathology and lesion dimensions. **C:** H&E staining of an untreated area. **D:** H&E staining of an area in the middle of the lesion (core region). Sample shows cell death throughout, with a mixture of severe apoptosis and complete hepatocellular necrosis. **E:** H&E staining of the outer margin with a sharp transition of completely dead tissue (upper right corner) to apparently unaffected (or already regenerated) liver tissue (lower left corner).

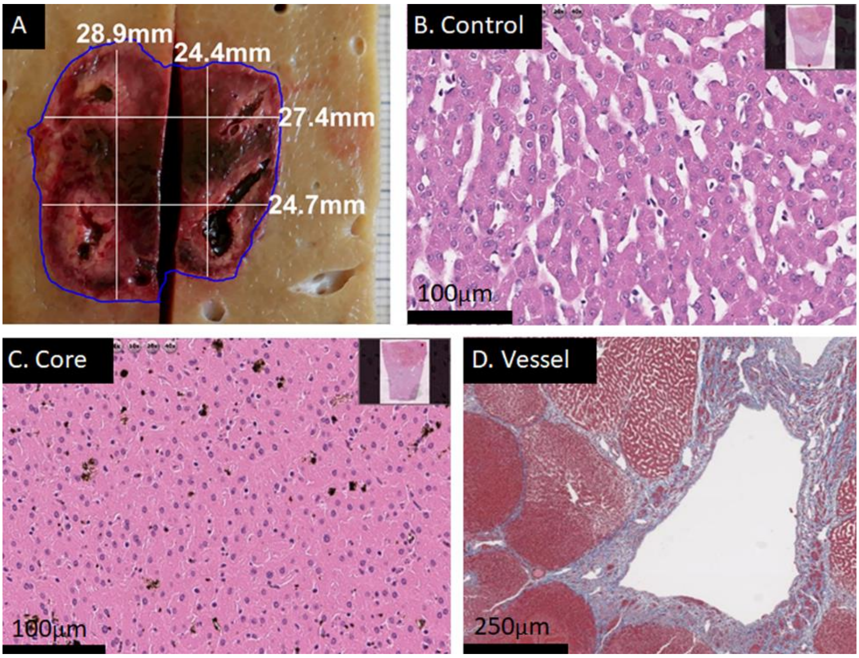

Figure 17: Example of a successful 4-electrode array ablation using a total of 10 pulses. Analog ablation to the one shown in Figure 16. While the electrical and geometrical parameters were identical, E2 electrodes of 16G diameter were used, which allowed for approx. 20% less charge to be delivered in the same amount of time. Liver harvest was 22h post treatment. **A:** Gross pathology of the lesion, showing approximate lesion dimensions of 26x26x35mm. **B:** H&E stained control area at 20x magnification. **C:** H&E stained tissue sample at 20x magnification from the core region, showing complete ablation, congruent with macroscopic impression. **D:** H&E stained tissue sample at 10x magnification from the core region, showing a large vessel. Cellular elements of vessels appear ablated. However, the fibers support the tissue infrastructure sufficiently to maintain its function.

Figure 18 shows and application of four electrodes which resulted in partial ablation. 1200 V were employed for the same geometry as described in Figure 16, but instead of 6+4 pulses, only 6 pulses (all electrode pair permutations) were applied. Both the maximum electric field as well as the total charge (per volume tissue) were lower than in the cases presented in Figure 16 and 17. While some areas appear completely ablated (Figure 18C), there are areas in the middle of the ablation zone which were only partially ablated (Figure 18D and E).

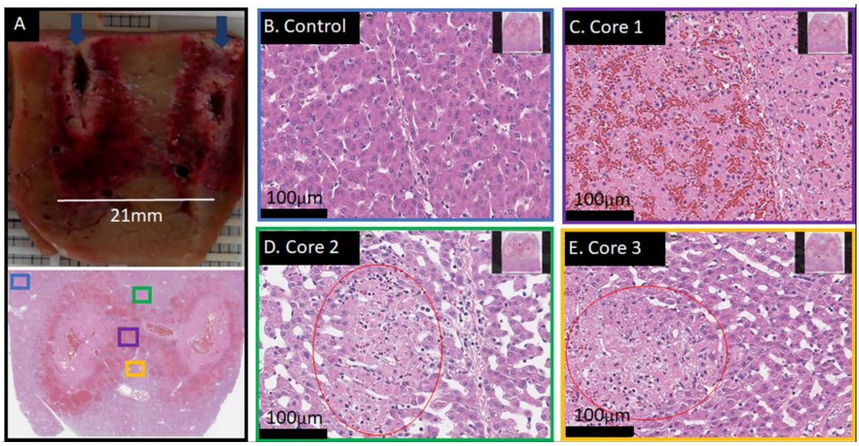

Figure 18: A 4-electrode array ablation with insufficient treatment outcome. Treatment parameters the same as shown in Figure 16. Liver harvest was 22h post treatment. Six pulses at 1200 V (every pair once) were delivered in total. **A:** Gross pathological cut between two electrodes of a 4-electrode array ablation. Only within a thin path which connects the two electrodes, complete cell death is found. Dark blue arrows indicate direction of electrode track. **B:** Control, H&E stained at 20x magnification. **C:** H&E staining of the sample at 20x magnification, illustrating the purple area shown in A. Within the thin path, cells are completely dead. **D and E:** H&E stained samples at 20x magnification of the outer areas (green and yellow boxes in A, respectively) at the core of the lesion, which are effected and show "patches" of dead cells (red circles) throughout.

4.4.2 E2 ablation with a two-electrode array

Examples of a complete ablation between two electrodes is shown in Figures 19 and 20. The lesion in Figure 19 was obtained with two pulses at 1500 V and 293 µF, at a distance of 20 mm and exposure length of 30 mm. For the lesion in Figure 20, the same parameters were applied, however at a distance of 20 mm. Here, the damage appears to show less signs of necrosis and structural loss compared to Figure 19, possibly due lower applied voltage and charge.

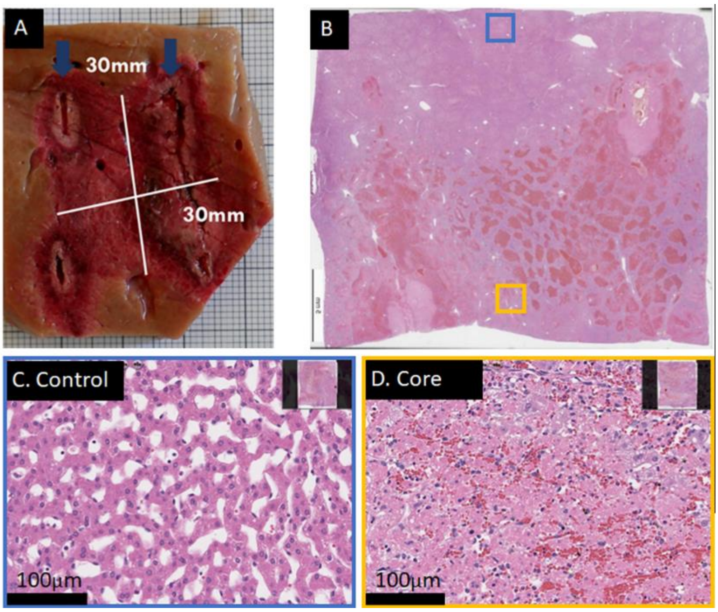

Figure 19: Successful 2-electrode ablation. There was a distance of 20mm between the electrodes, with an exposed length of 30mm and custom-made electrodes of 18G diameter, using 2 pulses of 1500 V peak voltage. Total time required was approx. 5s. Liver was harvested 23h post treatment. **A:** The outline of the macroscopic coronal cut, showing the area between the electrodes. Dark blue arrows indicate direction of electrode track. **B:** H&E staining of the upper part of the lesion. **C:** H&E stained control area at 20x magnification, blue insert in B. **D:** H&E stained area at 20x magnification from the core region (yellow insert in B). Severe cell death is found throughout the lesion. Note that the sample was cut out of plane, hence there is no perfect match between macroscopic and microscopic images.

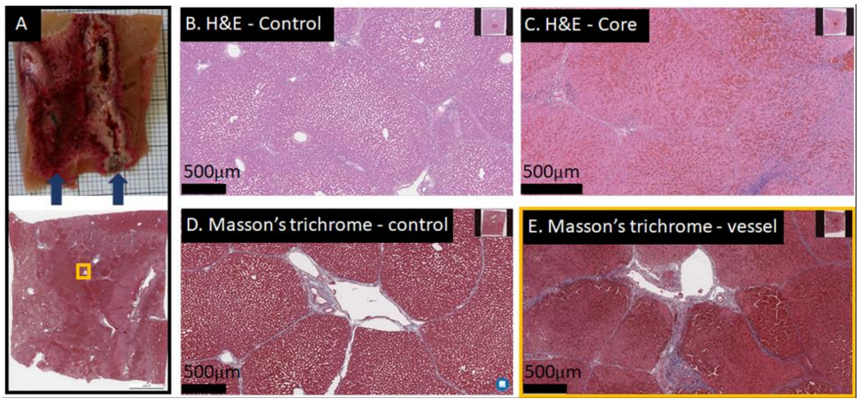

Figure 20: A successful 2-electrode lesion performed at 1500 V in less than 5 seconds. The parameters were 2 pulses at 1500 V, 15 mm distance, 30 mm exposure length with 13G diameter electrodes. Liver harvest was 22h post treatment. **A:** Macroscopic lesion (top), and Masson's Trichrome staining of the entire lesion (bottom). Dark blue arrows indicate direction of electrode track. **B:** H&E stained control area at 4x magnification. **C:** H&E stained tissue sample at 4x magnification from the core region, showing complete cell death throughout the area. **D:** Masson's trichrome staining at 4x magnification of an untreated area. **E:** Masson's trichrome staining at 4x magnification of an area in the middle of the treatment field (yellow insert in A) were several vessels were present. All vessels showed an intact vessel structure, while all surrounding cells were ablated.

An example of insufficient E2 parameters is shown in Figure 21. It should be noted that in this case the applied pulses were cut-off too early by the software and not completely delivered, resulting in approx. 30% less charge per volume being delivered, compared to the lesion shown in Figure 19.

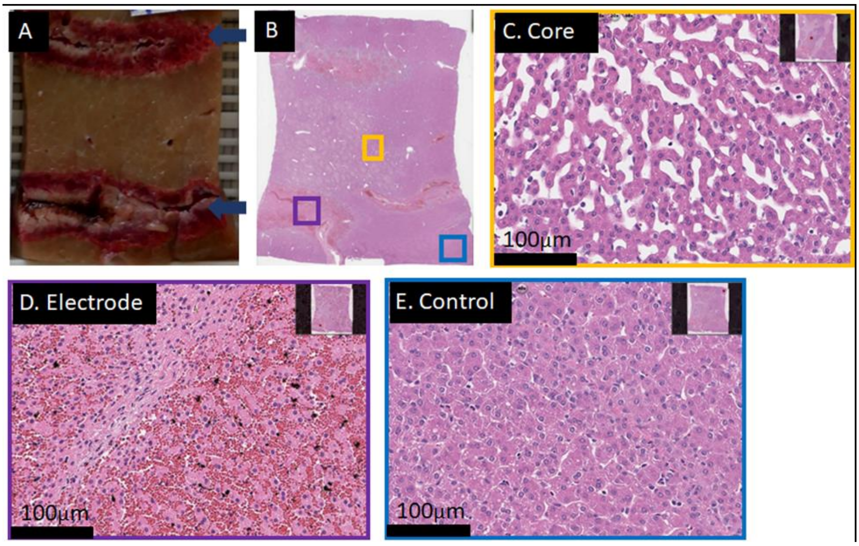

Figure 21: Example of a non-bridged 2-electrode ablation. Two pulses at 1600 V and 1500 V peak voltage were applied, delivered with 13G diameter electrodes at 20 mm distance and 30 mm exposure length. Total time required was approximately 5s, however the waveforms were cut off early by the software, leading to incomplete discharge and hence incomplete delivery and distribution of electrolysis. Liver harvest was 22h post treatment. **A:** Macroscopic image of the lesion, which shows healthy looking tissue between the electrodes (electrode track is visible as deeply darkened tissue, direction is indicated in dark blue arrows). **B:** H&E staining of the entire lesion. **C:** H&E stained tissue sample at 20x magnification from the core region (yellow insert in B). Sinusoids and cells appear affected, but not dead. **D:** H&E stained tissue shows complete cell death and disrupted cellular infrastructure at the electrodes at 20x magnification (purple insert in B). **E:** H&E stained control area at 20x magnification, blue insert in B.

4.4.3 E2 ablation with non-parallel electrodes

The application of two electrodes, in which the electrodes are not parallel and at one point come very close to each other, was tested in another experiment. The test was performed to see if E2 treatment can be successfully performed in cases where electrodes are not strictly parallel. Typically, in IRE procedures such an application will cause rapid discharge and resulting shut-down of the device. The results of the experiment are shown in Figure 22. A complete ablation of the area between the active parts of the electrodes and beyond was achieved. Microscopical results at different relevant sites (Figure 22C-E) compared to control (Figure 22B) show that the anticipated lesion was fully ablated throughout the space between the electrodes. A gradient of cell death can be seen, starting from the convergence (left in Fig 22A) of severe thermal necrosis to complete hepatocellular necrosis to severe apoptosis at the most diverged parts (Figure 22C). In the areas of thermal necrosis, the vessels were damaged, as to be expected (Figure 22D-E). No discharge (ignited plasma formation) was noted during pulse application.

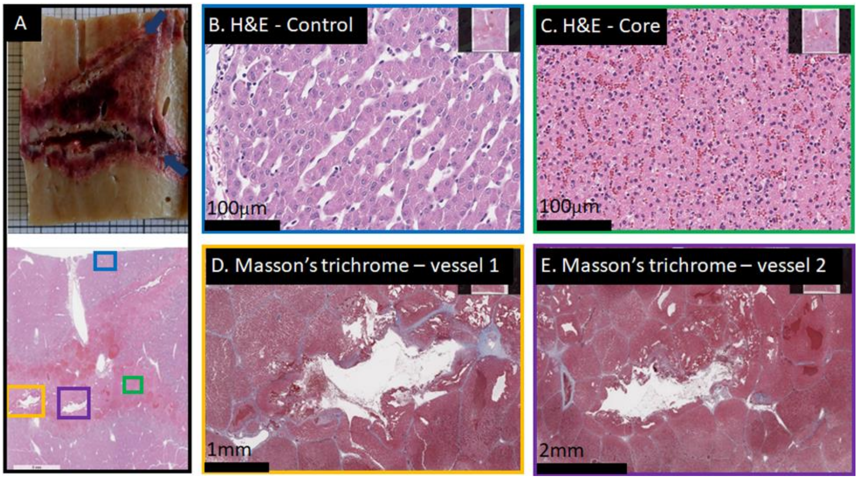

Figure 22: A 2-electrode lesion with non-parallel free-hand insertion. The parameters were 1000 V and 1200 V peak waveform voltage respectively, using 13G diameter electrodes with 30 mm exposed length at 293 µF capacitance. The distance between the electrodes was estimated using ultrasound measurement. Liver harvest was 22h post treatment. **A:** Gross macroscopic image of the lesion (top) and H&E stained slide of the whole lesion (bottom). Dark blue arrows indicate direction of electrode

track. **B:** H&E stained control area at 20x magnification (blue insert in A). **C:** H&E stained tissue sample at 20x magnification from the core region (green insert in A), showing complete cell death throughout the area. **D:** Masson’s trichrome staining of a vessel which was enclosed in the treatment area (yellow insert in A). Thermal necrosis is apparent, which the vessel was severely affected by. **E:** Masson’s trichrome staining of another vessel which was close to where the electrode tips almost touched (purple insert in A). Thermal necrosis has affected the vessel infrastructure.

4.4.4 E2 ablation with a bipolar electrode

Figure 23 and 24 show results for the application of a prototype bipolar electrode. Figure 23 shows an example of a closed ablation field between the two electrodes. In this experiment, three pulses at voltages of 1200, 1100 and 1000 V, and at 293 µF were delivered in a total of 9 seconds. In the experiment shown in Figure 24, the same pulse protocol was applied, but only 193 µF was delivered. In addition, the insulated distance of anode and cathode was larger with 15 mm instead of 10 mm (Table 6), resulting in a non-continuous lesion.

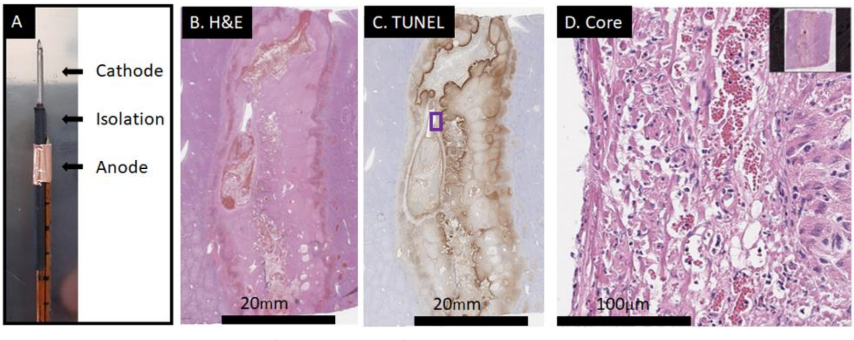

Figure 23: Example of a successful ablation with a bipolar electrode. Applied were three E2 waveforms at 1200, 1100 and 1000 V peak voltage and 293 µF capacitance. Liver harvest was 18h post treatment. **A:** The electrode prototype had lengths of 10-10-15 mm for anode-isolation-cathode, respectively. **B:** H&E staining of the entire lesion. **C:** TUNEL-

staining of the entire lesion. Both stains show a clean, closed lesion with a mixture of necrosis and significant apoptosis towards the margins.

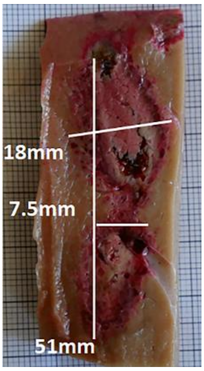

Figure 24: Non-continuous lesion of a bipolar electrode. 15-15-15 mm were used as anode-isolation-cathode lengths, respectively, employing 3 times 1200 V peak voltage for the waveforms and 193 µF charge.

4.5 Discussion

The treatment of large tumors which are close to sensitive structures and cannot be completely removed by surgery or radiation therapy remains a challenge for clinicians. Focal therapies which are based on extreme thermal changes, such as microwave ablation, radiofrequency ablation or cryoablation are able to achieve respectable lesion sizes, but they face the issue of potential thermal damage, which makes them unemployable near sensitive structures, similar to standard treatments. Currently available electroporation-based therapies have preservative properties towards vessels and nerves and can thus be used in such a clinical setting, but they face limitations regarding treatment size, as the distance between two electrodes is limited. Thus, a tissue-preserving form of therapy which can create large lesions in close proximity to sensitive structures is in demand. This study investigated the application of E2 in such a clinical setting.

Results in Figure 16, 19 and 23 illustrate the ability of E2 to produce large lesions, and the safety of the application when large and critical vessels are within the treatment field. To achieve these lesions, two and four-electrode arrays as well as a bipolar electrode were successfully utilized.

Figure 16 and 17 illustrate successful four-electrode array applications which can safely create large lesions, while including critical vessels in the treatment field. While both lesions were produced following an identical treatment protocol, the application shown in Figure 16 employed electrodes with a larger diameter (16G). The displayed clinical results in Figure 17 have slightly smaller outer dimensions. This is most likely due to the fact that approx. 20% less total charge was delivered into the same tissue volume.

The charge dependency of the E2 treatment effect can also be observed in the partial ablation shown in Figure 18. Both the maximal field as well as the total charge (per volume tissue) were lower than in the cases presented in Figure 14 and 15. This likely resulted in too little electrolytic species per tissue volume and electric fields which were too low for reliable reversible electroporation throughout the treatment field. The latter point is indicated through the macroscopically visible “hourglass” shape, which is typical for electrical field-based procedures with insufficient electroporation parameters. A similar conclusion was made in a study on Electrochemical treatment, where it was shown that Coulomb dosage is proportional to the extension of the tissue damaged by pH [148].

The achieved lesion sizes are clinically significant. Comparable IRE treatments of pig liver to those shown here were performed and are described in [16]. In their experimental setting, four electrodes were arranged in a 15 mm square, with an exposure of 10 mm, in which a total of 8 pulses of 100 µs duration and 2500 V were delivered to successfully ablate tissue between all electrodes. In comparison, the results in Figs 16 and 17 were obtained with 1400 V and 10 pulses. As the applied voltage in E2 is much lower than in IRE, it is possible to scale up the treated volume of tissue. The increase of the exposure length to 30 mm or longer is possible. With today’s recommendations for clinical IRE, an IRE treatment that achieves the same result would need an application of 540 pulses at 2250 V.

The results in Figure 19 and 20 show that it is possible to obtain complete ablation with two electrodes with the delivery of only two pulses at field strengths equal to what is used in clinical ECT protocols. In contrast, a similar procedure with IRE would require 2500 V and 180 pulses with a delivery time of approx. 220 seconds, not including the time for manual push-forward procedure due to the limited maximum exposure length in IRE application.

Similar to the four-electrode array, the incomplete ablation of a two-electrode array shown in Figure 21 was possibly due to 30% less charge being delivered to the tissue, further confirming that Coulomb dosage is a relevant factor to consider in an E2 application. The parameters which resulted in the lesion shown in

Figure 19 can be seen as a lower E2 margin for two-electrode arrays.

Focal therapy is often employed when the target tissue is difficult to reach in a surgical setting. But it is also in such cases where anatomical limitations may hinder the insertion of perfectly parallel needle-type electrodes. This is one of the limitations of IRE, because pulses delivered between two electrodes that are not parallel may result in inhomogeneous electric fields within the treatment field and possibly impair treatment outcome. The successful and safe application of ablation with non-parallel electrodes is therefore something that is desired in a clinical setting. An example of such a successful case is shown in Figure 22. A geometry like this is not possible with IRE pulses because the required electric field magnitude allows little wiggle-room, resulting in gaping plasma formations between converging electrodes [20]. An ignited plasma spreads due to its very low resistance. If not shut down immediately, immense energies can be delivered into the tissue in microseconds. As E2 is further below this plasma ignition threshold, convergence of electrodes is less of a problem. However, as to be expected, joule heating remains more prevalent in these high-field areas. Therefore, the mode of death in this area shifted more towards thermal-induced cell death.

To overcome the challenges which arise with multiple electrodes, such as non-parallelism, the application of bipolar electrodes can be another feasible option. Figure 23 and 24 show the results of the use of a prototype bipolar electrode. The parameters applied in Figure 23 resulted in complete ablation, while the ablation procedure with significantly less charge did not produce a continuous lesion (Figure 24). It is evident that much less electrolysis was delivered in the incomplete ablation.

4.6 Conclusion

This *in vivo* study was performed in porcine liver to evaluate E2 applications to achieve large lesions. The goal of the study was to develop a better understanding of the effects of E2 parameters on tissue ablation with the boundary conditions of fast, large and vessel-preserving ablations, employing various electrode arrays that are commonly used in clinical settings. The results demonstrate the ability to produce large continuous lesions with a 4-electrode array, a 2-electrode array and a bipolar electrode encompassing large vessels in a majority of the treatment zones. Lesions as large as 35 x 35 x 35 mm were achieved without requiring replacement of the electrodes. No major bleeding occurred, no clinically significant adverse events occurred and no subject died during treatment or observation time. Similar to other electroporation-based treatments, parameters that are below the effective threshold will lead to non-continuous lesions. It is implied that an E2 application is charge-dependent, which needs to be considered when defining lower thresholds of treatment parameters in a clinical setting. The charge dependency of the treatment was also observed in the *in vitro* study described in Chapter 3, thus both studies show congruent results in that regard. The next Chapter will further investigate the lower limits of E2 in an *in silico* study, and aim to understand the underlying cell death mechanisms which take place in order to reliably predict E2 lesion sizes.

An *in silico* study on the treatment effects of E2

Chapter 5

5.1 Abstract

To investigate the electrochemical effects of an E2 application, an *in silico* study was performed. The goal of the study was to simulate ion concentration profiles and the resulting pH fronts of known and theoretical E2 applications *in vitro* and *in vivo*. A buffered model which incorporates components of a bicarbonate buffer system and a protein buffer system was employed. The results were combined with an assessment on electroporation efficiency, ion uptake and resealing processes to determine how the interplay between the electrolysis and electroporation component of E2 leads to cell death. It was shown that the extracellular concentrations of protons and hydroxyl ions are high enough that, when combined with electropermeabilization of the cell, molecules can enter the cells in lethal bulge concentrations. Moreover, it was shown that high concentrations of iron and chlorine ions are present. The results further reinforce the hypothesis that E2's cell killing mechanism is triggered internally after the uptake of high concentrations of different molecules within the treatment field. The findings of this study are in alignment with the *in vitro* study presented in Chapter 3, which showed that the E2 effect unfolds after a significant time delay and that both components are necessary. The findings are also in alignment with previously reported *in vivo* results which determined the cell death modi of E2 to be necroptosis and pyroptosis.

5.2 Introduction

In Electrochemical Treatment, a small dc current is applied to tissue, activating the electron transfer and polarizing the electrodes, which results in the formation of ions at the surface of the electrodes, according to Eq. (6) – (8) (Chapter 2). In addition, negatively charged ions move towards the anode and positively charged ions towards the cathode, forming a significant pH gradient within the treatment field, which is ultimately the cause of cell death [113]. The resulting electric field also drags Na^+ and Cl^- towards anode and cathode, respectively. Once there, these ions start to react with other molecules, producing more chemical substances, such as sodium hydroxide at the cathode, and hydrochloric acid, oxygen and chlorine at the anode [46].

Seminal work on *in silico* modeling of electrochemical treatment was performed by Nilsson *et al.* in a series of papers [42, 114–116] and is discussed in detail in Chapter 2. Their model, while simple, gave insight into ion movements within the treatment field and the resulting pH fronts, which was shown to correlate with areas of cell death obtained from *in vivo* and *in vitro* data.

The resulting pH changes in electrochemical treatment face the natural buffering capacity of tissue. Homeostasis, the regulation of the dynamic stability of the internal medium and thus the cell, is influenced by physiological processes such as respiration, blood circulation, and renal excretion. To maintain homeostasis, the body’s buffering system is essential. Bicarbonate, proteins and organic phosphate are the principal buffer systems, being mainly present in plasma and interstitial fluid. This buffering system is a critical part for numerical modeling of EChT, as demonstrated in [43] and [124], and electroporation-based treatments like GET, as demonstrated in [149], and provides more accurate results than using an electrolyte without buffering capacity.

The electrochemical processes during an E2 application and the impact they have on tissue have not been investigated yet. The purpose of this study was to investigate the electrochemical effects of E2 and combine the outcomes with an assessment of electroporation processes which simultaneously take place. The goal was to combine the results of both aspects to further understand the cell death mechanism of an E2 treatment.

5.3 Methods

When looking at the electrolysis component of E2, the generation, movement and concentration profiles of ionic species are considered, using the modeling approach of [116, 124] and adopting it to simulate an E2 application. When looking at the electroporation component, the electroporation efficiency related to pulse number application and molecule uptake are considered by using the model suggested in [150].

5.3.1 Physiochemical background

As indicated in the introduction of this Chapter, the dominent electrochemical reactions at the electrode surfaces are the oxygen and chlorine evolution reactions at the anode (Table 7, reaction number 1 and 2), and the hydrogen evolution reaction at the cathode (Table 7, reaction number 3). Pre-clinical and theoretical studies have implied that the reaction products around the electrodes, specifically the H^+ and OH^- ions, are the main cause of tumor ablation, as extreme pH values are reached during an electrochemical treatment [151, 152]. Other studies report that the toxicity of chlorine ions and other complexes involving chlorine are one of the main drivers of tissue necrosis due to electrolysis [42]. The impact of both of these aspects is currently unknown for E2 application.

The spreading of ions is counteracted by the buffer systems that exist inside the tissue. The most important buffer system in tissue is the bicarbonate buffer system, followed by buffer systems including proteins and organic phosphate contents, which together make up the entire buffer capacity of tissue [42, 116]. The electrochemical reactions of electrolytic products within buffer systems like tissue are very complex and have been described previously [116, 149, 153]. The model described here considers these buffering aspects of the tissue. Table 7 summarizes the reactions which are included in this model.

Table 7: Reaction descriptions, equations and rates for the reactions considered in the buffered model [124].

Reaction no. and description	**Reaction equation**	**Reaction rate**
1. Oxygen evolution	$2H_2O \rightarrow O_2 + 4H+ + 4e^-$	i1 (Eq. 26)
2. Chlorine evolution	$2Cl^- \rightarrow Cl_2 + 2e^-$	i2 (Eq. 27)
3. Hydrogen evolution	$2H_2O + e2^- \rightarrow H_2 + 2OH^-$	i3 (Eq. 28)
4. Hypochlorous acid formation	$Cl_{2aq}+H_2O \rightarrow HClO + H^+ + Cl^-$	$R_{Cl2(aq)} = -R_{HClO} = -R_{H+} = -R_{Cl}- =$ $-k4,f([Cl_{2aq}]-\frac{[HClO][H+][Cl-]}{K4})$
5. Chlorinating reaction of Cl_2	$Cl_{2aq}+Org \rightarrow Org\text{-}Cl + Cl^- + H^+$	$R_{Cl2(aq)} = R_{Org} = -k6,f[Cl_2][Org]$
6. Chlorinating reaction of HClO	$HClO + Org \rightarrow Org\text{-}Cl + H_2O$	$R_{HClO} = R_{Org} = -k7,f[HClO][Org]$
7. Oxidation reaction of Cl_2	$Cl_{2aq} + Org\text{-}red + H_2O \rightarrow Org\text{-}ox + 2Cl^- + 2H^+$	$R_{Cl2(aq)} = R_{Org\text{-}red} = -k8,f[Cl_{2aq}][Org]$
8. Oxidation reaction of HClO	$OH^- + HCO_3^- \rightarrow CO_3^{2-} + H_2O$	$R_{HClO} = R_{Org\text{-}red} = -k9,f[HClO][Org\text{-}red]$
9. Bicarbonate buffer reaction	$OH^- + CO_2 \rightarrow HCO_3^-$	$R_{OH-} = R_{CO2} = -\ R_{HCO3}{}^- = -k2,f([CO_{2aq}][OH^-] - \frac{[HCO3-]}{K2})$
10. Bicarbonate buffer reaction	$OH^- + HCO_3^- \rightarrow CO_3^{2-} + H_2O$	$R_{OH-} = R_{HCO3}{}^- = R_{CO3}{}^{2-} = -k3,f([HCO_3^-][OH^-]-\frac{[CO32-]}{K2})$
11. Bicarbonate buffer reaction	$H^+ + HCO_3^- \rightarrow CO_{2aq} + H_2O$	$R_{HCO3-} = R_{H+} = -R_{CO2aq} = -k11,f([H^+][HCO_3^-]-\frac{[CO2][H2O]}{K11})$
12. Organic buffer reaction	$H\text{-}Org + OH^- \rightarrow Org^- + H_2O$	$R_{H\text{-}Org} = -k5,f[H\text{-}Org][OH^-] + k5,f[H\text{-}Org]^0[OH^-]^0$
13. Organic buffer reaction	$OH\text{-}Org + H^+ \rightarrow Org^+ + H_2O$	$R_{OH\text{-}Org} = R_{H+} = R_{Cl-} = -korg([H^+][OH\text{-}Org][Cl^-] - [H^+]^0[OH\text{-}Org]^0[Cl^-]^0$
14. Organic buffer reaction	$Org^+ + Cl^- \rightarrow Org\text{-}Cl$	$R_{OH\text{-}Org} = R_{H+} = R_{Cl-} = -korg([H^+][OH\text{-}Org][Cl^-] - [H^+]^0[OH\text{-}Org]^0[Cl^-]^0$
15. Organic buffer reaction	$OH\text{-}Org + H^+ + C^{l-} \rightarrow Org\text{-}Cl + H_2O$	$R_{OH\text{-}Org} = R_{H+} = R_{Cl-} = -korg([H^+][OH\text{-}Org][Cl^-] - [H^+]^0[OH\text{-}Org]^0[Cl^-]^0$
16. Equilibrium reaction $Cl_2(aq)$	$Cl_{2aq} \rightarrow Cl_{2gas}$	$r_{Cl2aq} = -k10,f([Cl_{2aq}]-c^s{}_{Cl2})$
17. Water protolysis reaction	$H^+ + OH^- \rightarrow H_2O$	$r_{H+} = r_{OH-} = k12,f([H^+]+[OH^-]-\frac{[H2O]}{KW}$

In addition to the evolution of H^+, Cl^- and OH^-, the three main reactions of a bicarbonate buffer system were included, as well as amphoteric reactions of the organic compounds. The latter is important to incorporate because the organic compounds react as an acid near the cathode and as a base near the anode electrode (Table 7, reaction (14) and (15)) [124]. Reactions that are not being considered within the described system are the dissociation of hypochlorous acid and the reaction forming gaseous carbon dioxide from aquarious carbon dioxide.

5.3.2 Geometry description and problem statement

A series of simulation studies were conducted using different geometries for the electrodes and the electrolyte.

An initial study was conducted in which the modeling results were compared to actual experiments. This served as a validation for the electrochemical model. In this first study, the model geometry is identical to the experimental set-up described in Chapter 5.3.5 and Table 3 Exp ID 2 (Chapter 3): Two plate electrodes with a depth of 5 mm were positioned 8 mm apart in a petri dish filled with gelified medium. Figure 25 provides a schematic of the geometrical dimensions and computational domain. The electrolyte domain is confined by the inner electrode surfaces. The outer boundary represents two lines which connect the bottom and top of the electrode tips.

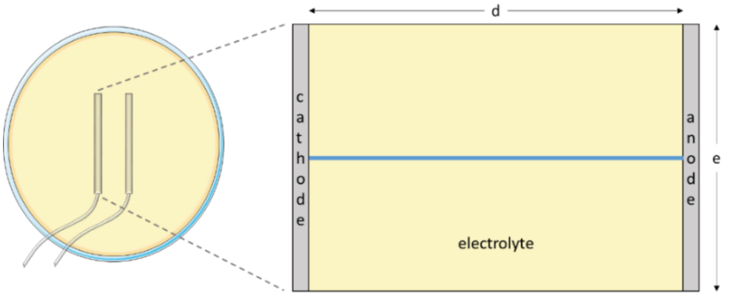

Figure 25: Model geometry of Mo-ID 1. Blue line represents the defined cutline.

This first study investigated the effect of an E2 application in two types of electrolytes: The first electrolyte only consists of saline solution (Table 8) and represents an unbuffered electrolyte. The second electrolyte has buffering properties and considers the bicarbonate buffer capacity of the extracellular fluid of the tissue as well as the reaction of chlorine with reactive organic molecules. It is further enhanced to include the influence of the buffer capacity of the proteins, as described in [124].

The physical parameters of the different models are listed in Table 8.

Table 8: Physical parameters used in the models. Mo-ID = Model ID. Mo-ID 1: *in vitro* in gelified medium (Figure 25); Mo-ID 2: *in vitro* cells in solution (Figure 26); Mo-ID 3: *in vivo* liver electrode + pad (Figure 27).

Mo-ID	Description	Parameter	Value
1	Electrode exposure (height)	e1	5 mm
1	Electrode thickness	di1	0.5 mm
1	Distance between electrodes	d1	8 mm
1	Initial temperature	T1	310.15 K
1	Initial conductivity	σ1	1.3 S/m
2	Electrode exposure (height)	e2	4 mm
2	Electrode thickness	di2	1 mm
2	Distance between electrodes	d2	4 mm
2	Initial temperature	T2	293.15 K
2	Initial conductivity	σ2	1.7 S/m
3	Electrode exposure (height)	E4	20 mm
3	Electrode thickness	di4	1 mm
3	Distance between electrode/pad	d4	20 mm
3	Initial temperature	T4	310.15 K
3	Initial conductivity	σ4	0.184 S/m

Comparison studies of E2 application with different pulse numbers were carried out to investigate the effect of different buffer systems and applied current densities on generation of electrolysis species, ion movements and concentration profiles inside the tissue. Previous considerations of pH changes during E2 only considered saline solution without a buffer [50]. To directly compare these results to that of what is closer to reality (tissue as a buffered system) was a secondary aim of this study.

In a second study, the geometry of the *in vitro* study with cells in solution (Chapter 3, Table 3 Exp ID 1) is applied to be able to directly compare results of the *in silico* study with those described in Chapter 3. Figure 26 illustrates the geometry of that model.

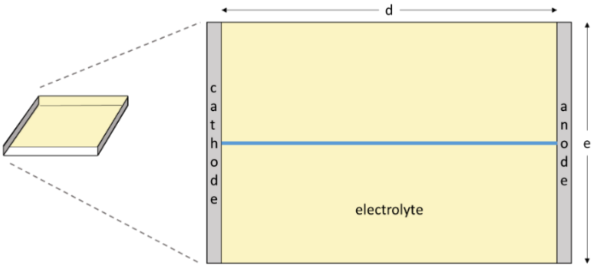

Figure 26: Model geometry of Mo-ID 2. Blue line represents the defined cutline.

In a third study, the hypothetical geometry of a monopolar electrode paired with a surface pad is considered. Figure 27 illustrates the geometry of that model, which is implemented as a simple 2D model with a 1D axial symmetry. The purpose of this type of geometry is to approximate the solution for $\mathbf{J_i}$ in a way that it can produce realistic results while reducing computation times. When the pad is far enough from the electrode, the simulated current densities around the electrode can be considered a close enough approximation to the actual case of a single needle electrode and a pad, if we approximate the relation between the flux and the E-field as $\mathbf{J_i} = \sigma\mathbf{E}$.

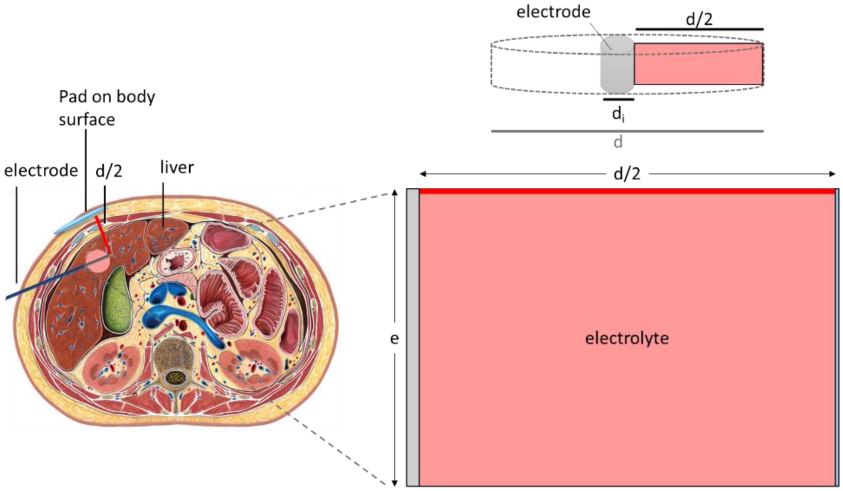

Figure 27: Model geometry of Mo-ID 3. Red line represents the defined cutline. Axial body image adapted from [154].

For the *in vitro* study of cells in solution, the simulation period and endpoint was 120 seconds. The reason for that is because the cells remained in the solution for this time period before being diluted in medium. It thus represents how the experiments were executed in reality. For the *in vivo* study, the same simulation period and measuring point was chosen. The two minutes represent approx. the time in which the perfusion inside the tissue is strongly impaired after a pulse of 800 V/cm magnitude [155]. This phenomenon, known as the vascular lock, is dose-dependent regarding pulse duration and amplitude, and will decline over time, though the impairment can last for several hours [156]. The assumption applied in this simulation is that during the time of maximum perfusion stop, the generated electrolysis products remain in the area within the extracellular space (with the exception of gaseous molecules).

Table 9: Treatment parameters used in the models. Mo-ID = Model ID. Mo-ID 1: *in vitro* in gelified medium; Mo-ID 2: *in vitro* cells in solution. Mo-ID 3: *in vivo* liver. t_{treat} = treatment time, t_m = time of measuring. *only for buffered simulation.

Mo-ID	Description	Parameter(s)	Value
1	E2 Initial voltage	U0	640 V
1	E2 tau time	$\tau1$	2.66 ms
1	E2 applied pulse numbers	P	1,2*,5, 10
1	E2 frequency of pulse application	f1	0.5 Hz
1	E2 time of measuring	t_m1	10s after treat
2	E2 Initial voltage	U_01	320 V
2	E2 tau time	$\tau2$	2.84 ms
2	E2 applied pulse numbers	P	3
2	E2 frequency of pulse application	f2	0.33 Hz
2	E2 time of measuring	t_m2	120s after treat
3	E2 Initial voltage	U_02	1500 V
3	E2 tau time	$\tau3$	70 ms
3	E2 applied pulse numbers	P	1
3	E2 time of measuring	t_m3	120s after treat

5.3.3 Modeling and numerical procedure

The extended buffered model includes a total of 15 unknowns: fourteen ionic species that were considered in this study:

Na^+, H^+, Cl^-, OH^-, Cl_2, HClO, Org (organic compounds near the anode), HCO_3^-, CO_2, CO_3^{2-}, Org-red, OH-Org, H-Org, Orgc (organic compounds near the cathode), and the potential field. Thus, fifteen domain equations with associated boundary conditions are required to model this system. The simplified model uses saline solution, thus only the ionic species Na^+, H^+, Cl^-, OH^-, Cl_2 and CO_2 are considered.

5.3.3.1 Governing equations

To simulate ion movement, only diffusion and migration mechanisms were used. These can be described with the Nernst-Planck equation:

$$N_i = -D_i \nabla c_i - \frac{zi}{|z_i|} u_i c_i \nabla \varphi_i \tag{20}$$

With c_i as concentration, D_i as diffusion coefficient, z_i as the electrical charge of the ion and u_i as the ionic mobility of the ionic species. The mass conservation for the species is considered, which is given by substituting equation (20) in (21):

$$\frac{\partial c_i}{\partial t} + \nabla \cdot N_i = R_i \tag{21}$$

The reaction rate for the corresponding species, R_i can be described as

$$\frac{\partial c_i}{\partial t} = D_i \nabla^2 c_i + \frac{zi}{|z_i|} u_i \nabla \cdot (c_i \nabla \varphi) + R_i \tag{22}$$

and the current density is given by

$$j = F \sum_{i=1}^{14} z_i N_i \tag{23}$$

As charge separation in electrolytes is within the Debye length scale [157], the Poisson equation which relates the electric field and charge separation for electrolytes simplifies to the electroneutrality condition. From substituting the Nernst-Planck expressions for N_i, the combination of the laws of conservation of mass and charge satisfy the conservation of current.

5.3.3.2 Initial and boundary conditions

The mass transport across the electrode surfaces for the species which are involved in the electrode reactions is related to the charge transport of electrochemical reactions [42, 116], while the mass transport is zero for species not involved in the electrode reaction. Therefore, the mass transport can be described as

$$-D_i(\nabla c_i \cdot n) - \frac{zi}{|z_i|} u_i c_i (\nabla \phi \cdot n) = 0 \text{ for i = Na}^{+}\text{, CO}_2\text{, CO}_3^{2-}\text{, HCO}_3^{-} \quad (24)$$

The contribution of the gas reactions of oxygen, chlorine, and hydrogen to the total current density are given by Butler-Volmer equations:

$$i_i = i_0 \left\{ C_R P_R \exp\left(\frac{\alpha_a F \eta}{RT}\right) - C_0 P_0 \exp\left(\frac{\alpha_c F \eta}{RT}\right) \right\} \quad (25)$$

where the gaseous reactants $Ci=ci/ci_{ref}$ and $Pi=pi/pi_{ref}$ are the reduction and oxidized forms of the species involved in the electrochemical reactions according to [124], and where the values for ci_{ref} were chosen to be the initial concentrations of the species, except in the case of Cl_2, where the value was set to its saturation concentration at 1 atm.

The evolution of H^+, Cl^- and OH^- can thus be described as

$$i_1 = i_{0,1} \left\{ \exp\left(\frac{F\phi_S - \phi_1 - E_{Eq1}^{ref}}{2RT}\right) \ldots - \left(p_{O2} \frac{1}{4} [H^+] \exp\left(\frac{F\phi_S - \phi_1 - E_{Eq1}^{ref}}{2RT}\right) \right\} \quad (26)$$

$$i_2 = i_{0,2} \left\{ [Cl^-] \exp\left(\frac{F\phi_S - \phi_1 - E_{Eq2}^{ref}}{2RT}\right) \ldots - \left([Cl_{2aq}] \frac{1}{2} [H^+] \exp\left(\frac{F\phi_S - \phi_1 - E_{Eq2}^{ref}}{2RT}\right) \right\} \quad (27)$$

$$i_3 = i_{0,3} \left\{ [OH^-]^2 p_{H2} \exp\left(\frac{3F\phi_S - \phi_1 - E_{Eq3}^{ref}}{2RT}\right) \ldots - \left(\exp\left(\frac{F\phi_S - \phi_1 - E_{Eq3}^{ref}}{2RT}\right) \right\} \quad (28)$$

Zero concentration gradients were applied at the outer boundary layer, and the system starts with no concentration gradients throughout the electrolyte domain. For the simulations, initial ionic concentrations close to the actual values found in plasma and interstitial fluid were used (Table 10).

Table 10: Initial concentrations used in the model.

Description	**Parameter**	**Value**	**Ref.**
Initial concentration of Na^+	c_0^{Na+}	0.160 M	[158]
Initial concentration of H^+	c_0^{H+}	$1 \cdot 10^{-7.4}$ M	[158]
Initial concentration of Cl^-	c_0^{Cl-}	0.133 M	[124]
Initial concentration of OH^-	c_0^{OH-}	$1 \cdot 10^{-6.2}$ M	[124]
Initial concentration of HCO_3^-	c_0^{HCO3-}	0.027 M	[158]
Initial concentration of $Cl_{2(aq)}$	$c_0^{Cl2(aq)}$	0.000 M	[158]
Initial concentration of HClO	c_0^{HClO}	0.000 M	[158]
Initial concentration of Org	c_0^{Org}	0.280 M	[158]
Initial concentration of Org-red	$c_0^{Org\text{-}red}$	0.280 M	[158]
Initial concentration of H_Org	$c_0^{H\text{-}Org}$	0.050 M	[158]
Initial concentration of $CO_{2(aq)}$	$c_0^{CO2(aq)}$	$1 \cdot 10^{-3}$ M	[158]
Initial concentration of CO_3^{2-}	$c_0^{CO_3^{2-}}$	$4.4 \cdot 10^{-5}$ M	[158]
Initial concentration of Org^-	c_0^{Org-}	0.000 M	[158]
Initial concentration of OH-Org	$c_0^{OH\text{-}Org}$	0.050 M	[158]
Saturation concentration of $Cl_{2(aq)}$	$c^s_{Cl2(aq)}$	0.040 M	[158]

5.3.3.3 Physiochemical properties

The initial concentrations, thermodynamic and kinetic parameters applied in the study are listed in Table 10 and 11. A temperature of 37°C was considered as the reference temperature for Mo-ID 1 and 3, while 20°C was considered as reference temperature for Mo-ID 2. The following relationship was used to calculate the diffusion coefficients at 37°C and 20°C from 25°C [32]:

$$\frac{D_{20}\mu_{20}}{T_{20}} = \frac{D_{25}\mu_{25}}{T_{25}} = \frac{D_{37}\mu_{37}}{T_{37}} \tag{29}$$

in which viscosities at the different temperatures are approximated to be µ20°C = 1 mNm^2, µ25°C = 0.890 mNm^2 and µ37°C = 0.692 mNm^2 [159]. All organic compounds (Org, Orgred, OH-Org, Orgc and H-Org) are immobile in this model, with diffusion coefficients close to zero [124].

The solubility of chlorine in tissue was estimated according to [124] by Henry's law:

$$k10, f = \exp\{\frac{[Cl_{2aq}] - c^s_{Cl2aq}}{ac^s_{Cl2aq}}\} \tag{30}$$

With constant a = 0.001 and c^s_{Cl2aq} as chlorine saturation solubility.

Table 11: Thermodynamic and kinetic parameters of the model for 37°C.

Description	**Parameter**	**Value**	**Ref.**
Diffusion coefficient of Na^+	D_{Na+}	$1.78\cdot10^{-9}\,m^2s^{-1}$	[157]
Diffusion coefficient of H^+	D_{H+}	$12.5\cdot10^{-9}\,m^2s^{-1}$	[157]
Diffusion coefficient of Cl^-	D_{Cl-}	$2.72\cdot10^{-9}\,m^2s^{-1}$	[157]
Diffusion coefficient of OH^-	D_{OH-}	$7.05\cdot10^{-9}\,m^2s^{-1}$	[157]
Diffusion coefficient of HCO_3^-	D_{HCO3-}	$1.49\cdot10^{-9}\,m^2s^{-1}$	[157]
Diffusion coefficient of $Cl_{2(aq)}$	$D_{Cl2(aq)}$	$1.98\cdot10^{-9}\,m^2s^{-1}$	[157]
Diffusion coefficient of HClO	D_{HClO}	$2.06\cdot10^{-9}\,m^2s^{-1}$	[157]
Diffusion coefficient of Org	D_{Org}	$1\cdot10^{-12}\,m^2s^{-1}$	[124]
Diffusion coefficient of Org-red	$D_{Org\text{-}red}$	$1\cdot10^{-12}\,m^2s^{-1}$	[124]
Diffusion coefficient of H_Org	$D_{H\text{-}Org}$	$1\cdot10^{-12}\,m^2s^{-11}$	[124]
Diffusion coefficient of $CO_{2(aq)}$	D_{CO2}	$2.71\cdot10^{-9}\,m^2s^{-1}$	[157]
Diffusion coefficient of CO_3^{2-}	D_{CO3}^{2-}	$2.46\cdot10^{-9}\,m^2s^{-1}$	[157]
Diffusion coefficient of Org^-	D_{Org-}	$1\cdot10^{-12}\,m^2s^{-1}$	[124]
Diffusion coefficient of OH-Org	$D_{OH\text{-}Org}$	$1\cdot10^{-12}\,m^2s^{-11}$	[124]
Exchange Current density of reaction A1	i0,1	$1\cdot10^{-6}\,Am^{-2}$	[160]
Exchange Current density of reaction A2	i0,2	$10\,Am^{-2}$	[161]
Exchange Current density of reaction C	i0,3	$1\,Am^{-2}$	[161]
Equilibrium potential difference reaction A1	$E_{eq}1$	0.77 V	[157]
Equilibrium potential difference reaction A2	$E_{eq}2$	1.41 V	[157]
Equilibrium potential difference reaction C	$E_{eq}3$	-0.828 V	[157]
Equilibrium constant	K_2	$3.3\cdot10^{7}\,M^{-1}$	[162]
Forward rate const, buffer system reaction	$k_{2,f}$	$20\,M^{-1}s^{-1}$	[162]
Backward rate const, buffer system reaction	$k_{2,b}$	k_{2f}/K_2	[124]
Equilibrium constant	K_3	$2.6\cdot10^{3}\,M^{-1}$	[162]
Forward rate const, buffer system reaction	$k_{3,f}$	$15\,M^{-1}s^{-1}$	[162]
Backward rate const, buffer system reaction	$k_{3,b}$	k_{3f}/K_3	[124]
Equilibrium constant	K_4	$6.3\cdot10^{-4}\,M^{2}$	[163]
Forward rate constant of chlorine reaction	$k_{4,f}$	$37\,s^{-1}$	[163]
Backward rate constant of chlorine reaction	$k_{4,b}$	k_{4f}/K_4	[124]
Forward rate constant	$k_{6,7,8,9,f}$	$1\cdot10^{11}\,M^{-1}s^{-1}$	[124]
Rate constant of Cl_2 conversion to gas phase	$k_{10,f}$	Eq. 30	[124]
Forward rate constant	$k_{11,f}$	$3.1\cdot10^{11}\,M^{-1}s^{-1}$	[42]
Forward rate constant of water deionization	$k_{12,f}$	$1.5\cdot10^{11}\,M^{-1}s^{-1}$	[42]
Backward rate constant of water deionization	$k_{12,b}$	$KW*k_{12f}/c_{H2O}$	[124]
Forward rate constant of reaction	$k_{w,f}$	$1.5\cdot10^{11}\,M^{-1}s^{-1}$	[114]
Backward rate constant of reaction	$k_{w,b}$	$2.7\cdot10^{-5}\,s^{-1}$	[114]
Water protolysis rate constant	KW	$1\cdot10^{-13.6}\,M^{2}$	[114]

5.3.3.4 Numerical solution

The system of equations was solved using the COMSOL Multiphysics software (www.comsol.com, V 5.3a), a finite-element based software.

Similar to [124], the concentrations, electrolyte, and electric potential were discretized using linear shape functions for each element. Free triangular elements with a maximum size of 0.1 mm were used to discretize the electrolyte domain for Mo-ID 1 and 2, while free quad elements with a maximum size of 1.19 mm were used for Mo-ID 3. The interface tertiary current distribution, Nernst-Planck (tcdee) was used for ionic species transport, pH profiles, and electric fields. Supporting electrolyte was selected as the charge conservation model in all simulations. Crosswind diffusion and streamline diffusion methods were selected for stabilization in all simulations. The reactions node was used to enter reaction rates for each ion. The default boundary conditions for flux and insulation were used. Additionally, the electrodes needed to be defined further. For the inner surface of the anode, electric potential with an external electric potential of zero volts was selected as the electrode surface boundary condition. The two electrode reactions at the anode were then added as electrode surface reactions. The concentration-depended kinetics via the Butler-Volmer equations were selected. For the cathode, the boundary condition was set to electrode potential, and in the reaction node under electrode kinetics, the local current density needed to be defined. In this case, the E2 exponential decay function, which was introduced as a global analytic function, was multiplied with the value to have a time-dependent decay of the applied current.

The consecutive pulses were simulated in study steps, where the first step had a simulation period from 0 to the time point of the next pulse. The next step then started with the next pulse application and ended before the next pulse. The time period of the final study step was extended to the endpoint of the simulation.

The post-processing procedure consisted of presenting the data along a straight 1D cutline between the two electrodes (Mo-ID 1 and 2, Figure 25 and 26), or the electrode and pad (Mo-ID 3, Figure 27).

5.3.4 Considerations of electroporation efficiency, ion uptake and resealing processes

In order to understand the treatment effect of E2 in more detail, it is necessary to evaluate the electroporation efficiency, ion uptake and re-sealing processes of the cell membranes. The following chapters describe the rationale and considerations which were taken into account to include these aspects into the assessment of this *in silico* study.

5.3.4.1 Electroporation efficiency

There are different methods to theoretically assess electroporation efficiency. Some numerical models calculate the efficiency based on the determination of pore formation, number and size of pores, and pore lifetimes. All of these highly depend on pulse and tissue parameters, which are the inputs of these models.

Another way to determine electroporation efficiency is by assessing the conductivity change of the electrolyte during pulse application. The conductivity is linked to the cell membrane permeabilization efficiency in a way that it will increase when the membrane permeabilization of the cell membranes inside the electrolyte increases. The membrane conductivity model in [164] had the goal to test this hypothesis and reproduce the conductivity changes which occur during the first microseconds after the pulse onset, by linking the changes in membrane conductivity to the induced transmembrane voltage (TMV):

$$\sigma_m = \sigma_{m0} + K(e^{\beta|TMV|} - 1) \tag{31}$$

with σ_{m0} as the conductivity of the membrane at the resting TMV and K and β as two constants adjusted to fit empirical results.

Under the assumption that the membrane conductivity increases due to the creation of pores, Eq. 31 can be written as:

$$\overline{\sigma_m} = \sigma_{m0} + \sigma_p(\lambda e^{\beta|TMV|} - 1) \tag{32}$$

With λ as a third constant and σ_p as the with medium filled pore conductivity.

According to the Eqs. 31 and 231, the average membrane conductivity is related to the cell membrane area which is occupied by membrane defects. Because σ_{m0} and σ_p are constant along the membrane, and the term $\lambda e^{\beta|TMV|} - 1$ represents the local area occupied by pores at each point of the membrane, the average membrane conductivity can be put in relation to the relative pore area (RPA) during the pulse [150]:

$$\overline{\sigma_m} = \sigma_{m0} + \sigma_p \times RPA \tag{33}$$

The effective conductivity of the pores was estimated as in [165]:

$$\sigma_p = \frac{\sigma_e - \sigma_i}{\ln(\sigma_e/\sigma_i)} \tag{34}$$

with σ_e and σ_i being the conductivity of the extracellular and the intracellular medium.

It has been suggested that different types of pores can be created upon electroporation. Transient pores will form in high quantities and have a lifetime of only ~100 ns [166]. A typical large transient pore number during cell electroporation pulsing is of order 10^6 and is mainly responsible for the measured conductivity change. Because transient pores vanish so shortly after the pulse ends, they cannot account for evident post-pulse processes like large and/or non-specific ionic and molecular transport. The transport of molecules into cells is thus proposed to be via complex and long-lived pores, which are typically larger in size and have a longer lifetime [166]. The determination of the fraction of these long-lived pores is necessary to calculate cellular uptake.

Pavlin and Miklavčič [167] developed a model in which they considered the increase of electroporation efficiency with an increased number of applied pulses. They calculated the fraction of long-lived pores for different applied pulse numbers (Table 12), showing approx. a linear dependency within the measured range. While the applied field strengths of that study match those of an E2 application (around 800 V/cm), the applied pulse duration of 100 µs is significantly shorter than that of an E2 application, which typically lasts between tens of milliseconds (*in vitro*) and several hundred milliseconds (liver tissue).

Previous studies have predicted that at E-field amplitudes within the discussed range, submicrosecond long pulses induce a large number (millions per cell) of small pores ($r \sim 1$ nm), whereas longer pulses result in a much smaller number (up to tens of thousands per cell) of larger pores (tens of nanometers) [168]. Other studies have also confirmed that the application of ms-long pulses will create larger, more stable pores [169]. Thus, the values for the fraction of long-lived pores in Table 12 can be considered as a worst case approximation in terms of electroporation efficiency of an E2 application and can be used when the objective is to find the lower threshold of sufficient membrane permeability and ion uptake.

Table 12: Comparison of different parameters with increasing number of pulses: Measured transient conductivity changes $\Delta\sigma_{tran}/\sigma_0$ during N-th pulse, changes of the initial level of conductivity due to ion efflux $\Delta\sigma/\sigma_0$ (after N pulses), permeability coefficient k_N, the fraction of transient short-lived pores (f_p), fraction of long-lived pores (f_{per}) and percentage of permeabilized cells. All parameters were evaluated at E~0.86 kV/cm. Table adapted from [167].

No. of pulses	**N = 1**	**N = 2**	**N = 4**	**N = 8**
$\boldsymbol{\Delta\sigma_{tran}/\sigma_0}$	0.15	0.14	0.14	0.145
$\boldsymbol{\Delta\sigma/\sigma_0}$	0.083	0.2	0.4	0.59
k_N [s^{-1}] 8·100µs	0.029	0.040	0.072	0.11
f_p [·10-5]	~3	~3	~3	~3
f_{per} [·10-6]	~1.4	~1.9	~3.4	~5.4
permeabilization	10 – 14%	-	33%	75 – 90%

5.3.4.2 Ion uptake

Mercadal *et al.* [150] further developed the outlined model to describe molecular transport across the cell membrane. Because the majority of the transport process happens after the pulse, the contribution of electrophoretic and diffusion transport during the pulse can be neglected. Hence, the transport by diffusion after the pulse is considered, which can be described by Fick's law:

$$\frac{dc(t)}{dt}\frac{V}{S_p(t)} = -D\frac{dc(t)}{dx} \qquad (35)$$

with c(t) as the concentration of the ion which passes through an effective and time-dependent surface area $S_p(t)$, V as the volume of the cell and D as the diffusion coefficient of the ion.

As discussed previously, only the long-lived pores are to be considered here, because the uptake through the short-lived pores can be neglected. To tie the effective surface area to the fraction of long-lived pores, the following function was applied [150]:

$$S_p(t) = S_{per} e^{-t/\tau} \tag{36}$$

with S_{per} as the surface area occupied by the membrane defects at the end of the pulse, and τ as the resealing time constant. The relationship of S_{per} to the RPA (Eq. 33) and fraction of pores (f_{per}) was defined as

$$S_{per} = f_{per} \times S_p = RPA \times S_c \tag{37}$$

with S_c as the surface of the cell membrane.

The amount of molecules which pass through the membrane via diffusion is a time and concentration-dependent function described by Eq. 35. Under the assumption that the extracellular concentration of the molecule can be considered constant and a simplification of the term dc(t)/dx as $(c_i(t)-c_e(t))/h$ (c_i = intracellular concentration; c_e = extracellular concentration; h = membrane thickness) can be applied, Eq. 35 can be simplified to

$$c_i(t) = (c_{i0} - c_e) \exp\left[\frac{DS_{per}\tau}{Vh} \mathrm{e}^{-\frac{t}{\tau}} - 1\right] + c_e \tag{38}$$

Equation 38 can be further simplified in the case of concentration measurement at a time point long after pulse delivery completion [150], which is the case in this study:

$$c_i = (c_{i0} - c_e) \exp\left[-\frac{DS_{per}\tau}{Vh}\right] + c_e \tag{39}$$

5.3.4.3 Resealing of pores

While the electroporation efficiency is dependent on the applied electric field strength and other pulse parameters, it is known that resealing is independent of the field strength [170].

Hence, in this model we only considered the effects of resealing as a simple function of time without an initial E-field dependency. The exponential function is added to the function defining the effective surface area (Eq. 36).

For the multi-pulse application, some aspects need to be considered. When the duration of the applied pulse is less than 1 ms, the resealing lifetime is a linear function of the number of successive pulses [171]. This is the case as long as less than 10 pulses are delivered [171].

In the case of the application of an E2 pulse such an approximation is a worst case approximation. In fact, it was proposed by Teissie that increasing the pulse duration brings an increase in the density of defects (pore creations) and an associated increase in transport. This increase is thought to be further enhanced during the resealing process, because the created defects remain present during a longer time compared to effects of shorter pulses. It is also speculated that long pulses result in a higher cumulative transport of molecules across the membrane [172].

The effect of interpulse delays on electroporation effiency and resealing processes is something that is not being considered in this assessment, though some studies suggest that it plays a role in the electropermeabilization efficiency. Interpulse delays of longer than one second can have a so called memory effect, a process which is not fully understand yet [171].

In this assessment, the resealing time was empirically determined for the specific case of an *in vitro* application of E2 of cells in solution (Mo-ID 2 Table 8), specifically by taking into account the time-dependent measured permeabilization efficiency (Chapter 3, Figure 9). Table 13 lists all parameters employed in this assessment.

Table 13: Parameters used in this investigation.

Description	**Parameter**	**Value**	**Ref.**
Diffusion coefficient, H^+ (20°C)	D_{H+}	$9.15 \cdot 10^{-9}$ m^2s^{-1}	[157]
Diffusion coefficient, OH^- (20°C)	D_{HO-}	$5.16 \cdot 10^{-9}$ m^2s^{-1}	[157]
Diffusion coefficient, Cl^- (20°C)	D_{Cl-}	$1.99 \cdot 10^{-9}$ m^2s^{-1}	[157]
Diffusion coefficient, Fe^{2+} (20°C)	D_{Fe2+}	$6.51 \cdot 10^{-10}$ m^2s^{-1}	[157]
Cell membrane thickness	h	$5 \cdot 10^{-9}$ m	[150]
Resealing time	τ	936s	calculated
Volume of cell	V	$1.8 \cdot 10^{-15}$ m^3	calculated
Total surface of cell membrane	S_c	$7.1 \cdot 10^{-10}$ m^2	calculated
Intracellular conductivity	σ_i	0.5 S/m	[150]
Extracellular conductivity	σ_e	1.7 S/m	measured
Pore conductivity	σ_p	Eq. 34	calculated
Membrane conductivity	σ_m	Eq. 32	calculated
Membrane conductivity at resting TMV for h = 5 nm	σ_{m0}	$2.7 \cdot 10^{-7}$ S/m	[150]
Constant	K	$5 \cdot 10^{-9}$ m x σ_p	[164]
Constant	β	16	[150]
Applied potential, to produce E field 800 V/cm	V0	0.9V	[150]
Relative pore area	RPA	Eq. 37	calculated
fraction of long-lived pores 1-10P	f_{per}	$1.4 \cdot 10^{-6}$ - $6 \cdot 10^{-6}$	[167]

5.3.5 *In* vitro experiments

5.3.5.1 Experimental set-up

To validate the implemented electrolysis component of the model, pH fronts were determined experimentally. The experimental set-up used in this study was identical to that described in Table 8 (Exp ID 1), employing custom-made electrodes made of polished stainless steel (0.5 mm thickness) at a distance of 8 mm and a surface area of 30 x 5 mm² (width x length; Figure 7).
For the E2 application, the electrodes were connected to the output ports of a custom-built generator, a device which was previously used and described in detail [56].

The experiments were carried out in two different media. The first medium consisted of a simple NaCl solution which was gelified with agar (7.5 g/L). The second medium was a bicarbonate buffer with added sodium chloride, also gelified with agar of the same concentration. All concentrations were identical to the model parameters listed in Table 10. The pH was set to 7.4. The medium was brought to boiling and then poured into petri-dishes. Immediately after pouring, an indicator was added, which is further described in Chapter 5.3.4.3. The gel was cooled down to 37°C and was then ready for treatment. During the treatment phase, the petri-dishes were kept warm at 37°C for consistent initial temperature.

5.3.5.2 Treatment protocols

Prior to treatment, the temperature of the gelified medium was controlled to ensure a temperature of 37°C. An E2 treatment with varying pulse numbers was applied. The treatment parameters are listed in Table 8 under Model ID 1. All treatments were repeated 3 times for each indicator dye.

5.3.5.3 Colorimetric measurements

Colorimetric detection of pH changes: Universal indicator (JBL) was used to visualize the pH in the gelified medium after treatment. A universal indicator consists of water, 1-Propanol, phenolphthalein sodium salt, sodium hydroxide, methyl red, bromothymol blue monosodium salt and thymol blue monosodium salt [173]. The indicated colors are shown in Table 14, while an example of the application is shown in Figure 28A.

Table 14: Colorimetric detection of pH in these experiments.

pH range	Description	Colour
< 4.5	Acid	Red
5–6	Weak acid	Orange or yellow
7	Neutral	Green
8–11	Weak alkali	Blue-purple

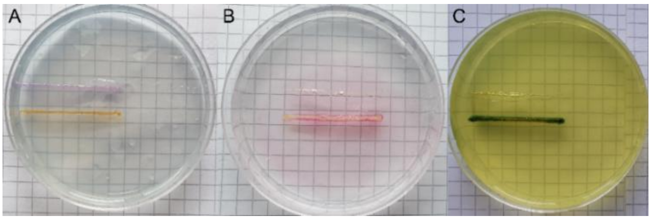

Figure 28: Examples of gelified medium with indicator after E2 treatment. Pictures were taken 10s after treatment completion. **A:** pH indicator **B:** DPD indicator **C:** potassium hexacyanoferrate(III).

Colorimetric detection of chlorine ions: The presence of free chlorine in the form of hypochloric acid (HClO) and hypochlorite (OCl) was detected by adding a total of 6 drops of N,N Diethyl-1,4-phenylendiamin (DPD) indicator solution (ipt) into the agar before it hardened. In the absence of iodide ion, free chlorine reacts instantly with DPD indicator to produce a red color. The discoloration of the sample liquid results from the oxidation of the indicator by the HClO [174]. The indicator solution has a sensitivity of 0.1 ppm. An example of the colorimetric detection is shown in Figure 28B.

Colorimetric detection of iron ions: The presence of Fe^{2+} ions was detected by mixing potassium hexacyanoferrate(III) (5% w/V) into the gel before it hardened. The potassium hexacyanoferrate(III) turns blue in the presence of Fe^{2+}, which is generated in the oxidation reaction at the anode:

$$Fe(s) \rightarrow Fe^{2+} + 2e^{-} \qquad (40)$$

An example of the colorimetric detection is shown in Figure 28C. The detection limit was 0.0136 mol/L.

5.4 Results

5.4.1 Model verification and validation

The model was validated by comparing the results to experimental data. The accuracy of the equations, electrochemical reactions, homogeneous reaction kinetics, and all input parameters were varified for each electrode separately in previous studies [56, 124].

In this study, first the outputs of the NaCl and buffered model were compared to the the measured pH profiles and ion concentrations from the *in vitro* experiments with model ID Mo-ID 1. Table 15 shows the modelled and measured values, while Chapter 5.4.2 graphically presents the results. Then, the buffered model was used to compare the simulated values to some of the results of the *in vitro* study described in Chapter 3, and *in vivo* studies described in [56].

As can be seen in Table 15 and Figure 29, the model outcome is overall in alignment with the experimentally obtained results. All simulated values are within the standard deviation of the experimental data, except in one case (distances obtained for 1 pulse in NaCl).

Table 15: Simulated lesion zone distances (mm) and pH values near the anode and cathode using the NaCl and buffered model along with experimentally measured mean pH front distances and pH. EXP = experimental; SIM = simulated; An = Anode; Cat = Cathode; SD = standard deviation. Threshold pH at cathode: pH 9; threshold pH at anode: pH 4.5 except for E2 in buffered medium 1 - 5 pulses, here the threshold is pH 6 because pH 4.5 was not reached.

E2 treatment in NaCl						
#no of pulses	EXP d(pH) and SD at An	SIM d(pH) at An	SIM pH at An	EXP d(pH) and SD at Cat	SIM d(pH) at Cat	SIM pH at Cat
1	0.63±0.38	1.50	3.70	0.70±0.24	1.06	11.56
5	2.07±0.25	1.95	3.69	1.87±0.43	1.71	12.16
10	2.42±0.23	2.39	3.16	2.36±0.13	2.31	12.32
E2 treatment in buffered medium						
#no of pulses	EXP d(pH) at An	SIM d(pH) at An	SIM pH at An	EXP d(pH) at Cat	SIM d(pH) at Cat	SIM pH at Cat
1	0.60±0.24	0.45	6	0.70±0.24	0.51	9.10
2	0.62±0.17	0.60	6	0.94±0.29	0.63	9.60
5	0.84±0.11	0.74	6	1.19±0.08	0.93	11.15
10	0.93±0.07	0.86	4.5	1.44±0.17	1.28	11.89

5.4.2 Simplified vs. buffered model

Figure 29 compares simulated and experimentally determined pH fronts of lethal limits for E2 treatment delivered in gelified buffer and NaCl. All measurements were performed at 10s after the last pulse was delivered. The results in buffered media (Figure 29A and B) are very similar between simulated and experimentally obtained data, and the two lines show no statistical significance (p = 0.125). The results in saline solution (Figure 29C and D) are also not significantly different, but the simulated results appear to be slightly underestimating the actual pH fronts.

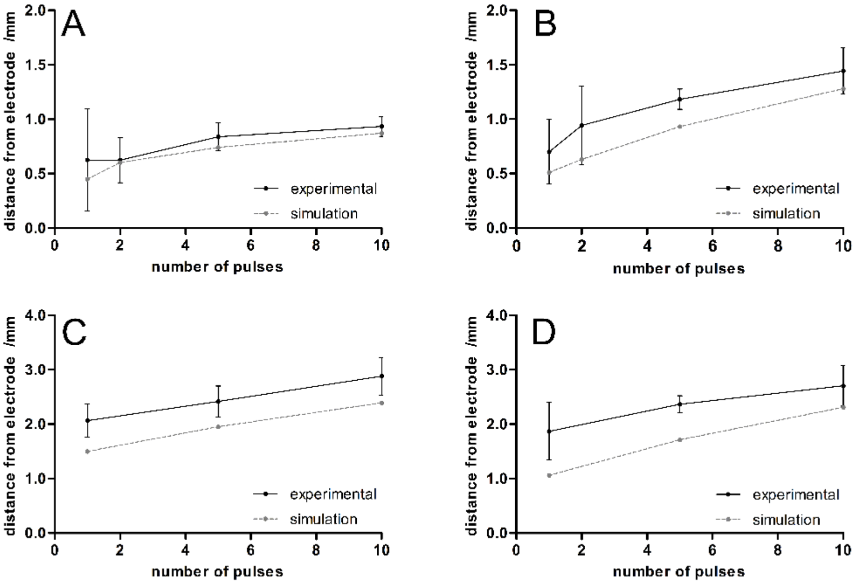

Figure 29: Experimental and simulated pH fronts after E2 treatment of different pulse numbers. **A:** buffered media, anode, threshold pH value is pH 6. **B:** buffered media, cathode, threshold pH value is pH 9. C: NaCl, anode, threshold pH value is 4.5. D: NaCl, cathode, threshold pH value is pH 9.

The E2 treatment in buffered media did not result in a pH of 4.5 or lower when 1 to 5 pulses were applied. This result was congruent in both experimental and simulated data. The application of 10 pulses resulted in a minimum pH of around 4.5. Similar low pH values were reached at the anode when the treatment was in saline solution, even at lower pulse numbers.

As expected, the pH fronts travel further towards the other electrode with increasing pulse number. Also expected is the fact that the lethal pH fronts (pH < 4.5 and > 9) in the saline solution travel much further than in the buffered solution.

5.4.3 Ion concentrations for different E2 applications

5.4.3.1 *in vitro* application of E2

The buffered model was employed to simulate ion concentrations for the *in vitro* treatment discussed in detail in Chapter 3. The parameters are listed in Table 8 under Model-ID 2. The cells in solution were treated with three exponential decay pulses and kept in the cuvette for 2 minutes before further dilution in medium. Figure 30 shows the concentration profiles throughout the cuvette at different time points, where the ventral line at x = 0 mm is the location of the cathode and x = 4 mm the location of the anode. The blue line corresponds to 15 seconds, green to 30, red to 60 and cyan to 120 seconds after pulse application, respectively.

Figure 30A shows proton concentrations, where there is a clear increase in $[H^+]$ at the anode which slowly decreases towards the cathode and with time. Figure 30B shows hydroxyl concentrations, which behave exactly the opposite, which is expected. It should be noted that the H^+ ions travel further away from the electrode surface than the OH^- ions. Figure 30C shows a decrease of Cl^- at the cathode side, and increase at the anode side. Sodium concentration profiles are illustrated in Figure 30D, where concentrations are increased towards the cathode and decreased towards the anode. Finally, the last row shows carbonite (Figure 30E) bicarbonate concentrations (Figure 30F). Both are strongly elevated around the cathode, which makes sense because both are products of the bicarbonate buffer reaction with OH^-. At the anode, both carbonate and bicarbonate concentrations are elevated as well, though less strongly. Both panels indicate that the buffer reactions are taking place.

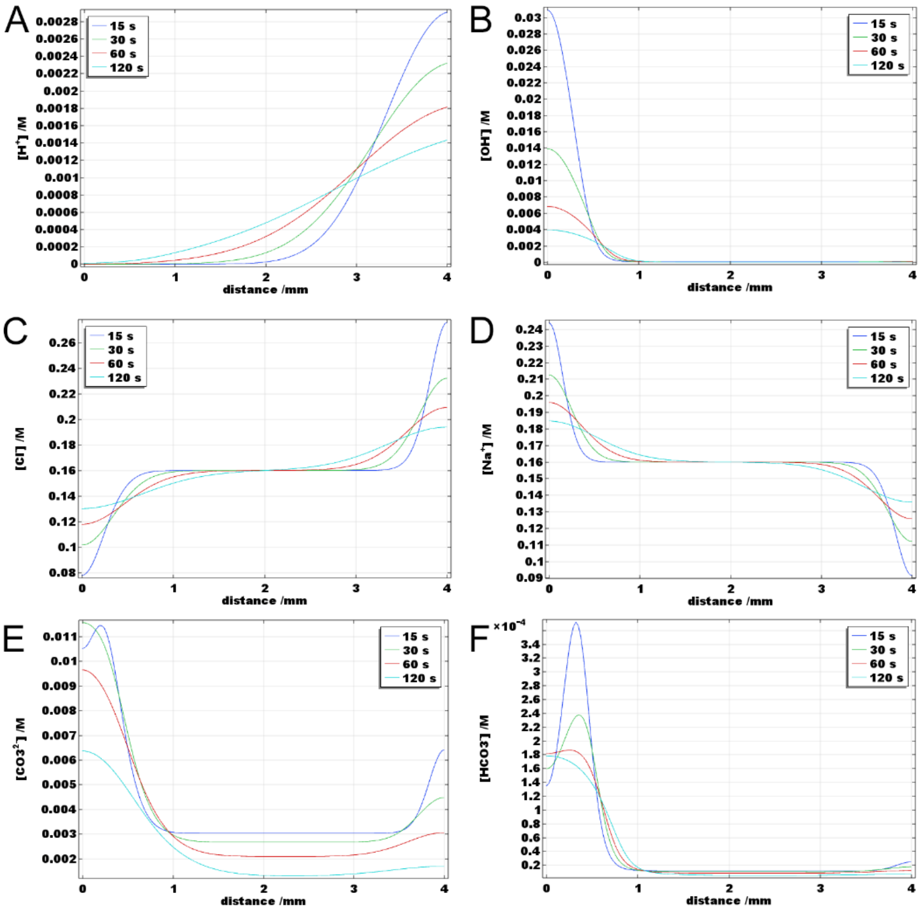

Figure 30: Simulated concentration profiles between the electrodes after E2 treatment with three pulses using the buffered model. View is a cut plane between cathode (x = 0 mm) and anode (x = 4 mm) halfway the electrode length (meaning that the line goes right in the middle of the treatment area). Time points after treatment: blue, 15 seconds; green, 30 seconds; red, 60 seconds, cyan, 120 seconds. **A:** Proton concentrations **B:** Hydroxyl concentrations **C:** Chlorine concentrations **D:** Sodium concentrations **E:** Carbonite concentrations **F:** Bicarbonate concentrations.

Figure 31 shows time-dependent simulated hypochloric acid concentrations directly after the last pulse of a 1, 2, 5 and 10 pulse application in buffered medium. HClO forms at the anode as described in reaction 4 (Table 7). All curves have their peak around 50 – 60 ms after the last pulse, with peak values of 0.824 mM (1P) to 0.71 mM (10P). The peak values decrease with number of pulse application. In all treatments, the concentration of HClO decreases rather rapidly, reaching 0 before the first second passes. It should be noted that these concentrations are all within a 2 – 3 mm space around the anode (not pictured) and are not present further away from the electrode surface.

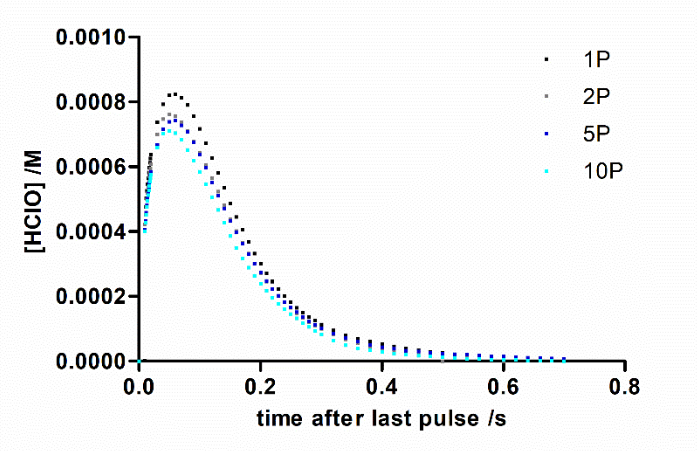

Figure 31: Time-dependent peak hypochloric acid concentrations of 1, 2, 5 and 10 pulses applied in buffered medium.

5.4.3.2 *in vivo* application of E2

Next, the buffered model was employed to simulate a hypothetical E2 treatment in liver with a monopolar electrode and surface pad (geometry in Figure 27). For this configuation, the distance between pad and electrode was assumed to be 6 cm. Figure 32 shows the simulated pH values at different time points for two cases: Anode as electrode (Figure 32A) and cathode as electrode (Figure 32B). Minimum pH reached for anode as the electrode was approx. pH 3, while at the cathode, the maximum pH reached was approx. pH 9. A lethal area was drawn (red dotted line), the thresholds of which will be explained in more detail in the next chapter.

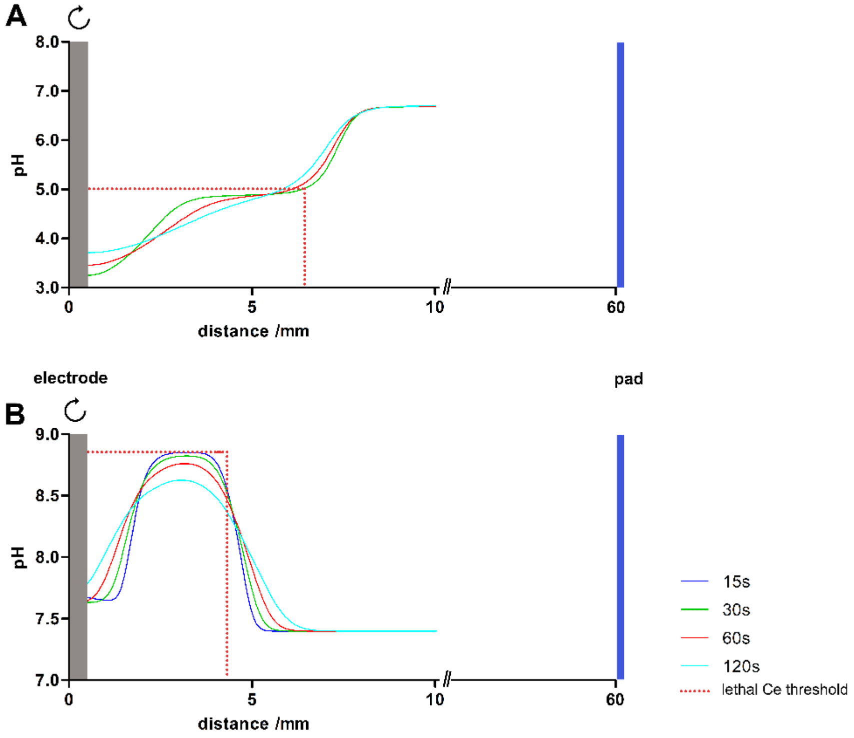

Figure 32: pH fronts at the electrode after the application of a single exponential decay pulse employing a monopolar electrode and surface pad. Pad is located at a distance of 60 mm. The blue line corresponds to 15 seconds, green to 30, red to 60 and cyan to 120 seconds after pulse application. Red dotted line indicates lethal extracellular concentration thresholds (Ce) of H^+ (A) or OH^- (B). **A:** Anode as electrode. **B:** Cathode as electrode.

5.4.4 Intracellular ion concentrations after E2 application

Figure 33A shows the estimated shape of the exponential decay which was obtained from *in vitro* data presented in Chapter 3 and used to calculate the resealing process of the formed long-lived pores. Figure 33B shows the calculated total surface of the cell membrane which is occupied by long-lived pores after 1-10 consecutively applied pulses.

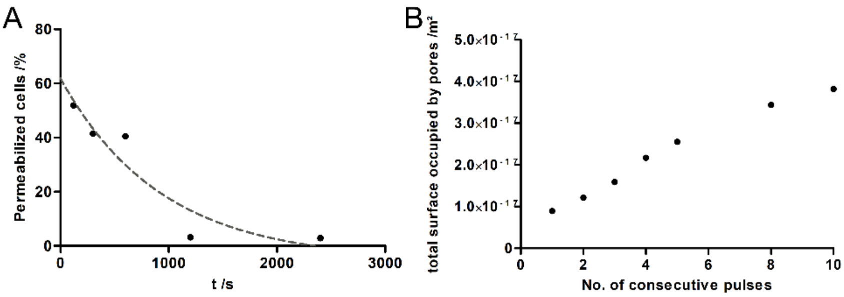

Figure 33: A: Percent of permeabilized cells as a function of time. Numbers were obtained from *in vitro* measurements (Figure 9). **B:** Calculated total surface of the cell membrane which is occupied by long-lived pores after 1-10 consecutively applied pulses.

The obtained ion concentrations of H^+ and OH^- at 120s which are presented in Figure 30 were used to calculate the intracellular concentration at the lower limit which is potentially able to trigger intrinsic cell death processes (described in detail in Chapter 2.4 and Table 1). This was an E2 application of 3 pulses, the measuring times are t = 3s after the first pulse, t = 6s after the second pulse, and t = 120s after the final pulse. The lower limits for lethal intracellular concentrations were taken from various scientific publications which have studied cell death through increased intracellular concentrations and are listed in Table 16.

Table 17 summarizes the results of the calculations, listing the lethal limit (and measuring point) of the extracellular concentration C_e, the resulting calculated C_i values by using Eq. 39, and finally the distances from the electrode surface at which these C_e limits are present according to the simulations. Note that the lethal extracellular limit was set a lot more conservatively, with necessary concentrations one order of magnitude higher than those listed in Table 16.

A substantial area within the cuvette is exposed to ion concentrations which can potentially lead to regulated cell death. As expected, the necessary extracellular concentrations that lead to enough uptake to intrinsically trigger cell death decrease with applied pulse numbers. Thus, the area in which cells are exposed to lethal C_e gets bigger with increasing pulse number. In fact, the entire cuvette has external concentrations of ions after one pulse which, when able to pass the cell membrane, can achieve lethal intracellular bulk concentrations. It should be noted that in reality, pH fronts are formed (refer to Figure 35). Figure 34 illustrates calculated internalized H^+ and OH^- ions per pulse application and is a visualization of the data presented in Table 17.

Table 16: Intracellular concentration thresholds for different ions that lead to cell death induction (H^+, OH^-, Fe^{2+}) or cell function impairment (Cl^-).

Ion	**Threshold**	**Ref**
H^+	10^{-6} M	[60]
OH^-	10^{-6} M	[175]
Cl^-	0.05 M	[68]
Fe^{2+}	$6 \cdot 10^{-6}$ M	[176]

Table 17: Extracellular concentrations (C_e) which were used as a threshold and which lead to potentially lethal intracellular concentrations (C_i) for different number of pulses (#P) applied in the *in vitro* cuvette experiment, and the resulting simulated distances (d) at which these concentrations are reached, when no pH front formation is considered. Note that the lethal thresholds for H^+ and OH^- were set one order of magnitude higher than those found in the literature (Table 16).

#P	**C_e /M**		**C_e /mM**		**C_i /M**		**d /mm**	
	H^+	OH^-	H^+	OH^-	H^+	OH^-	H^+	OH^-
1	$1.01 \cdot 10^{-5}$	$1.01 \cdot 10^{-5}$	0.01010	0.01010	$1.01 \cdot 10^{-5}$	$1 \cdot 10^{-5}$	0.9	4
2	$1.01 \cdot 10^{-5}$	$1.01 \cdot 10^{-5}$	0.01005	0.01005	$1.01 \cdot 10^{-5}$	$1 \cdot 10^{-5}$	1.38	4
3	$1.00 \cdot 10^{-5}$	$1.00 \cdot 10^{-5}$	0.01001	0.01001	$1.00 \cdot 10^{-5}$	$1 \cdot 10^{-5}$	4	4

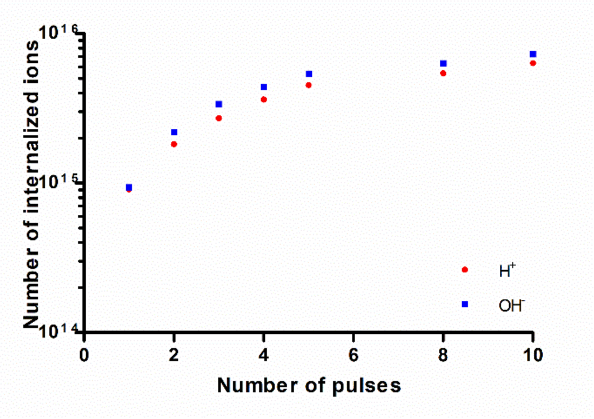

Figure 34: calculated internalized H^+ and OH^- ions for 1-10 executive pulse applications.

Iron distributions of a certain concentration were obtained from the *in vitro* experiments in gelified medium 10s after pulse application. This data was used because it was the only experimentally obtained source of information available for Fe^{2+} release and distribution after an E2 application. Table 18 shows the results for different pulse numbers. It should be noted that the detection limit here is 0.0136 M. This is much higher than the calculated lethal C_e of $6\cdot10^{-6}$ M (see Table 16). The table also includes the values for Cl^-, which are all above the reported threshold for induction of cell function impairment throughout the treatment field, as well as throughout the cuvette (not pictured).

Table 18: Distances of extracellular concentrations (C_e) of Fe^{2+} (*detection limit) and Cl^- and the resulting intracellular concentrations (C_i) for different number of pulses (#P).

#P	**C_e /M**		**C_i /M**		**d /mm**	
	Cl^-	Fe^{2+}	Cl^-	Fe^{2+}	Cl^-	Fe^{2+}
1	0.0592	0.0136*	0.05	0.00599	8	0.37 ± 0.11
2	0.0500	0.0136*	0.05	0.00741	8	0.39 ± 0.12
5	0.0499	0.0136*	0.05	0.01054	8	0.66 ± 0.10
10	0.0499	0.0136*	0.05	0.01247	8	0.80 ± 0.11

5.5 Discussion

The mechanistic explanation of the E2 modality is hypothetically thought to be related to the permeabilization of the cell membrane by electroporation, which makes the cells more sensitive to the products of electrolysis. These can, thereby, enter the cells in an unregulated way, causing homeostasis impairment and eventually cell death. Due to the combination with cell permeabilization, the effect can be achieved at a much lower electrolytic dosage than what is required for tissue ablation by electrolysis. The goal of this study was to test this hypothesis by combining the knowledge obtained from the *in vitro* and *in vivo* E2 applications with electrochemical simulations, as well as considerations of electropermeabilization efficiency, molecular uptake and membrane resealing.

5.5.1 Unbuffered vs. buffered model

The model was implemented for two types of media, a simple saline solution and a buffered medium which represents the ionic composition of tissue. The simulation of an E2 application in both of these models was consistent with experimental results (Figure 29). It was expected that the distribution of the charged molecules would go much further in the non-buffered medium. This outcome is of importance for future benchtop experiments which employ tissue phantoms, as it shows very clearly that the results will be significantly overestimated compared to results in tissue when a tissue phantom without a buffer component is used.

5.5.2 Parallels and differences between E2 and EChT

The simulations provided concentration profiles for different relevant species (Figure 30 and 31). Even though a single exponential pulse is very short in duration compared to the dc current applied for minutes to hours in EChT, the total current density applied is high enough to produce substantial amounts of electrolysis species. Compared to reported concentrations for EChT treatments [124], the initial ion concentrations are much larger in an E2 application, which is to be expected for such high total current densities applied.

Then, these concentrations decrease to values around the same order of magnitude as in EChT after 120s, creating similar looking pH front collision points, though the maximum and minimum pH values appear to be more extreme in EChT (Figure 35).

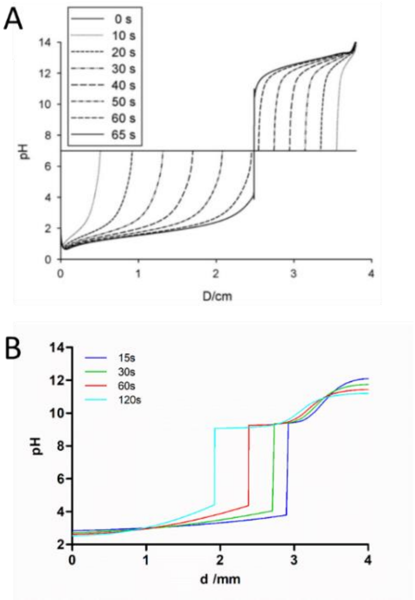

Figure 35: Time-dependent pH front collision distances. A: Electrochemical treatment of 3 mA, with the anode at x = 0 and cathode at x = 4 cm. Image taken from [123]. **B:** E2 *in vitro* application presented in this study, with 3 pulses at 800 V/cm. Distances are not in the same order of magnitude (cm (A) vs. mm (B)), therefore the graph's purpose is not direct comparison, but visualization of pH fronts for both treatments.

The key difference between the two treatment modalities is that an EChT application requires to maintain these strong pH values for minutes to hours (25min to 5h in liver [46]) in order to achieve a treatment effect, while an E2 application is completed after the pulse application (less than a minute) and does not require to maintain the extreme pH values within the treatment field.

Therefore, it is impossible to explain the mechanism of action of E2 with that of EChT, because the extreme concentrations of ionic species generated at the beginning of the E2 treatment are first in close proximity to the electrode surface and then distribute throughout the treatment area with time until they are neutralized via buffering and perfusion mechanisms once the vascular lock effect has ceased and perfusion is partially restored. Yet, the cells are evidently dead throughout the treatment field after an E2 application (though death sets in with a delay) as presented in detail in *in vivo* experiments in Chapter 4 and published in [52, 55, 56, 131, 137].

5.5.3 Proposed cell killing mechanism of E2

The question therefore remains: how do the cells in the middle of the treatment field die after an E2 application?

The presence of elevated H^+ and OH^- concentrations two minutes after treatment (Figure 30 and Table 17) is an important observation when paired with the fact that the cells have been sufficiently permeabilized (see Chapter 3, *in vitro* study). These molecules are now able to freely cross the cell membrane along a concentration gradient, a process which does not anymore depend on membrane proteins and other mechanisms which usually regulate this process. The results of this study indicate that the extracellular concentration of these molecules, while the incubation time is too short to sufficiently kill through processes in the microenvironment, would theoretically be sufficiently high to trigger intrinsic cell death once they are in the cytosol. In a later section of this chapter, this will be explained in more depth.

The results presented here indicate that the entire treatment field has extracellular concentrations of various ions which may result in lethal intracellular concentrations once they pass the cell membrane via diffusion (Table 17 and 18). As the electropermeabilization effect increases with each applied pulse, the uptake efficiency also increases with each applied pulse, at least in the range of 1 – 10 applied pulses (Figure 34). As a result, the threshold for lethal extracellular concentrations decreases, and the area of lethal extracellular concentrations increases. This pulse number-dependent behavior is in alignment with previously reported findings of other electroporation-based treatments [167, 172, 177]

The mechanism proposed would explain why cell death can occur even though the incubation time within the toxic microenvironment is so short. Usually, killing cells via the external microenvironment requires much longer exposure to the species to trigger functional decline or even cell death [60, 67].

Several *in vivo* studies [56, 130, 155, 155, 155, 178] demonstrated that cell death is delayed after E2 application, and that the cell death mode is necroptosis and pyroptosis [137]. Both of these aspects speak for intrinsically triggered cell death. Additionally, the *in vitro* study presented in this thesis also clearly showed that neither the electroporation component alone nor electrolysis component alone sufficiently killed the cells in the cuvette (Chapter 3 Figure 14). It is clear that the combination of both leads to cell death, which is in alignment with the outcomes presented in this assessment of intracellular concentrations of H^+ and OH^- after successful molecular uptake. As both of the mentioned cell death modes (necroptosis and pyroptosis) can be triggered when the cell experiences severe acidosis [59, 60] or alkaliptosis [58] on the inside, reaching concentration so high that the buffering capacity of the cell is not sufficient to counteract the bulk pH change, we assume that this is what causes the cell death.

As the concentration of electrolytically generated species are a function of the applied charge, it is no surprise that the *in vivo* study presented in Chapter 4 could clearly show for multiple applications that the treatment success is charge-dependent. All failed lesions of this study (Figure 18, 21, 24) had in common that less charge was applied than in the cases of their successful counterparts (Figure 16, 19, 23).

In addition to these findings, the general toxicity of high intracellular Cl^- and Fe^{2+} need to be taken into consideration. According to the presented simulations, both species are present in big loads both inside and outside the cell (Table 18). As explained in Chapter 2.4, multiple stressors, even if present below lethal values, can ultimately trigger intrinsic regulated cell death when combined [67]. It can be assumed that the probability of cell death increases with each of these stressors reaching elevated intracellular concentrations. Further studies with specific stains may reveal that ferroptosis is amongst the cell death modes of E2 and other electroporation-based therapies.

In general, there are more biochemical aspects that can potentially play a key role in the outcome of treatments that have an electrochemical component, such as metal release during the process and its addition to the toxicity of the extracellular space [125]. It was just explained how this study briefly touched on this by looking at Fe^{2+} distributions of E2 applications with different pulse numbers. Detected extracellular concentrations were in the tens of mM range at the dectection margin of Fe^{2+} (Table 18). Previously reported concentrations for applications of 800 V/cm of a 2 ms duration pulse (ten times shorter than the pulse applied here) were approx. 0.3 mM for the entire cuvette [179]. This means that more Fe^{2+} was detected in the experiments conducted in this study. Considering the fact that the pulse applied here was longer in duration, and in a shape which is reported to release more Fe^{2+} ions [180], the elevated levels are sensible.

As for the resulting lethal Fe^{2+} “margin”, it should be noted that the detection limit here was 0.0136 M. This is much higher than the calculated lethal C_e of $6 \cdot 10^{-6}$ M (refer to Table 16). It can therefore be assumed that the area in which Fe^{2+} reaches a C_e value resulting in lethal C_i concentrations goes further than the values reported here. The observation period (measurement after 10 seconds) was also quite short; presumably the ions will diffuse further towards the other electrode with time (refer to drift velosities presented in Chapter 3 Table 4) and will not leave the treatment field within the first two minutes [155].

While Fe^{2+} is reported to play the biggest role in metal release during electroporation with stainless steel electrodes [179], other metal ions could still play an additional role. Nevertheless, the results reported here can serve as an approximation for the lower limits of Fe^{2+} toxicity within the extracellular space.

5.5.4 Monopolar electrode configuration

In this study, the buffered model was also utilized to simulate a hypothetical clinical set-up with a monopolar electrode and a surface pad (Figure 27). The objective was to assess the resulting lethal area with just a single pulse. Applying the concentration thresholds presented in this study, the results in Figure 32 suggest that the area with lethal C_e two minutes after the treatment is approx. 5 mm around the electrode, and slightly larger in the case of the anode as the electrode. These results are encouraging and can contribute to the development of a treatment application with a monopolar electrode and pad, eventually with pulse protocols that include more than one pulse to increase the area of cell death.

5.5.5 Limitations of the study

This study has a few limitations. One of them is the fact that while the change in temperature with time and for three consecutively delivered pulses was considered for the *in vitro* study outlined in Chapter 3, it was not coupled to the electrochemical simulations of this study. Temperature increase is generally an important factor, as temperature has a substantial effect on physiological processes. Even when no significant thermal damage during the treatment occurs, an increase of temperature can have an effect on electrochemical processes such as the activity of the species H_3O^+, OH^- and H_2O due to temperature-induced pH changes [181]. The reason the temperature increase was not considered was because of computational limitations of the electrochemical simulation. In theory, it is possible to couple the Joule heating effect with electrochemical modules. This was done in [124], however only to evaluate temperature profiles, similar to those reported in Chapter 3, not to alter all thermodynamic parameters according to the simulated temperatures which in turn have an impact on the electrochemical processes. Including such processes into the model would make it very complex and significantly increase the simulation run-time.

The assessment of the electroporation part of the study was based on a very simplified model to make a few superficial assumptions on electroporation efficiency, ion uptake and resealing. While the assessment is highly approximated, almost all of the parameters which were chosen were taken from studies which employed significantly shorter pulses (i.e. 100 µs, Table 12). The exponential E2 pulse applied in the *in vitro* study had a total length of 20 ms. It is known that pulse lengths in the ms range will lead to larger and more stable long-lived pores, which will most likely significantly enhance the molecular uptake process. Therefore, it can generally be said that the parameters chosen here lie on the conversative end of the spectrum regarding long-lived pore formation. However, even with these possibly underestimating parameters, the results presented here indicate sufficient extracellular concentrations of various ions which will result in lethal intracellular concentrations. This study can therefore be seen as the basis for future, more sophisticated studies where the electroporation efficiency is modelled for a specific case study. A way to improve the model would be to include uptake mechanisms during pulse application, similar to that proposed in [177]. This addition would add the component of electrophoretic dragging of molecules into the cell during the pulse.

Another limitation is the fact that complex tissue structures and their time-dependent changes during treatment were neglected. It is known that electroosmotic effects occur when currents are applied to tissue, causing edema at the cathode and dryness at the anode [46]. Gas bubbles additionally increase pressure inside the tissue locally and induce mechanical damage [85]. Therefore, the limitation is that neither the tissue changes nor the tissue pressure change was considered. It is possible to enhance the model to include these aspects, but it will probably require tissue parameters which need to be determined experimentally first.

Finally, the geometries of the models were simple. For the validation of the treatment of cell solution in a cuvette, the model was a good approximation. The geometry which was used to simulate a monopolar + pad set-up was also a good approximation for this specific application. However, to properly simulate needle-type electrodes in tissue, it is necessary to advance the proposed 2D model to a 3D domain with a healthy outer layer. The Primary Current Distribution, Transport of the Dilute Spices, and Infinite Element Domains would need to be coupled with the additional layers, considering constant conductivity in the area of healthy tissue, to properly represent large healthy tissue around the tumor, as proposed in [124]. It is very likely that advancing the model in such a way will result in concentration profiles that are lower for *in vivo* applications.

5.6 Conclusion

This *in silico* study was performed to shed light on the electrochemical mechanism of an E2 application. A buffered model which included a bicarbonate buffer system and a protein buffer system was used to simulate ion concentration profiles and pH values. A gelified tissue phantom model with incorporated colorimetric indicators was used to validate the numerical model. Then, the *in vitro* application presented in Chapter 3 was reproduced with the model, as well as a theoretical application of E2 employing a monopolar electrode and a surface pad. The results were combined with an assessment on electroporation efficiency, ion uptake and resealing processes to determine how the interplay between the electrolysis and electroporation component of E2 can lead to cell death.

It was concluded that the extracellular concentrations of protons and hydroxyl ions may be high enough so that, when combined with electroporated cell membranes, they can enter the cells in lethal bulge concentrations and trigger the process of cell death internally. This would in alignment with the previously reported cell death modi of E2, necroptosis and pyroptosis, as both can be triggered via intrinsic pathways as a result of significant intracellular pH changes.

The findings of this study are also in alignment with the *in vitro* study presented in Chapter 3, which showed that both components are necessary for effectively eradicating tumor cells. Incubating the cells with the generated electrolysis species will not kill the cells efficiently, as incubation times are too short. The reported *in vivo* results of Chapter 4 further demonstrated a charge-dependent efficiency of E2. As the applied charge is directly correlated with the amount of produced electrolysis species, this supports a concentration-dependency of electrolysis species of the E2 treatment effect.

In summary, it can be said that the model was useful in the determination of electrochemical processes of electroporation-based therapies like E2. It can be further developed to a 3D model to include more aspects of the treatment.

We propose *in vivo* studies that assess time-dependent physiological and molecular events within the treatment field, employing specific dyes, to determine which cell death pathways are triggered after E2 treatment.

Conclusion

Chapter 6

6.1 General conclusions

This research project aimed at better understanding the mechanisms of action of tumor eradication by Electrolytic Electroporation (E2). The goal was to understand the interplay between the two components of the treatment, electrolysis and reversible electroporation, and the process of cell death induced by the treatment.

Electrolysis of organic samples is a process which starts with electrochemical reactions at the electrode surface and continues with ionic movement of the generated species and chemical reactions with other molecules within the tissue. The outcome is a toxic extracellular environment which can induce cell death. While it was clear that electrolysis plays an important role in E2, it was not understood how critical its role is. The results presented in this thesis illustrate that substantial amounts of electrolysis species are produced with the application of only a few E2 pulses, and that these distribute within the treatment field with time. The results also showed, however, that the extracellular concentration of the species, while elevated, cannot induce cell death through extrinsic pathways. This is mainly due to the fact that the exposure time of the cells to these species is very short for the generated concentrations. The *in vitro*, *in vivo* and *in silico* studies presented in this thesis moreover demonstrated that the treatment effect is charge-dependent, in the sense that sufficient concentrations of electrolysis species need to be generated and present in the extracellular space, but that the necessary thresholds are lower than in Electrochemical Treatment.

Electroporation is the second component of E2 and is known to trigger an array of complex molecular processes which result in electropermeabilization of the cell membrane. In E2, reversible electroporation is employed, which means that the induced permeability of the cell membrane is temporary. In the context of an E2 application, electroporation is essential because it enables large bulge concentrations of ions, which are present in the extracellular space after electrolysis, to enter the cell through the induced membrane defects.

It is known that the electroporation efficiency increases with number of pulses, because each pulse further stabilizes the initially created membrane defects. The assessment performed in this study showed that the uptake efficiency during E2 also increases with number of pulses. Similar findings were already presented for other combinational electroporation-based therapies like Electrochemotherapy and Gene Electrotransfer, but not yet for E2.

The key difference between these treatments and E2 is that no additional substance is applied to induce cell death. The question of how exactly the cells die after E2 application was therefore not clear. The results of this thesis imply that the intracellular concentrations achieved after E2 pulse application are potentially high enough to cause intracellular acidosis and alkaliptosis. Both of these effects can trigger regulated cell death via necroptosis and pyroptosis, which is the proposed cell killing mechanism of this work.

Only few pulse applications are required in a typical E2 *in vivo* protocol to achieve cell death even in the middle of very large treatment fields, as long as the total charge applied generates enough electrolytic products and the initial voltage and number of pulses is efficient enough to electroporate all cells within the treatment field. Information on lower limits of all necessary parameters is essential for the development of clinical protocols of any treatment. The work presented here determined the lower threshold of applied charge and electric field strength for successful liver ablations, both of which are below conventional IRE or EChT. Different electrode arrays were employed (two-electrode, four electrode and bipolar electrode applications) to demonstrate where the lower limit lies for each application type. This serves as the basis for the development of effective E2 pulse protocols *in vivo*.

6.2 Future perspectives

Electrolytic Electroporation is a newly proposed combinational treatment, which has opened up a new research area in the field of focal therapy. The work presented in this thesis, together with the studies performed so far which involve E2, represent the foundation for future investigations which can be performed to further understand the mechanism of E2 and implement its use in a clinical setting.

As for the understanding of the mechanistic processes of E2, the thesis provided insight regarding the interplay of the two components and suggested the mechanism of action which induces cell death. Future work could involve the confirmation of the proposed cell death modi by investigating the molecular pathways that are triggered after the treatment.

While the effectiveness of the treatment has been demonstrated well for small and large liver lesions as well as different electrode arrays in pre-clinical studies, the next step is to broaden the application spectrum to other tissue types (e.g. kidney, pancreas, prostate). It can be expected, similar to other electroporation-based therapies, that lower threshold limits and optimum pulse protocols will vary depending on tissue properties.

The majority of pre-clinical data on E2 is based on acute outcomes of the treatment. In order to successfully implement E2 as a minimally-invasive treatment modality for tissue ablation in humans, it is necessary to obtain clinical data with longer follow-up times, investigating treatment safety and efficacy within the scope of a clinical trial.

Finally, the numerical model presented in this thesis was useful in the determination of electrochemical processes of electroporation-based therapies like E2 can be used for continuative studies of other aspects of similar applications. It can be further developed into a 3D model that can predict lesion sizes for different tissue types and applications. The model could be extended to implement other interesting aspects of the treatment, such as tissue inhomogeneity, to make it a useful tool for treatment predictions.

References

1. Weaver, J.C., Chizmadzhev, Y.: Theory of electroporation. A review. Bioelectrochemistry and Bioenergetics (1996). https://doi.org/10.1016/S0302-4598(96)05062-3
2. Neumann, E., Schaefer-Ridder, M., Wang, Y., Hofschneider, P.H.: Gene transfer into mouse lyoma cells by electroporation in high electric fields. The EMBO journal **1**, 841–845 (1982)
3. C. Heller, L., Heller, R.: Electroporation Gene Therapy Preclinical and Clinical Trials for Melanoma. CGT (2010). https://doi.org/10.2174/156652310791823489
4. Neumann, E., Sowers, A.E., Jordan, C.A.: Electroporation and electrofusion in cell biology. Plenum Press, New York (1989)
5. Mir, L.M., Orlowski, S.: The basis of electrochemotherapy. Methods in molecular medicine (2000). https://doi.org/10.1385/1-59259-080-2:99
6. National Institute for Health and Care Excellence (NICE): Electrochemotherapy for primary basal cell carcinoma and primary squamous cell carcinoma. www.nice.org.uk. (2014)
7. National Institute for Health and Care Excellence (NICE): Electrochemotherapy for metastases in the skin from tumours of non-skin origin and melanoma. http://publicationsniceorguk/ (2013)
8. Gehl, J., Sersa, G., Matthiessen, L.W., Muir, T., Soden, D., Occhini, A., Quaglino, P., Curatolo, P., Campana, L.G., Kunte, C., Clover, A.J.P., Bertino, G., Farricha, V., Odili, J., Dahlstrom, K., Benazzo, M., Mir, L.M.: Updated standard operating procedures for electrochemotherapy of cutaneous tumours and skin metastases. Acta oncologica (Stockholm, Sweden) (2018). https://doi.org/10.1080/0284186X.2018.1454602
9. Mir, L.M., Gehl, J., Sersa, G., Collins, C.G., Garbay, J.-R., Billard, V., Geertsen, P.F., Rudolf, Z., O'Sullivan, G.C., Marty, M.: Standard operating procedures of the electrochemotherapy: Instructions for the use of bleomycin or cisplatin administered either systemically or locally and electric pulses delivered by the CliniporatorTM by means of invasive or non-invasive electrodes. European Journal of

Cancer Supplements (2006). https://doi.org/10.1016/j.ejcsup.2006.08.003

10. Matthiessen, L.W., Johannesen, H.H., Hendel, H.W., Moss, T., Kamby, C., Gehl, J.: Electrochemotherapy for large cutaneous recurrence of breast cancer: a phase II clinical trial. Acta oncologica (Stockholm, Sweden) (2012). https://doi.org/10.3109/0284186X.2012.685524
11. Klein, N., Gunther, E., Zapf, S., El-Idrissi, R., Atta, J., Stehling, M.: Prostate cancer infiltrating the bladder sphincter successfully treated with Electrochemotherapy. A case report. Clin Case Rep (2017). https://doi.org/10.1002/ccr3.1270
12. Bianchi, G., Campanacci, L., Ronchetti, M., Donati, D.: Electrochemotherapy in the Treatment of Bone Metastases: A Phase II Trial. World Journal of Surgery (2016). https://doi.org/10.1007/s00268-016-3627-6
13. Edhemovic, I., Gadzijev, E.M., Brecelj, E., Miklavcic, D., Kos, B., Zupanic, A., Mali, B., Jarm, T., Pavliha, D., Marcan, M., Gasljevic, G., Gorjup, V., Music, M., Vavpotic, T.P., Cemazar, M., Snoj, M., Sersa, G.: Electrochemotherapy. A new technological approach in treatment of metastases in the liver. Technology in cancer research & treatment (2011). https://doi.org/10.7785/tcrt.2012.500224
14. Gasljevic, G., Edhemovic, I., Cemazar, M., Brecelj, E., Gadzijev, E.M., Music, M.M., Sersa, G.: Histopathological findings in colorectal liver metastases after electrochemotherapy. PloS one (2017). https://doi.org/10.1371/journal.pone.0180709
15. Miklavčič, D., Sersa, G., Brecelj, E., Gehl, J., Soden, D., Bianchi, G., Ruggieri, P., Rossi, C.R., Campana, L.G., Jarm, T.: Electrochemotherapy. Technological advancements for efficient electroporation-based treatment of internal tumors. Med Biol Eng Comput (2012). https://doi.org/10.1007/s11517-012-0991-8
16. Rubinsky, B., Onik, G., Mikus, P.: Irreversible electroporation. A new ablation modality--clinical implications. Technology in cancer research & treatment (2007). https://doi.org/10.1177/153303460700600106
17. Edd, J.F., Horowitz, L., Davalos, R.V., Mir, L.M., Rubinsky, B.: In vivo results of a new focal tissue ablation technique. Irreversible electroporation. IEEE transactions on bio-medical

engineering (2006). https://doi.org/10.1109/TBME.2006.873745

18. Onik, G., Rubinsky, B.: Irreversible Electroporation: First Patient Experience Focal Therapy of Prostate Cancer. In: Rubinsky, B. (ed.) Irreversible Electroporation. Series in Biomedical Engineering, pp. 235–247. Springer-Verlag Berlin Heidelberg, Berlin, Heidelberg (2010)
19. Davalos, R.V., Mir, L.M., Rubinsky, B.: Tissue Ablation with Irreversible Electroporation. Ann Biomed Eng (2005). https://doi.org/10.1007/s10439-005-8981-8
20. Vogel, J.A., van Veldhuisen, E., Agnass, P., Crezee, J., Dijk, F., Verheij, J., van Gulik, T.M., Meijerink, M.R., Vroomen, L.G., van Lienden, K.P., Besselink, M.G.: Time-Dependent Impact of Irreversible Electroporation on Pancreas, Liver, Blood Vessels and Nerves: A Systematic Review of Experimental Studies. PloS one (2016). https://doi.org/10.1371/journal.pone.0166987
21. Nielsen, K., Scheffer, H.J., van den Tol, M.P., Nilsson, A.: Irreversible Electroporation of Liver Tumors. In: Meijerink, M.R., Scheffer, H.J., Narayanan, G. (eds.) Irreversible Electroporation in Clinical Practice, vol. 4, pp. 139–166. Springer International Publishing, Cham (2018)
22. Holzgang, M., Eigl, B., Erdem, S., Gloor, B., Worni, M.: Irreversible Electroporation in Pancreatic Cancer. In: Rodrigo, L. (ed.) Advances in Pancreatic Cancer. InTech (2018)
23. Stehling, M., Guenther, E., Klein, N.: Irreversible Electroporation in Treatment of Prostate Cancer. Miklavcic D. (eds) Handbook of Electroporation, Springer (2017)
24. Martin, R.C., Schwartz, E., Adams, J., Farah, I., Derhake, B.M.: Intra - operative Anesthesia Management in Patients Undergoing Surgical Irreversible Electroporation of the Pancreas, Liver, Kidney, and Retroperitoneal Tumors. Anesthesiology and pain medicine (2015). https://doi.org/10.5812/aapm.22786
25. Tracy, C.R., Kabbani, W., Cadeddu, J.A.: Irreversible electroporation (IRE): a novel method for renal tissue ablation. BJU international (2011). https://doi.org/10.1111/j.1464-410X.2010.09797.x
26. Sugrue, A., Maor, E., Ivorra, A., Vaidya, V., Witt, C., Kapa, S., Asirvatham, S.: Irreversible electroporation for the treatment of

cardiac arrhythmias. Expert review of cardiovascular therapy (2018). https://doi.org/10.1080/14779072.2018.1459185

27. Klein, N., Zapf, S., Gunther, E., Stehling, M.: Treatment of lymph node metastases from gastric cancer with a combination of Irreversible Electroporation and Electrochemotherapy. A case report. Clin Case Rep (2017). https://doi.org/10.1002/ccr3.1079
28. Horwitz, E.M., Thames, H.D., Kuban, D.A., Levy, L.B., Kupelian, P.A., Martinez, A.A., Michalski, J.M., Pisansky, T.M., Sandler, H.M., Shipley, W.U., Zelefsky, M.J., Hanks, G.E., Zietman, A.L.: Definitions of biochemical failure that best predict clinical failure in patients with prostate cancer treated with external beam radiation alone. A multi-institutional pooled analysis. The Journal of urology (2005). https://doi.org/10.1097/01.ju.0000152556.53602.64
29. Arena, C.B., Sano, M.B., Rossmeisl, J.H., Caldwell, J.L., Garcia, P.A., Rylander, M.N., Davalos, R.V.: High-frequency irreversible electroporation (H-FIRE) for non-thermal ablation without muscle contraction. Biomedical engineering online (2011). https://doi.org/10.1186/1475-925X-10-102
30. Sano, M.B., Fan, R.E., Xing, L.: Asymmetric Waveforms Decrease Lethal Thresholds in High Frequency Irreversible Electroporation Therapies. Scientific reports (2017). https://doi.org/10.1038/srep40747
31. Dong, S., Wang, H., Zhao, Y., Sun, Y., Yao, C.: First Human Trial of High-Frequency Irreversible Electroporation Therapy for Prostate Cancer. Technology in cancer research & treatment (2018). https://doi.org/10.1177/1533033818789692
32. Frandsen, S.K., Gehl, J.: A Review on Differences in Effects on Normal and Malignant Cells and Tissues to Electroporation-Based Therapies: A Focus on Calcium Electroporation. Technology in cancer research & treatment (2018). https://doi.org/10.1177/1533033818788077
33. Calvet, C.Y., Mir, L.M.: The promising alliance of anti-cancer electrochemotherapy with immunotherapy. Cancer metastasis reviews (2016). https://doi.org/10.1007/s10555-016-9615-3
34. Queirolo, P., Marincola, F., Spagnolo, F.: Electrochemotherapy for the management of melanoma skin metastasis: a review of the literature and possible combinations with immunotherapy. Archives of dermatological research (2014). https://doi.org/10.1007/s00403-014-1462-x

35. Alnaggar, M., Lin, M., Mesmar, A., Liang, S., Qaid, A., Xu, K., Chen, J., Niu, L., Yin, Z.: Allogenic Natural Killer Cell Immunotherapy Combined with Irreversible Electroporation for Stage IV Hepatocellular Carcinoma: Survival Outcome. Cellular physiology and biochemistry : international journal of experimental cellular physiology, biochemistry, and pharmacology (2018). https://doi.org/10.1159/000492509
36. Amory, R.: A Treatise on Electrolysis and its applications to Therapeutical and Surgical Treatment in Disease. W. Wood **1886**
37. Nordenström, B.E.: Preliminary trials of electrophoretic ionization in the treatment of malignant tumours. IRCS Medical Science, 537 (1978)
38. Czymek, R., Dinter, D., Löffler, S., Gebhard, M., Laubert, T., Lubienski, A., Bruch, H.-P., Schmidt, A.: Electrochemical treatment. An investigation of dose-response relationships using an isolated liver perfusion model. Saudi journal of gastroenterology : official journal of the Saudi Gastroenterology Association (2011). https://doi.org/10.4103/1319-3767.84491
39. Berendson, J., Simonsson, D.: Electrochemical aspects of treatment of tissue with direct current. The European journal of surgery. Supplement. : = Acta chirurgica. Supplement, 111–115 (1994)
40. Li, K., Xin, Y., Gu, Y., Xu, B., Fan, D., Ni, B.: Effects of direct current on dog liver: possible mechanisms for tumor electrochemical treatment. Bioelectromagnetics **18**, 2–7 (1997)
41. Vijh, A.: Electrochemical treatment (ECT) of cancerous tumours: necrosis involving hydrogen cavitation, chlorine bleaching, pH changes, electroosmosis. International Journal of Hydrogen Energy (2004). https://doi.org/10.1016/S0360-3199(03)00156-3
42. Nilsson, E.: Impact of chlorine and acidification in the electrochemical treatment of tumours. Journal of Applied Electrochemistry (2000). https://doi.org/10.1023/A:1026560806158
43. Turjanski, P., Soba, A., Suarez, C., Colombo, L., González, G., Molina, F., Marshall, G.: Anodic PH Distribution Analysis During Electrochemical Treatment of Tumors: Numerical Simulations. Mecánica Computacional **0**, 3458–3744 (2007)

44. Robertson, G.S., Wemyss-Holden, S.A., Dennison, A.R., Hall, P.M., Baxter, P., Maddern, G.J.: Experimental study of electrolysis-induced hepatic necrosis. The British journal of surgery (1998). https://doi.org/10.1046/j.1365-2168.1998.00806.x
45. J. S. MacLaren: Electrolysis in Prostate Enlargement. Ann. Surg., 347–350 (1989)
46. Gravante, G., Ong, S.L., Metcalfe, M.S., Bhardwaj, N., Maddern, G.J., Lloyd, D.M., Dennison, A.R.: Experimental application of electrolysis in the treatment of liver and pancreatic tumours. Principles, preclinical and clinical observations and future perspectives. Surgical oncology (2011). https://doi.org/10.1016/j.suronc.2009.12.002
47. Lloyd, M., Miller, J., Moretti, K.L., Texler, M., Maddern, G.J.: Electrolysis - a new method of renal ablation? BJU international (2012). https://doi.org/10.1111/j.1464-410X.2012.11478.x
48. Fosh, B.G., Finch, J.G., Lea, M., Black, C., Wong, S., Wemyss-Holden, S., Maddern, G.J.: Use of electrolysis as an adjunct to liver resection. The British journal of surgery (2002). https://doi.org/10.1046/j.1365-2168.2002.02134.x
49. Finch, J.G., Fosh, B., Anthony, A., Slimani, E., Texler, M., Berry, D.P., Dennison, A.R., Maddern, G.J.: Liver electrolysis: pH can reliably monitor the extent of hepatic ablation in pigs. Clinical science (London, England : 1979) **102**, 389–395 (2002)
50. Rubinsky, L., Guenther, E., Mikus, P., Stehling, M., Rubinsky, B.: Electrolytic Effects During Tissue Ablation by Electroporation. Technology in cancer research & treatment (2016). https://doi.org/10.1177/1533034615601549
51. Stehling, M.K., Guenther, E., Mikus, P., Klein, N., Rubinsky, L., Rubinsky, B.: Synergistic Combination of Electrolysis and Electroporation for Tissue Ablation. PloS one (2016). https://doi.org/10.1371/journal.pone.0148317
52. Phillips, M., Krishnan, H., Raju, N., Rubinsky, B.: Tissue Ablation by a Synergistic Combination of Electroporation and Electrolysis Delivered by a Single Pulse. Annals of biomedical engineering (2016). https://doi.org/10.1007/s10439-016-1624-4
53. Phillips, M., Raju, N., Rubinsky, L., Rubinsky, B.: Modulating electrolytic tissue ablation with reversible electroporation

pulses. Technology (2015). https://doi.org/10.1142/S233954781550003X

54. Phillips, M., Rubinsky, L., Meir, A., Raju, N., Rubinsky, B.: Combining Electrolysis and Electroporation for Tissue Ablation. Technology in cancer research & treatment (2015). https://doi.org/10.1177/1533034614560102
55. Rubinsky, B., Gunther, E., Botea, F., Lugnani, F., Herlea, V., Mikus, P., Pautov, M., Klein, N., Pecheanu, C., K. Stehling, M., Tomescu, D., Macchioro6, M., Dima, S., Serban, A., Popescu, I.: Minimally Invasive, Non-Thermal Tissue Ablation with a Single Exponential Decay Electrolytic Electroporation Waveform. JTMR (2016). https://doi.org/10.21614/jtmr-21-4-98
56. Klein, N., Guenther, E., Mikus, P., Stehling, M.K., Rubinsky, B.: Single exponential decay waveform; a synergistic combination of electroporation and electrolysis (E2) for tissue ablation. PeerJ (2017). https://doi.org/10.7717/peerj.3190
57. Galluzzi, L., Vitale, I., Abrams, J.M., Alnemri, E.S., Baehrecke, E.H., Blagosklonny, M.V., Dawson, T.M., Dawson, V.L., El-Deiry, W.S., Fulda, S., Gottlieb, E., Green, D.R., Hengartner, M.O., Kepp, O., Knight, R.A., Kumar, S., Lipton, S.A., Lu, X., Madeo, F., Malorni, W., Mehlen, P., Nuñez, G., Peter, M.E., Piacentini, M., Rubinsztein, D.C., Shi, Y., Simon, H.-U., Vandenabeele, P., White, E., Yuan, J., Zhivotovsky, B., Melino, G., Kroemer, G.: Molecular definitions of cell death subroutines: recommendations of the Nomenclature Committee on Cell Death 2012. Cell death and differentiation (2012). https://doi.org/10.1038/cdd.2011.96
58. Tang, D., Kang, R., Berghe, T.V., Vandenabeele, P., Kroemer, G.: The molecular machinery of regulated cell death. Cell research (2019). https://doi.org/10.1038/s41422-019-0164-5
59. Zhang, Z.-X., Gan, I., Pavlosky, A., Huang, X., Fuhrmann, B., Jevnikar, A.M.: Intracellular pH Regulates TRAIL-Induced Apoptosis and Necroptosis in Endothelial Cells. Journal of immunology research (2017). https://doi.org/10.1155/2017/1503960
60. Park, H.J., Lyons, J.C., Ohtsubo, T., Song, C.W.: Acidic environment causes apoptosis by increasing caspase activity. British journal of cancer (1999). https://doi.org/10.1038/sj.bjc.6690617

61. Matsuyama, S., Reed, J.C.: Mitochondria-dependent apoptosis and cellular pH regulation. Cell death and differentiation (2000). https://doi.org/10.1038/sj.cdd.4400779
62. Roos, A., Boron, W.F.: Intracellular pH. Physiological reviews (1981). https://doi.org/10.1152/physrev.1981.61.2.296
63. Li, J., Cao, F., Yin, H.-L., Huang, Z.-J., Lin, Z.-T., Mao, N., Sun, B., Wang, G.: Ferroptosis: past, present and future. Cell death & disease (2020). https://doi.org/10.1038/s41419-020-2298-2
64. Terman, A., Kurz, T.: Lysosomal iron, iron chelation, and cell death. Antioxidants & redox signaling (2013). https://doi.org/10.1089/ars.2012.4885
65. Chen, M., Cabantchik, Z.I., Chan, S., Chan, G.C., Cheung, Y.: Iron overload and apoptosis of HL-1 cardiomyocytes: effects of calcium channel blockade. PloS one (2014). https://doi.org/10.1371/journal.pone.0112915
66. Yu, Z., Persson, H., Eaton, J.W., Brunk, U.T.: Intralysosomal iron: a major determinant of oxidant-induced cell death. Free Radical Biology and Medicine (2003). https://doi.org/10.1016/S0891-5849(03)00109-6
67. Eid, R., Arab, N.T.T., Greenwood, M.T.: Iron mediated toxicity and programmed cell death: A review and a re-examination of existing paradigms. Biochimica et Biophysica Acta (BBA) - Molecular Cell Research (2017). https://doi.org/10.1016/j.bbamcr.2016.12.002
68. Zhang, Y.-L., Chen, P.-X., Guan, W.-J., Guo, H.-M., Qiu, Z.-E., Xu, J.-W., Luo, Y.-L., Lan, C.-F., Xu, J.-B., Hao, Y., Tan, Y.-X., Ye, K.-N., Lun, Z.-R., Zhao, L., Zhu, Y.-X., Huang, J., Ko, W.-H., Zhong, W.-D., Zhou, W.-L., Zhong, N.-S.: Increased intracellular Cl- concentration promotes ongoing inflammation in airway epithelium. Mucosal immunology (2018). https://doi.org/10.1038/s41385-018-0013-8
69. Miller, L., Leor, J., Rubinsky, B.: Cancer cells ablation with irreversible electroporation. Technology in cancer research & treatment (2005). https://doi.org/10.1177/153303460500400615
70. Rubinsky, J., Onik, G., Mikus, P., Rubinsky, B.: Optimal parameters for the destruction of prostate cancer using irreversible electroporation. The Journal of urology (2008). https://doi.org/10.1016/j.juro.2008.08.003

71. Miklavčič, D. (ed.): Handbook of Electroporation. Springer International Publishing, Cham (2017)
72. Zaman, M.H.: The role of engineering approaches in analysing cancer invasion and metastasis. Nature reviews. Cancer (2013). https://doi.org/10.1038/nrc3564
73. Muratori, C., Pakhomov, A.G., Xiao, S., Pakhomova, O.N.: Electrosensitization assists cell ablation by nanosecond pulsed electric field in 3D cultures. Scientific reports (2016). https://doi.org/10.1038/srep23225
74. Gibot, L., Rols, M.-P.: Progress and prospects. The use of 3D spheroid model as a relevant way to study and optimize DNA electrotransfer. Current gene therapy **13**, 175–181 (2013)
75. Bulysheva, A.A., Burcus, N., Lundberg, C., Edelblute, C.M., Francis, M.P., Heller, R.: Recellularized human dermis for testing gene electrotransfer ex vivo. Biomedical materials (Bristol, England) (2016). https://doi.org/10.1088/1748-6041/11/3/035002
76. Pampaloni, F., Reynaud, E.G., Stelzer, E.H.K.: The third dimension bridges the gap between cell culture and live tissue. Nature reviews. Molecular cell biology (2007). https://doi.org/10.1038/nrm2236
77. Djuzenova, C.S., Zimmermann, U., Frank, H., Sukhorukov, V.L., Richter, E., Fuhr, G.: Effect of medium conductivity and composition on the uptake of propidium iodide into electropermeabilized myeloma cells. Biochimica et Biophysica Acta (BBA) - Biomembranes (1996). https://doi.org/10.1016/S0005-2736(96)00119-8
78. Cromer Berman, S.M., Walczak, P., Bulte, J.W.M.: Tracking stem cells using magnetic nanoparticles. Wiley interdisciplinary reviews. Nanomedicine and nanobiotechnology (2011). https://doi.org/10.1002/wnan.140
79. Kotnik, T., Macek-Lebar, A., Miklavcic, D., Mir, L.M.: Evaluation of cell membrane electropermeabilization by means of a nonpermeant cytotoxic agent. BioTechniques (2000). https://doi.org/10.2144/00285st05
80. Rosazza, C., Haberl Meglic, S., Zumbusch, A., Rols, M.-P., Miklavcic, D.: Gene Electrotransfer: A Mechanistic Perspective. CGT (2016). https://doi.org/10.2174/1566523216666160331130040
81. Golberg, A., Sack, M., Teissie, J., Pataro, G., Pliquett, U., Saulis, G., Stefan, T., Miklavcic, D., Vorobiev, E., Frey, W.:

Energy-efficient biomass processing with pulsed electric fields for bioeconomy and sustainable development. Biotechnology for biofuels (2016). https://doi.org/10.1186/s13068-016-0508-z

82. Kotnik, T., Frey, W., Sack, M., Haberl Meglič, S., Peterka, M., Miklavčič, D.: Electroporation-based applications in biotechnology. Trends in biotechnology (2015). https://doi.org/10.1016/j.tibtech.2015.06.002
83. Castellví, Q., Mercadal, B., Ivorra, A.: Assessment of Electroporation by Electrical Impedance Methods. In: Miklavcic, D. (ed.) Handbook of Electroporation, vol. 67, pp. 1–20. Springer International Publishing, Cham (2016)
84. Batista Napotnik, T., Miklavčič, D.: In vitro electroporation detection methods - An overview. Bioelectrochemistry (Amsterdam, Netherlands) (2018). https://doi.org/10.1016/j.bioelechem.2017.12.005
85. Guenther, E., Klein, N., Mikus, P., Stehling, M.K., Rubinsky, B.: Electrical breakdown in tissue electroporation. Biochemical and biophysical research communications (2015). https://doi.org/10.1016/j.bbrc.2015.10.072
86. Azan, A., Untereiner, V., Descamps, L., Merla, C., Gobinet, C., Breton, M., Piot, O., Mir, L.M.: Comprehensive Characterization of the Interaction between Pulsed Electric Fields and Live Cells by Confocal Raman Microspectroscopy. Analytical chemistry (2017). https://doi.org/10.1021/acs.analchem.7b02079
87. Berridge, M.V., Herst, P.M., Tan, A.S.: Tetrazolium dyes as tools in cell biology. New insights into their cellular reduction. In: El-Gewely, M.R. (ed.) Biotechnology annual review. vol. 11, vol. 11. Biotechnology Annual Review, pp. 127–152. Elsevier, Amsterdam, New York (2005)
88. Li, J., Zhang, D., Ward, K.M., Prendergast, G.C., Ayene, I.S.: Hydroxyethyl disulfide as an efficient metabolic assay for cell viability in vitro. Toxicology in vitro : an international journal published in association with BIBRA (2012). https://doi.org/10.1016/j.tiv.2012.01.007
89. Jakštys, B., Ruzgys, P., Tamošiūnas, M., Šatkauskas, S.: Different Cell Viability Assays Reveal Inconsistent Results After Bleomycin Electrotransfer In Vitro. The Journal of membrane biology (2015). https://doi.org/10.1007/s00232-015-9813-x

90. Gillies, R.J., Didier, N., Denton, M.: Determination of cell number in monolayer cultures. Analytical Biochemistry (1986). https://doi.org/10.1016/0003-2697(86)90314-3
91. Altman, S.A., Randers, L., Rao, G.: Comparison of trypan blue dye exclusion and fluorometric assays for mammalian cell viability determinations. Biotechnology progress (1993). https://doi.org/10.1021/bp00024a017
92. Jones, K.H., Senft, J.A.: An improved method to determine cell viability by simultaneous staining with fluorescein diacetate-propidium iodide. The journal of histochemistry and cytochemistry : official journal of the Histochemistry Society (1985). https://doi.org/10.1177/33.1.2578146
93. Banerjee, A., Majumder, P., Sanyal, S., Singh, J., Jana, K., Das, C., Dasgupta, D.: The DNA intercalators ethidium bromide and propidium iodide also bind to core histones. FEBS open bio (2014). https://doi.org/10.1016/j.fob.2014.02.006
94. Šatkauskas, S., Jakštys, B., Ruzgys, P., Jakutavičiūtė, M.: Different Cell Viability Assays Following Electroporation In Vitro. In: Miklavcic, D. (ed.) Handbook of Electroporation, vol. 9, pp. 1–14. Springer International Publishing, Cham (2016)
95. Pavšelj, N., Miklavčič, D.: Numerical modeling in electroporation-based biomedical applications. Radiology and oncology, 297
96. Soba, A., Suárez, C., González, M.M., Cabrales, L.E.B., Pupo, A.E.B., Reyes, J.B., Martínez Tassé, J.P.: Integrated analysis of the potential, electric field, temperature, pH and tissue damage generated by different electrode arrays in a tumor under electrochemical treatment. Mathematics and Computers in Simulation (2018). https://doi.org/10.1016/j.matcom.2017.11.006
97. Rols, M.P., Teissié, J.: Electropermeabilization of mammalian cells. Quantitative analysis of the phenomenon. Biophysical Journal (1990). https://doi.org/10.1016/S0006-3495(90)82451-6
98. Čorović, S., Mir, L.M., Miklavčič, D.: In vivo muscle electroporation threshold determination: realistic numerical models and in vivo experiments. The Journal of membrane biology (2012). https://doi.org/10.1007/s00232-012-9432-8
99. Miklavčič, D., Šemrov, D., Mekid, H., Mir, L.M.: A validated model of in vivo electric field distribution in tissues for

electrochemotherapy and for DNA electrotransfer for gene therapy. Biochimica et Biophysica Acta (BBA) - General Subjects (2000). https://doi.org/10.1016/S0304-4165(00)00101-X

100. Pavliha, D., Kos, B., Zupanič, A., Marčan, M., Serša, G., Miklavčič, D.: Patient-specific treatment planning of electrochemotherapy: procedure design and possible pitfalls. Bioelectrochemistry (Amsterdam, Netherlands) (2012). https://doi.org/10.1016/j.bioelechem.2012.01.007
101. Poignard C., Silve A., Wegner L.: Different Approaches Used in Modeling of Cell Membrane Electroporation. Handbook of Electroporation, Springer, Cham, 1019–1042. https://doi.org/10.1007/978-3-319-32886-7_3
102. Ivorra, A.: Tissue Electroporation as a Bioelectric Phenomenon: Basic Concepts. In: Rubinsky, B. (ed.) Irreversible Electroporation. Series in Biomedical Engineering, pp. 23–61. Springer-Verlag Berlin Heidelberg, Berlin, Heidelberg (2010)
103. Pintar, M., Langus, J., Edhemović, I., Brecelj, E., Kranjc, M., Sersa, G., Šuštar, T., Rodič, T., Miklavčič, D., Kotnik, T., Kos, B.: Time-Dependent Finite Element Analysis of In Vivo Electrochemotherapy Treatment. Technology in cancer research & treatment (2018). https://doi.org/10.1177/1533033818790510
104. Voyer, D., Silve, A., Mir, L.M., Scorretti, R., Poignard, C.: Dynamical modeling of tissue electroporation. Bioelectrochemistry (Amsterdam, Netherlands) (2018). https://doi.org/10.1016/j.bioelechem.2017.08.007
105. Lackovic, I., Magjarevic, R., Miklavcic, D.: Three-dimensional finite-element analysis of joule heating in electrochemotherapy and in vivo gene electrotransfer. IEEE Trans. Dielect. Electr. Insul. (2009). https://doi.org/10.1109/TDEI.2009.5293947
106. Garcia, P.A., Rossmeisl, J.H., Neal, R.E., Ellis, T.L., Davalos, R.V.: A parametric study delineating irreversible electroporation from thermal damage based on a minimally invasive intracranial procedure. Biomedical engineering online (2011). https://doi.org/10.1186/1475-925X-10-34
107. Sel, D., Lebar, A.M., Miklavcic, D.: Feasibility of employing model-based optimization of pulse amplitude and electrode distance for effective tumor electropermeabilization. IEEE

transactions on bio-medical engineering (2007). https://doi.org/10.1109/TBME.2006.889196

108. Županič, A., Miklavčič, D.: Optimization and Numerical Modeling in Irreversible Electroporation Treatment Planning. In: Rubinsky, B. (ed.) Irreversible Electroporation. Series in Biomedical Engineering, pp. 203–222. Springer-Verlag Berlin Heidelberg, Berlin, Heidelberg (2010)
109. Breton, M., Delemotte, L., Silve, A., Mir, L.M., Tarek, M.: Transport of siRNA through lipid membranes driven by nanosecond electric pulses: an experimental and computational study. Journal of the American Chemical Society (2012). https://doi.org/10.1021/ja3052365
110. Li, J., Tan, W., Yu, M., Lin, H.: The effect of extracellular conductivity on electroporation-mediated molecular delivery. Biochimica et biophysica acta (2013). https://doi.org/10.1016/j.bbamem.2012.08.014
111. Garcia, P.A., Davalos, R.V., Miklavcic, D.: A numerical investigation of the electric and thermal cell kill distributions in electroporation-based therapies in tissue. PloS one (2014). https://doi.org/10.1371/journal.pone.0103083
112. Dermol, J., Miklavčič, D.: Mathematical Models Describing Cell Death Due to Electroporation. In: Miklavčič, D. (ed.) Handbook of Electroporation, vol. 4, pp. 1199–1218. Springer International Publishing, Cham (2017)
113. Euler, H. von, Söderstedt, A., Thörne, A., Olsson, J.M., Yongqing, G.: Cellular toxicity induced by different pH levels on the R3230AC rat mammary tumour cell line. An in vitro model for investigation of the tumour destructive properties of electrochemical treatment of tumours. Bioelectrochemistry (2002). https://doi.org/10.1016/S1567-5394(02)00154-8
114. Nilsson, E., Berendson, J., Fontes, E.: Development of a dosage method for electrochemical treatment of tumours: a simplified mathematical model. Bioelectrochemistry and Bioenergetics (1998). https://doi.org/10.1016/S0302-4598(98)00157-3
115. Nilsson, E., Berendson, J., Fontes, E.: Electrochemical treatment of tumours: a simplified mathematical model. Journal of Electroanalytical Chemistry (1999). https://doi.org/10.1016/S0022-0728(98)00352-0
116. Nilsson, E., Fontes, E.: Mathematical modelling of physicochemical reactions and transport processes occurring

around a platinum cathode during the electrochemical treatment of tumours. Bioelectrochemistry (2001). https://doi.org/10.1016/S0302-4598(01)00097-6

117. Marshall, G., Mocskos, P.: Growth model for ramified electrochemical deposition in the presenceof diffusion, migration, and electroconvection. Phys. Rev. E (1997). https://doi.org/10.1103/PhysRevE.55.549
118. Aguilera, A.R., Cabrales, L.E.B., Ciria, H.M.C., Pérez, Y.S., Oria, E.R., Brooks, S.A., González, T.R.: Distributions of the potential and electric field of an electrode elliptic array used in tumor electrotherapy: Analytical and numerical solutions. Mathematics and Computers in Simulation (2009). https://doi.org/10.1016/j.matcom.2008.11.011
119. Bergues Pupo, A.E., Reyes, J.B., Bergues Cabrales, L.E., Bergues Cabrales, J.M.: Analytical and numerical solutions of the potential and electric field generated by different electrode arrays in a tumor tissue under electrotherapy. Biomedical engineering online (2011). https://doi.org/10.1186/1475-925X-10-85
120. Yacoob, S.M., Hassan, N.S.: FDTD analysis of a noninvasive hyperthermia system for brain tumors. Biomedical engineering online (2012). https://doi.org/10.1186/1475-925X-11-47
121. Li, K., Xin, Y., Gu, Y., Xu, B., Fan, D., Ni, B.: Effects of direct current on dog liver: Possible mechanisms for tumor electrochemical treatment. Bioelectromagnetics (1997). https://doi.org/10.1002/(SICI)1521-186X(1997)18:1<2:AID-BEM2>3.0.CO;2-6
122. Olaiz, N., Suárez, C., Risk, M., Molina, F., Marshall, G.: Tracking protein electrodenaturation fronts in the electrochemical treatment of tumors. Electrochemistry Communications (2010). https://doi.org/10.1016/j.elecom.2009.10.044
123. Turjanski, P., Olaiz, N., Abou-Adal, P., Suárez, C., Risk, M., Marshall, G.: pH front tracking in the electrochemical treatment (EChT) of tumors: Experiments and simulations. Electrochimica Acta (2009). https://doi.org/10.1016/j.electacta.2009.05.062
124. Mokhtare, A., Shiv Krishna Reddy, M., Roodan, V.A., Furlani, E.P., Abbaspourrad, A.: The role of pH fronts, chlorination and physicochemical reactions in tumor necrosis in the electrochemical treatment of tumors: A numerical study.

Electrochimica Acta (2019). https://doi.org/10.1016/j.electacta.2019.03.148

125. Pataro, G., Falcone, M., Donsì, G., Ferrari, G.: Metal release from stainless steel electrodes of a PEF treatment chamber: Effects of electrical parameters and food composition. Innovative Food Science & Emerging Technologies (2014). https://doi.org/10.1016/j.ifset.2013.10.005
126. Pataro G., Donsì G., Ferrari G.: Modeling of Electrochemical Reactions During Pulsed Electric Field Treatment. Handbook of Electroporation, 1–30. https://doi.org/10.1007/978-3-319-26779-1_5-1
127. Mir, L.M.: Nucleic acids electrotransfer-based gene therapy (electrogenetherapy): past, current, and future. Molecular biotechnology (2009). https://doi.org/10.1007/s12033-009-9192-6
128. Silve, A., Mir, L.M.: Cell Electropermeabilization and Cellular Uptake of Small Molecules: The Electrochemotherapy Concept. In: Kee, S.T., Gehl, J., Lee, E.W. (eds.) Clinical aspects of electroporation, pp. 69–82. Springer, New York [u.a.] (2011)
129. André, F.M., Gehl, J., Sersa, G., Préat, V., Hojman, P., Eriksen, J., Golzio, M., Cemazar, M., Pavselj, N., Rols, M.-P., Miklavcic, D., Neumann, E., Teissié, J., Mir, L.M.: Efficiency of High- and Low-Voltage Pulse Combinations for Gene Electrotransfer in Muscle, Liver, Tumor, and Skin. Human Gene Therapy (2008). https://doi.org/10.1089/hum.2008.060
130. Guenther, E., Klein, N., Mikus, P., Botea, F., Pautov, M., Lugnani, F., Macchioro, M., Popescu, I., Stehling, M.K., Rubinsky, B.: Toward a clinical real time tissue ablation technology: combining electroporation and electrolysis (E2). PeerJ (2020). https://doi.org/10.7717/peerj.7985
131. Zhao, L., Rasko, A., Drescher, C., Maleki, S., Cejnar, M., McEwan, A.: Preliminary Validation of Electroporation-Electrolysis (E2) for Cardiac Ablation Using a Parameterisable In-Vivo Model. Conference proceedings : … Annual International Conference of the IEEE Engineering in Medicine and Biology Society. IEEE Engineering in Medicine and Biology Society. Annual Conference (2019). https://doi.org/10.1109/EMBC.2019.8857828
132. Ho, M.P.: Combining Electrolysis and Electroporation for Tissue Ablation. In: Miklavcic, D. (ed.) Handbook of

Electroporation, vol. 71, pp. 1–21. Springer International Publishing, Cham (2016)

133. Coury, L.: Conductance Measurements. Part 1: Theory. Current Separations, 92–96
134. Berjano, E.J., Burdío, F., Navarro, A.C., Burdío, J.M., Güemes, A., Aldana, O., Ros, P., Sousa, R., Lozano, R., Tejero, E., Gregorio, M.A. de: Improved perfusion system for bipolar radiofrequency ablation of liver: preliminary findings from a computer modeling study. Physiological measurement (2006). https://doi.org/10.1088/0967-3334/27/10/N03
135. Arena, C.B., Szot, C.S., Garcia, P.A., Rylander, M.N., Davalos, R.V.: A three-dimensional in vitro tumor platform for modeling therapeutic irreversible electroporation. Biophysical Journal (2012). https://doi.org/10.1016/j.bpj.2012.09.017
136. Zhang, H., Wang, H., Zhu, H., Li, H., Su, T., Li, S., Hu, M., Fan, H.: Hydrothermal synthesis and thermoelectric properties of PbS. Materials Science-Poland (2016). https://doi.org/10.1515/msp-2016-0098
137. Lv, Y., Zhang, Y., Rubinsky, B.: Molecular and histological study on the effects of electrolytic electroporation on the liver. Bioelectrochemistry (Amsterdam, Netherlands) (2019). https://doi.org/10.1016/j.bioelechem.2018.09.007
138. Kranjc, M., Miklavčič, D.: Electric Field Distribution and Electroporation Threshold. In: Miklavčič, D. (ed.) Handbook of Electroporation, vol. 80, pp. 1043–1058. Springer International Publishing, Cham (2017)
139. Subedi, G.P., Johnson, R.W., Moniz, H.A., Moremen, K.W., Barb, A.: High Yield Expression of Recombinant Human Proteins with the Transient Transfection of HEK293 Cells in Suspension. Journal of visualized experiments : JoVE (2015). https://doi.org/10.3791/53568
140. Tang, B., Li, L., Jiang, Z., Luan, Y., Li, D., Zhang, W., Reed, E., Li, Q.Q.: Characterization of the mechanisms of electrochemotherapy in an in vitro model for human cervical cancer. International journal of oncology **26**, 703–711 (2005)
141. Yen, Y., Li, J.-R., Zhou, B.-S., Rojas, F., Yu, J., Chou, C.K.: Electrochemical treatment of human KB cells in vitro. Bioelectromagnetics (1999). https://doi.org/10.1002/(SICI)1521-186X(1999)20:1<34:AID-BEM5>3.0.CO;2-R

142. Perkons, N.R., Stein, E.J., Nwaezeapu, C., Wildenberg, J.C., Saleh, K., Itkin-Ofer, R., Ackerman, D., Soulen, M.C., Hunt, S.J., Nadolski, G.J., Gade, T.P.: Electrolytic ablation enables cancer cell targeting through pH modulation. Communications biology (2018). https://doi.org/10.1038/s42003-018-0047-1
143. Ciria, H.M.C., González, M.M., Zamora, L.O., Cabrales, L.E.B., Sierra González, G.V., Oliveira, L.O. de, Zanella, R., Buzaid, A.C., Parise, O., Brito, L.M., Teixeira, C.A.A., Gomes, M.d.N., Moreno, G., Feo da Veiga, V., Telló, M., Holandino, C.: Antitumor effects of electrochemical treatment. Chinese journal of cancer research = Chung-kuo yen cheng yen chiu (2013). https://doi.org/10.3978/j.issn.1000-9604.2013.03.03
144. van den Bos, W., Scheffer, H.J., Vogel, J.A., Wagstaff, P.G.K., Bruin, D.M. de, Jong, M.C. de, van Gemert, M.J.C., La Rosette, J.J.M.C.H. de, Meijerink, M.R., Klaessens, J.H., Verdaasdonk, R.M.: Thermal Energy during Irreversible Electroporation and the Influence of Different Ablation Parameters. Journal of vascular and interventional radiology : JVIR (2016). https://doi.org/10.1016/j.jvir.2015.10.020
145. Zmuc, J., Gasljevic, G., Sersa, G., Edhemovic, I., Boc, N., Seliskar, A., Plavec, T., Brloznik, M., Milevoj, N., Brecelj, E., Kos, B., Izlakar, J., Jarm, T., Snoj, M., Stukelj, M., Miklavcic, D., Cemazar, M.: Large Liver Blood Vessels and Bile Ducts Are Not Damaged by Electrochemotherapy with Bleomycin in Pigs. Scientific reports (2019). https://doi.org/10.1038/s41598-019-40395-y
146. Diller, K.R.: Modeling of Bioheat Transfer Processes at High and Low Temperatures. In: Bioengineering Heat Transfer, vol. 22. Advances in Heat Transfer, pp. 157–357. Elsevier (1992)
147. Guenther, E., Klein, N., Zapf, S., Weil, S., Schlosser, C., Rubinsky, B., Stehling, M.K.: Prostate cancer treatment with Irreversible Electroporation (IRE): Safety, efficacy and clinical experience in 471 treatments. PloS one (2019). https://doi.org/10.1371/journal.pone.0215093
148. Luján, E., Schinca, H., Olaiz, N., Urquiza, S., Molina, F.V., Turjanski, P., Marshall, G.: Optimal dose-response relationship in electrolytic ablation of tumors with a one-probe-two-electrode device. Electrochimica Acta (2015). https://doi.org/10.1016/j.electacta.2015.10.147
149. Marino, M., Olaiz, N., Signori, E., Maglietti, F., Suárez, C., Michinski, S., Marshall, G.: pH fronts and tissue natural buffer

interaction in gene electrotransfer protocols. Electrochimica Acta (2017). https://doi.org/10.1016/j.electacta.2017.09.021

150. Mercadal, B., Vernier, P.T., Ivorra, A.: Dependence of Electroporation Detection Threshold on Cell Radius: An Explanation to Observations Non Compatible with Schwan's Equation Model. The Journal of membrane biology (2016). https://doi.org/10.1007/s00232-016-9907-0
151. Euler, H. von, Nilsson, E., Olsson, J.M., Lagerstedt, A.-S.: Electrochemical treatment (EChT) effects in rat mammary and liver tissue. In vivo optimizing of a dose-planning model for EChT of tumours. Bioelectrochemistry (2001). https://doi.org/10.1016/S1567-5394(01)00118-9
152. Euler, H. von, Stråhle, K., Thörne, A., Yongqing, G.: Cell proliferation and apoptosis in rat mammary cancer after electrochemical treatment (EChT). Bioelectrochemistry (Amsterdam, Netherlands) (2004). https://doi.org/10.1016/j.bioelechem.2003.10.008
153. Colombo, L., González, G., Marshall, G., Molina, F.V., Soba, A., Suarez, C., Turjanski, P.: Ion transport in tumors under electrochemical treatment: in vivo, in vitro and in silico modeling. Bioelectrochemistry (Amsterdam, Netherlands) (2007). https://doi.org/10.1016/j.bioelechem.2007.07.001
154. Vigue, J.: Asklepios Atlas of Human Anatomy. CBS Publishers & Distributors Pvt. Ltd, New Delhi (2014)
155. Gehl, J., Skovsgaard, T., Mir, L.M.: Vascular reactions to in vivo electroporation: characterization and consequences for drug and gene delivery. Biochimica et Biophysica Acta (BBA) - General Subjects (2002). https://doi.org/10.1016/S0304-4165(01)00233-1
156. Geboers, B., Scheffer, H.J., Graybill, P.M., Ruarus, A.H., Nieuwenhuizen, S., Puijk, R.S., van den Tol, P.M., Davalos, R.V., Rubinsky, B., Gruijl, T.D. de, Miklavčič, D., Meijerink, M.R.: High-Voltage Electrical Pulses in Oncology: Irreversible Electroporation, Electrochemotherapy, Gene Electrotransfer, Electrofusion, and Electroimmunotherapy. Radiology (2020). https://doi.org/10.1148/radiol.2020192190
157. Newman, J., Thomas-Alyea, K.E.: Electrochemical Systems, 3rd edn. Wiley, Somerset (2012)
158. Best, Charles Herbert, Norman B. Taylor: The physiological basis of medical practice. Williams & Wilkins Company (1945)

159. Atkins, P.W., Paula, J. de: Physical chemistry for the life sciences, 2nd edn. Oxford University Press, New York, Madrid (2016)
160. Damjanovic, A., Birss, V.I., Boudreaux, D.S.: Electron Transfer Through Thin Anodic Oxide Films during the Oxygen Evolution Reactions at Pt Electrodes: I . Acid Solutions. J. Electrochem. Soc. (1991). https://doi.org/10.1149/1.2086015
161. Bard, A.J., Ketelaar, J.A.A.: Encyclopedia of Electrochemistry of the Elements. J. Electrochem. Soc. (1974). https://doi.org/10.1149/1.2402383
162. Ashour, S.S., Rinker, E.B., Sandall, O.C.: Absorption of chlorine into aqueous bicarbonate solutions and aqueous hydroxide solutions. AIChE J. (1996). https://doi.org/10.1002/aic.690420308
163. Ashour, S.S., Rinker, E.B., Sandall, O.C.: Absorption of chlorine into aqueous bicarbonate solutions and aqueous hydroxide solutions. AIChE J. (1996). https://doi.org/10.1002/aic.690420308
164. Ivorra, A., Villemejane, J., Mir, L.M.: Electrical modeling of the influence of medium conductivity on electroporation. Physical chemistry chemical physics : PCCP (2010). https://doi.org/10.1039/C004419A
165. Li, J., Lin, H.: The current-voltage relation for electropores with conductivity gradients. Biomicrofluidics (2010). https://doi.org/10.1063/1.3324847
166. Weaver, J.C., Vernier, P.T.: Pore lifetimes in cell electroporation: Complex dark pores? https://arxiv.org/pdf/1708.07478 (2017)
167. Pavlin, M., Miklavcic, D.: Theoretical and experimental analysis of conductivity, ion diffusion and molecular transport during cell electroporation--relation between short-lived and long-lived pores. Bioelectrochemistry (Amsterdam, Netherlands) (2008). https://doi.org/10.1016/j.bioelechem.2008.04.016
168. Kotnik, T., Rems, L., Tarek, M., Miklavčič, D.: Membrane Electroporation and Electropermeabilization: Mechanisms and Models. Annual review of biophysics (2019). https://doi.org/10.1146/annurev-biophys-052118-115451
169. Saulis, G., Saulė, R.: Size of the pores created by an electric pulse: microsecond vs millisecond pulses. Biochimica et

biophysica acta (2012). https://doi.org/10.1016/j.bbamem.2012.06.018

170. Teissie, J., Golzio, M., Rols, M.P.: Mechanisms of cell membrane electropermeabilization: a minireview of our present (lack of ?) knowledge. Biochimica et biophysica acta (2005). https://doi.org/10.1016/j.bbagen.2005.05.006
171. Teissie, J.: Membrane Permeabilization Lifetime in Experiments. In: Miklavcic, D. (ed.) Handbook of Electroporation, pp. 1–15. Springer International Publishing, Cham (2016)
172. Zaharoff, D.A., Henshaw, J.W., Mossop, B., Yuan, F.: Mechanistic analysis of electroporation-induced cellular uptake of macromolecules. Experimental biology and medicine (Maywood, N.J.) (2008). https://doi.org/10.3181/0704-RM-113
173. Foster, L.S., Gruntfest, I.J.: Demonstration experiments using universal indicators. J. Chem. Educ. (1937). https://doi.org/10.1021/ed014p274
174. Palin, A.T.: The Determination of Free and Combined Chlorine in Water by the Use of Diethyl- p -phenylene Diamine. Journal - American Water Works Association (1957). https://doi.org/10.1002/j.1551-8833.1957.tb16870.x
175. Song, X., Zhu, S., Xie, Y., Liu, J., Sun, L., Zeng, D., Wang, P., Ma, X., Kroemer, G., Bartlett, D.L., Billiar, T.R., Lotze, M.T., Zeh, H.J., Kang, R., Tang, D.: JTC801 Induces pH-dependent Death Specifically in Cancer Cells and Slows Growth of Tumors in Mice. Gastroenterology (2018). https://doi.org/10.1053/j.gastro.2017.12.004
176. Li, S.-W., Liu, C.-M., Guo, J., Marcondes, A.M., Deeg, J., Li, X., Guan, F.: Iron overload induced by ferric ammonium citrate triggers reactive oxygen species-mediated apoptosis via both extrinsic and intrinsic pathways in human hepatic cells. Human & experimental toxicology (2016). https://doi.org/10.1177/0960327115597312
177. Goldberg, E., Suárez, C., Alfonso, M., Marchese, J., Soba, A., Marshall, G.: Cell membrane electroporation modeling: A multiphysics approach. Bioelectrochemistry (Amsterdam, Netherlands) (2018). https://doi.org/10.1016/j.bioelechem.2018.06.010
178. Klein, N., Guenther, E., Botea, F., Pautov, M., Dima, S., Tomescu, D., Popescu, M., Ivorra, A., Stehling, M., Popescu, I.: The combination of electroporation and electrolysis (E2)

employing different electrode arrays for ablation of large tissue volumes. PloS one (2019). https://doi.org/10.1371/journal.pone.0221393

179. Rodaite-Riseviciene, R., Saule, R., Snitka, V., Saulis, G.: Release of Iron Ions From the Stainless Steel Anode Occurring During High-Voltage Pulses and Its Consequences for Cell Electroporation Technology. IEEE Trans. Plasma Sci. (2014). https://doi.org/10.1109/TPS.2013.2287499
180. Roodenburg, B., Morren, J., Berg, H.E., Haan, S.W. de: Metal release in a stainless steel Pulsed Electric Field (PEF) system. Innovative Food Science & Emerging Technologies (2005). https://doi.org/10.1016/j.ifset.2005.04.006
181. Bandura, A.V., Lvov, S.N.: The Ionization Constant of Water over Wide Ranges of Temperature and Density. Journal of Physical and Chemical Reference Data (2006). https://doi.org/10.1063/1.1928231

List of publications

Peer-reviewed journal articles

1. **Klein, N.**, Mercadal, B., Stehling, M., & Ivorra, A. (2020). In vitro study on the mechanisms of action of electrolytic electroporation (E2). Bioelectrochemistry, 133, 107482.
2. Guenther E, **Klein N.**, Mikus P, Botea F, Pautov M, Lugnani F, Macchioro M, Popescu I, Stehling MK, Rubinsky B. (2020). Toward a clinical real time tissue ablation technology: combining electroporation and electrolysis (E2) *PeerJ 8:e7985 https://doi.org/10.7717/peerj.7985*
3. **Klein, N.**, Guenther, E., Botea, F., Pautov, M., Dima, S., Tomescu, D., ... & Popescu, I. (2019). The combination of electroporation and electrolysis (E2) employing different electrode arrays for ablation of large tissue volumes. PloS one, 14(8).
4. Guenther, E., **Klein, N.**, Zapf, S., Weil, S., Schlosser, C., Rubinsky, B., & Stehling, M. K. (2019). Prostate cancer treatment with Irreversible Electroporation (IRE): Safety, efficacy and clinical experience in 471 treatments. *PloS one*, 14(4), e0215093.
5. **Klein, N.**, Weil, S., Guenther, E., Stehling, M. Safety and toxicity profile of irreversible electroporation in combination with bleomycin for the treatment of high-risk prostate cancer *(under preparation)*
6. **Klein, N.**, Stehling, M., & Ivorra, A. Electrochemical effects in electrolytic electroporation (E2) *(under preparation)*

Abstracts in conference proceedings

1. **Klein, N.,** Stehling, M., Ivorra, A. (2020). Towards a finite element simulation of minimally-invasive tissue ablation employing electrolytic electroporation (E2). *8th European Medical and Biological Engineering Conference (EMBEC 2020),* Portorož, Slovenia, 29 November − 3 December 2020
2. **Klein, N.,** Weil, Stephanie, Stehling, M. (2020). Electrochemotherapy for high-grade prostate cancer. *8th European Medical and Biological Engineering Conference*

(EMBEC 2020), Portorož, Slovenia, 29 November − 3 December 2020

3. **Klein, N.**, Stehling, M., Ivorra, A. (2019). pH Distribution during Electrolytical Electroporation (E2). *Third World Congress on Electroporation and Pulsed Electric Fields in Biology, Medicine and Food & Environmental Technologies*, Toulouse, France, 3-6th of September 2019
4. Stehling, M., **Klein, N.**, Guenther, E., Czeloth, K. (2019). 6-year Outcomes Following Treatment with Irreversible Electroporation of High-Grade Prostate Cancer. *Third World Congress on Electroporation and Pulsed Electric Fields in Biology, Medicine and Food & Environmental Technologies,* Toulouse, France, 3-6th of September 2019
5. **Klein, N.**, Stehling, M.K. & Ivorra, A. (2018) Preliminary results on the *in vitro* comparison between Irreversible Electroporation and the combination of Electroporation and Electrolysis (E2), *Electroporation-Based Technologies and Treatments, International scientific workshop and postgraduate course*, November 11-17 2018, Ljubljana, Slovenia

Patents

1. Guenther, E., Rubinsky, B., **Klein, N.**, Mikus, P., Stehling, M. Methods, Systems, and apparatuses for tissue ablation using a modulated exponential decay pulse. WO2020051241A1, Priority date 2018-09-04